multi-Risk sciEnce for resilienT commUnities undeR a changiNg climate

Codice progetto MUR: **PE00000005**

Deliverable title: **Advanced physics-and-data driven modelling approaches**

Deliverable ID: **DV 4.4.a**

Due date: **30/11/2024**

AUTHORS

Cristiana Bragalli (UNIBO); Walter Lacarbonara (UNIROMA1); Raffaele Landolfo (UNINA); Aldo Milone (UNINA); Giuseppe Quaranta (UNIROMA1); Elena Toth (UNIBO); Lorenzo Carmelo Zingali (UNIBO)

Approved by: **Prof. Marco Savoia (WP Leader)**

1. Technical references

Project Acronym	RETURN
Project Title	multi-Risk sciEnce for resilienT commUnities undeR a changiNg climate
Project Coordinator	Domenico Calcaterra UNIVERSITÀ DEGLI STUDI DI NAPOLI FEDERICO II domcalca@unina.it
Project Duration	December 2022 – November 2025 (36 months)

Deliverable No.	DV 4.4.a
Dissemination level*	PP
Work Package	WP4 – Modelling and experimental technologies (including AI) for vulnerability assessment
Task	T4.4 – Advanced strategies for infrastructure modelling and vulnerability assessment
Lead beneficiary	UNIROMA1
Contributing beneficiaries	UNIBO, UNINA, UNIROMA1

* PU = Public

PP = Restricted to other programme participants (including the Commission Services)

RE = Restricted to a group specified by the consortium (including the Commission Services)

CO = Confidential, only for members of the consortium (including the Commission Services)

1.1 Document history

Version	Date	Lead contributor(s)	Description
0.1	01.10.2024	Raffaele Landolfo (UNINA), Aldo Milone (UNINA)	Layout of the contribution
0.2	07.10.2024	Walter Lacarbonara (UNIROMA1) Giuseppe Quaranta (UNIROMA1)	Layout of the contribution
0.3	10.10.2024	Cristiana Bragalli (UNIBO) Elena Toth (UNIBO)	Layout of the contribution
1.1	03.12.2024	Walter Lacarbonara (UNIROMA1) Giuseppe Quaranta (UNIROMA1)	Template and instructions
2.1	06.12.2024	Aldo Milone (UNINA)	First draft of the contribution
2.2	09.12.2024	Raffaele Landolfo (UNINA)	Edits for approval of the contribution
2.3	10.12.2024	Raffaele Landolfo (UNINA) Aldo Milone (UNINA)	Final version of the contribution
3.1	13.12.2024	Giuseppe Quaranta (UNIROMA1)	First draft of the contribution
3.2	16.12.2024	Walter Lacarbonara (UNIROMA1) Giuseppe Quaranta (UNIROMA1)	Edits for approval of the contribution
3.3	17.12.2024	Walter Lacarbonara (UNIROMA1) Giuseppe Quaranta (UNIROMA1)	Final version of the contribution
4.1	06.12.2024	Cristiana Bragalli (UNIBO) Elena Toth (UNIBO) Lorenzo C. Zingali (UNIBO)	First draft of the contribution
4.2	15.12.2024	Cristiana Bragalli (UNIBO) Elena Toth (UNIBO) Lorenzo C. Zingali (UNIBO)	Edits for approval of the contribution
4.3	17.12.2024	Cristiana Bragalli (UNIBO) Elena Toth (UNIBO) Lorenzo C. Zingali (UNIBO)	Final version of the contribution
5.1	20.12.2024	Walter Lacarbonara (UNIROMA1)	Edits for approval of the deliverable
5.2	21.12.2024	Walter Lacarbonara (UNIROMA1) Giuseppe Quaranta (UNIROMA1)	Submission of the deliverable
5.3	26.02.2026	Walter Lacarbonara (UNIROMA1) Giuseppe Quaranta (UNIROMA1)	Submission of the updated deliverable

2. Abstract

Working Package 4 focuses on advanced technologies to assess the vulnerability of existing infrastructures at the component level. Key sectors under consideration include transportation, hydraulic, energy, and telecommunication infrastructures. The approach integrates in-situ diagnostics, unmanned surveys equipped with AI recognition systems and machine learning algorithms, as well as remote sensing techniques to monitor degradation phenomena. Advanced infrastructure modelling, incorporating dynamic identification and model updating, supports vulnerability assessment and the establishment of alarm thresholds for early warning systems.

Within the framework of Work Package 4, Task 4 is dedicated to developing strategies to model infrastructure components, assessing their vulnerability and robustness under current and future conditions. The methodology incorporates degradation processes and the impacts of both natural and human-induced actions, employing dynamic system identification, Bayesian model updating, and scenario analysis.

This report titled “Advanced physics-and-data driven modelling approaches” (DV 4.4.a) is the first out of three deliverables expected for this Task. It aims to gather outputs from the participating Research Units on the numerical modeling of infrastructure components, utilizing physics-based approaches, data-driven techniques, or a combination of both.

In particular, the research unit UNINA (contributors: Raffaele Landolfo and Aldo Milone) developed a finite element model for multi-scale analysis of steel bridges subjected to combined fatigue and man-induced and/or environmental degradation. The research unit UNIROMA1 (contributors: Walter Lacarbonara and Giuseppe Quaranta) developed both semi-analytical physics-based models and machine learning models to study dynamic vehicle-bridge interaction in braking scenarios. The work also includes scenarios analysis, uncertainty quantification and experimental validations. The research unit UNIBO (contributors: Cristiana Bragalli, Elena Toth and Lorenzo Carmelo Zingali) developed a multiple dimensions data-driven numerical modeling approach applied to the water distribution system of Parma managed by IREN SpA. An advanced hydraulic (physically-based) model of this real-world water distribution system has been implemented in WNTR Python package able to perform multiple analysis.

3. Table of contents

1. Technical references 2
   1.1 Document history 3
2. Abstract 4
3. Table of contents 5
   3.1 List of Tables 7
   3.2 List of Figures 7
4. Multiscale modelling of steel bridges subjected to fatigue, man-induced and environmental degradation 9
   4.1 Generality 9
   4.2 State-of-the-art on multiscale modelling of CIs 9
   4.3 Main features of the proposed methodology 11
   4.4 Principles of the Strain Energy Density method 12
   4.5 Multi-scale modelling of steel bridges for SED applications 14
      4.5.1 Insights about global modelling and global-local interaction 14
      4.5.2 Insights about local modelling and SED-based fatigue assessment 14
   4.6 SED-based assessment of the influence of man-induced and environmental degradation 16
   4.7 Applicative example 17
      4.7.1 Generality and geometrical features of the case study 17
      4.7.2 MS-FEM of the case study 19
      4.7.3 SED-based assessment in pristine conditions 20
      4.7.4 Effect of structural degradation 22
   4.8 Derivation of structural fragility using multi-scale modelling 24
      4.8.1 Frequentist approach for fragility derivation 25
      4.8.2 Distribution based approach for fragility derivation 26
   4.9 Applicative example: POC2 Cadore Bridge 28
      4.9.1 Generalities 28
      4.9.2 Constructional details 29
      4.9.3 Geometric reconstruction of POC2 Cadore bridge 30
      4.9.4 Global FE modelling of POC2 Cadore bridge 30
      4.9.5 Considerations about spatial development of corrosion in Cadore bridge 32
      4.9.6 Local FE modelling of POC2 Cadore bridge 32
      4.9.7 Fragility estimation of Cadore bridge 34
   4.10 Conclusions 35
   4.11 References 36
5. Physics-based models, surrogate models and experimental assessment of the vehicle-bridge interaction in braking conditions 37

5.1 Introduction 37
5.2 Numerical modeling 38
5.2.1 Dynamic analysis of the vehicle-bridge interaction in braking conditions 38
5.2.2 Physics-based vehicle-bridge dynamic modelling 40
5.2.3 Machine-learning-aided surrogate vehicle-bridge dynamic modelling 42
5.3 Numerical and experimental applications 43
5.3.1 Monte Carlo simulations 44
5.3.2 Experimental validation 45
5.4 References 46
6. Data-driven numerical modeling of water infrastructure 48
6.1 Introduction 48
6.2 Main features of the proposed methodology 48
6.2.1 Topological dimension in numerical modeling 49
6.2.2 Numerical modeling for Primary network analysis 50
6.2.3 Structural dimension in numerical modeling 51
6.2.4 Hydraulic dimension in numerical modeling 51
6.3 Case study: Parma water distribution systems 53
6.3.1 Topological dimension: Primary Network analysis of Parma WDS 53
6.3.2 Hydraulic dimension: WNTR analysis with the numerical model of Parma WDS 54
6.3.3 Structural dimension in numerical model of Parma WDS 55
6.4 Vulnerability assessment scenarios 57
6.4.1 Vulnerability assessment on the current scenario 57
6.4.2 Vulnerability assessment on the future scenario 58
6.5 References 59

3.1 List of Tables

Table 4.7-1 – SED-based fatigue assessment of the case study: total fatigue damage and residual service life for each considered clamping loss scenario. 23
Table 5.2-1 – Physics-based models of the vehicle-bridge interaction in braking conditions. 39
Table 5.3-1 – Statistics of the IF estimates (CoV: coefficient of variation). 45
Table 6.3-1 – Water distribution network of Parma: distribution of breaks as a function of the pipe material. 57
Table 6.3-2 – Water distribution network of Parma: distribution of breaks as a function of the diameter. 57

3.2 List of Figures

Figure 4.2-1 – MS-FEM of Runyang Suspension Bridge for dynamic identification purposes (Adapted from *Wang et al., 2013*). 10
Figure 4.2-2 – MS-FEM of Stonecutters Bridge (Adapted from *Zhu et al., 2014*). 11
Figure 4.3-1 – Proposed methodology for fatigue assessment of steel bridges via MS-FEM. 11
Figure 4.4-1 – *a*) Control volumes for typical notched components and mechanical significance of ASED parameter and *b*) application of SED method to steel and aluminum fillet welded joints (Adapted from *Berto & Lazzarin, 2014*). 13
Figure 4.5-1 – MS-FEM of steel bridges for SED applications: Global modelling. 14
Figure 4.5-2 – MS-FEM of steel bridges for SED applications: Local modelling. 15
Figure 4.6-1 – Modelling of typical degradation phenomena in steel bridges: *a*) clamping loss, *b*) metallic corrosion. 17
Figure 4.7-1 – Main features of the selected case study: *a*) geometrical features retrieved in the original design report, *b*) front view with the critical double covered joint being highlighted. .. 18
Figure 4.7-2 – Main features of most critical structural detail: longitudinal girder-to-girder DCJ. 19
Figure 4.7-3 – MS-FEM of the selected case study. 19
Figure 4.7-4 – SED-based fatigue assessment of the critical detail: *a-b*) derivation of the master fatigue curve from data reported in *Razavi et al., 2017*, *c*) definition of Ω_{SED} for the DCJ..... 20
Figure 4.7-5 – SED-based fatigue assessment of the critical detail: *a*) moving load analysis, *b*) estimation of ASED ranges, *c*) residual service life estimation through the PM rule..... 22
Figure 4.7-6 – Clamping loss scenarios considered for the case study. 23
Figure 4.7-7 – Effect of clamping loss for the selected case study: *a*) alterations in load transfer mechanism and *b*) progressive reduction of residual service life. 24
Figure 4.8-1 –Examples of normalized parametric trends for degradation evolution. 25
Figure 4.8-2– Damage matrix **[D]** in case of corrosion-depending degradation. 25
Figure 4.8-3 – Example of application of the proposed frequentist approach. 26
Figure 4.8-4 – Example of application of the proposed distribution-based approach. 27
Figure 4.9-1 – Geolocalization and lateral view of the Cadore Bridge in Perarolo di Cadore (BL). 28
Figure 4.9-2 – Structural details of Cadore bridge: a) base hinge, b) central span OSD. 29
Figure 4.9-3: a) Structural lateral view of the Cadore bridge with different cross-section configurations being highlighted in blue (girder) and cyan (piers), b) Example of cross-section reconstruction for Girder segment A-A'. 30
Figure 4.9-4: Global FE modelling of the Cadore bridge: 31
Figure 4.9-5: NTC2018-compliant stress oscillograms for deck section F-F'. 32
Figure 4.9-6: Assumed spatial development of corrosion for Cadore Bridge (Section F-F'). 32
Figure 4.9-7: Local FE modelling of Cadore bridge for SED calculations. 33
Figure 4.9-8: Results of local FE analyses: distribution of maximum principal stresses and strain energy density for a) pristine detail (η = 0%), b) worn detail (η = 10%). 34
Figure 4.9-9: Fragility assessment of Cadore Bridge: a) relevant parameters for the frequentist and distribution-based approach and b) resulting fragility curves. 35

Figure 5.2-1 – Synoptic scheme that resumes the assumptions underlying the estimation of the IF according to the considered physics-based models. 40
Figure 5.2-2 – Single degrees-of-freedom vehicle model moving on a pinned-pinned beam-type bridge model. 41
Figure 5.2-3 – Two degrees-of-freedom vehicle model moving on a pinned-pinned beam-type bridge model. 41
Figure 5.2-4 – Genetic-algorithm-based optimization of the artificial neural network architecture. 43
Figure 5.3-1 – Some views of the bridge under investigation from the road level (a) and from beneath the deck (b), where it is also possible to note the equipment that was installed to measure the deflection under the applied dynamic load. 44
Figure 5.3-2 – Variation of IF as a function of the vehicle velocity: confidence bounds estimated using the physics-based model, nominal values carried out through surrogate modelling, and experimental data. 46
Figure 6.2-1 – Map of interdependencies between water infrastructure and the environmental, social and economic context (Ofwat, 2015). 49
Figure 6.2-2 – Framework components and tools used (Aljadhai et al., 2018). 49
Figure 6.2-3 – Prediction models for failure probability of water pipes (Taiwo et al., 2023). 51
Figure 6.2-4 – Descriptive statistics of the influencing factors (Taiwo et al., 2023); (b) pipe break dataset aggregated based on nearest distance of break point to the pipe (Fun et al., 2022). 52
Figure 6.2-5 – Well system modeling scheme. 53
Figure 6.3-1 – Primary Network by the algorithm proposed in Zingali et al. (2024): Steiner Tree Network. 54
Figure 6.3-2 – WNTR PDA results: flow rate entering the system is represented in black; the system demand (user consumption and leakage) in blue, obtained subtracting water transfers to other systems; finally, leakage flow rate in red. 54
Figure 6.3-3 – WNTR PDA results: maps of maximum, average and minimum pressures and relative percentage distribution at the nodes of the Parma water distribution system model, respectively in (a), (b) and (c). 56
Figure 6.3-4 – (a) grouping of pipelines that did not suffer any breaks in the period 2022-2023 (black line), that suffered breaks in 2022 (orange line), in 2023 (green line) or that suffered breaks in both years (blue line); (b) interventions on water network in 2023 based on the type: breaks on water pipelines (red dots) and breaks on user connections (green dots). 56
Figure 6.4-1 – WNTR PDA results: representative trend of the production from the well group, which is no longer available in this scenario. 58
Figure 6.4-2 – WNTR PDA results vulnerability assessment on the current scenario concerns the unavailability of an important groups of wells: maps of average pressures and relative percentage distribution at the nodes of the Parma water distribution system model. 58
Figure 6.4-3 – WNTR PDA model: drawdown of the dynamic groundwater level as shown in the curve, consistently with the well system modelling scheme shown in Figure 6.2-5. 59
Figure 6.4-4 – WNTR PDA results: maps of average pressures and relative percentage distribution at the nodes of the Parma water distribution system model considers a future generalized lowering of the groundwater table equal to 5 m, in order to assess whether the current pumping facilities are capable of compensating for this drawdown. 59

4. Multiscale modelling of steel bridges subjected to fatigue, man-induced and environmental degradation

4.1 Generality

Steel and steel-concrete composite bridges represent a significant aliquot of the infrastructural stock in Italy. As reported by major Italian highway network managements, almost 10% of highway bridges in the country features a steel or composite deck. Most of such manufacts are employed as highway overpasses with an average span of ≈ 30 – 40 m, simply-supported schemes and are characterized by a very significant average daily traffic (ADT). Remarkably, a large part of these structures already endured a non-negligible service life (about 40 years).

In the same fashion, over 4000 Italian railway bridges in service are made of steel. To this end, the most common structural solution is represented by 3D truss schemes featuring coupled (e.g., usually battened) members. Most of these bridges experienced a very long service life up to present time (more than 100 years in about 30% of the cases) and are characterized by obsolete details such as hot-driven riveted (HDR) connection, which were the most common structural detail implemented in steel bridges erected in the XIXth century and the first half of the XXth century.

In light of the above, it is quite clear how fatigue phenomena can represent a critical issue for steel and composite bridges, i.e., also in light of their typically limited redundancy deriving from adopted schemes. This criticality is further worsened by structural aging in the form of either man-induced and/or environmental degradation. As for the former case, it is worth mentioning how – in case of bridges featuring bolted connections – clamping loss due to traffic-induced loosening can significantly reduce fatigue life of details. With respect to environmental effects, the clearest hazard for steel infrastructures is represented by metallic corrosion, which can result in strong stress amplifications.

Within this framework, this contribution presents a technique for multi-scale finite element modelling (MS-FEM) of critical steel bridge infrastructures based on the Strain Energy Density (SED) method, i.e., in order to assess the influence of degradation on the fatigue performance of critical details.

This Section is hence mainly divided in six parts. In subSection 4.2, a brief state-of-the-art review on established multi-scale modelling techniques for steel bridges is first presented. Subsequently, the main features of the proposed, SED-based, methodology are introduced (§4.3). A wider focus on basic principles of the SED method is hence given in subSection 4.4. subSection 4.5 presents some more details on how to link different scale models with peculiar reference to steel bridges. Finally, the influence of man-induced and environmental degradation is theoretically (§4.6) and practically (§4.7) addressed.

4.2 State-of-the-art on multiscale modelling of CIs

MS-FEM of Critical Infrastructures (CIs) is based on a combination of global structural analysis with detailed local damage assessment, i.e., with the aim to enable a comprehensive performance evaluation.

This approach can either involve different element types and scales within a single FEM, i.e., as e.g. shown by *Mashayekhi & Santini-Bell, 2020*, *Li et al., 2007*, or be based on structural sub-assembly (*Milone et al., 2024*, *Tartaglia et al., 2022*).

Recently, various techniques have been developed for a concurrent multi-objective optimization to update multi-scale models, improving accuracy in both global and local response predictions (see e.g. *Wang et al., 2013*). These models, when properly developed and calibrated, can effectively represent complex parts of CIs such as bridge welded, bolted or riveted connections, while maintaining computational efficiency.

Moreover, on principle, MS-FEM can be combined with structural health monitoring (SHM), i.e., in order to validate and/or update models to provide accurate assessments of bridge performance and safety.

In order to give context for the methodology proposed in subSection 4.3, in the following few notable contributions devoted to MS-FEM of CIs are mentioned. *Wang et al., 2013* developed a multi-scale model of Runyang Suspension Bridge in Jiangsu, China (see Figure 4.2-1) for dynamic identification purposes. The Authors indeed employed 1D frame and cable elements to model the entire bridge, while a limited portion of the orthotropic deck was accurately reproduced through 2D shell elements. Computational effort and analyses accuracy were balanced with an optimization procedure aiming at properly capturing *i*) bridge modal shapes and frequencies, *ii*) midspan deflections and *iii*) local stress values on the refined portion.

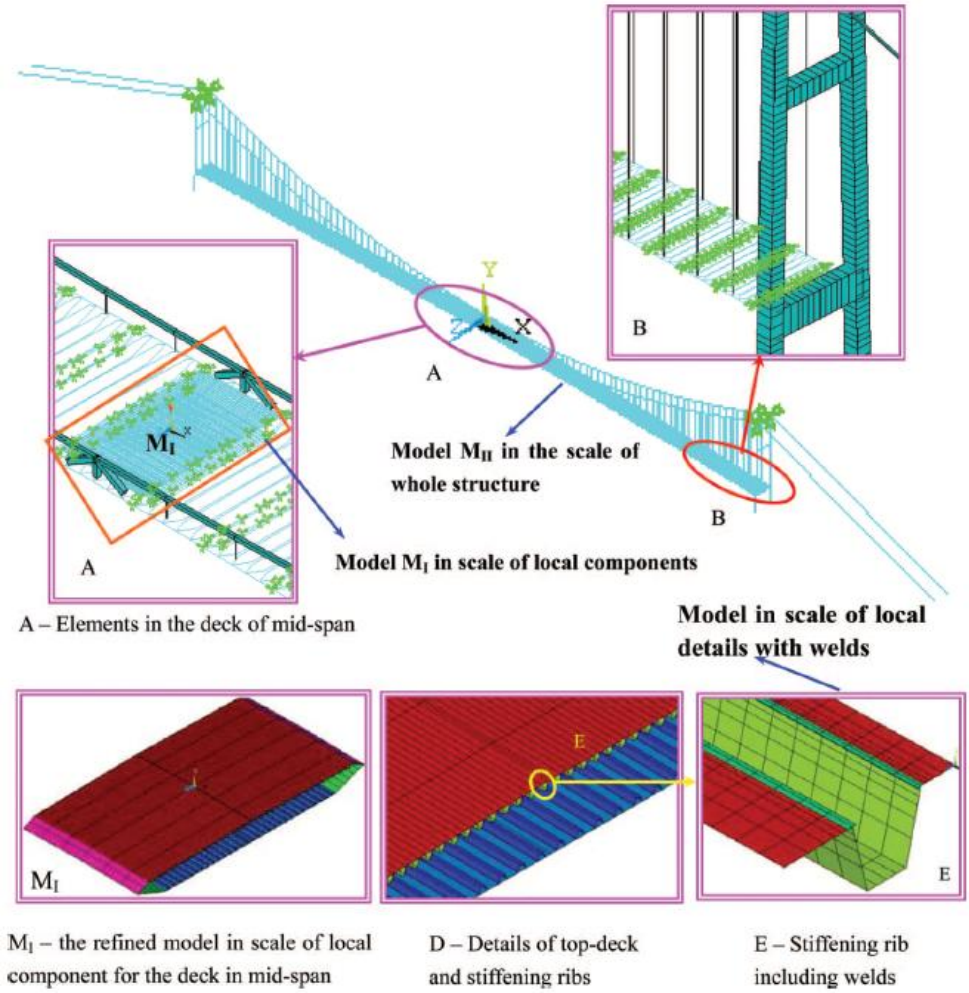

Figure 4.2-1 – MS-FEM of Runyang Suspension Bridge for dynamic identification purposes (Adapted from *Wang et al., 2013*).

Zhu et al., 2014 addressed MS-FEM of Stonecutters Bridge in Hong Kong, China (see Figure 4.2-2) aiming at integrating results from on-site SHM and outcomes from numerical analyses. In the same fashion of the previous work, 1D frame and cable elements were used to model strands and parts of the deck, while 3D brick elements were used to model piers, shafts and specific parts of the collaborating concrete slab. The Authors

showed how proper MS-FEM of this long-span bridge could *i*) support the interpretation of SHM results and *ii*) allow accurate damage analysis of bridge details.

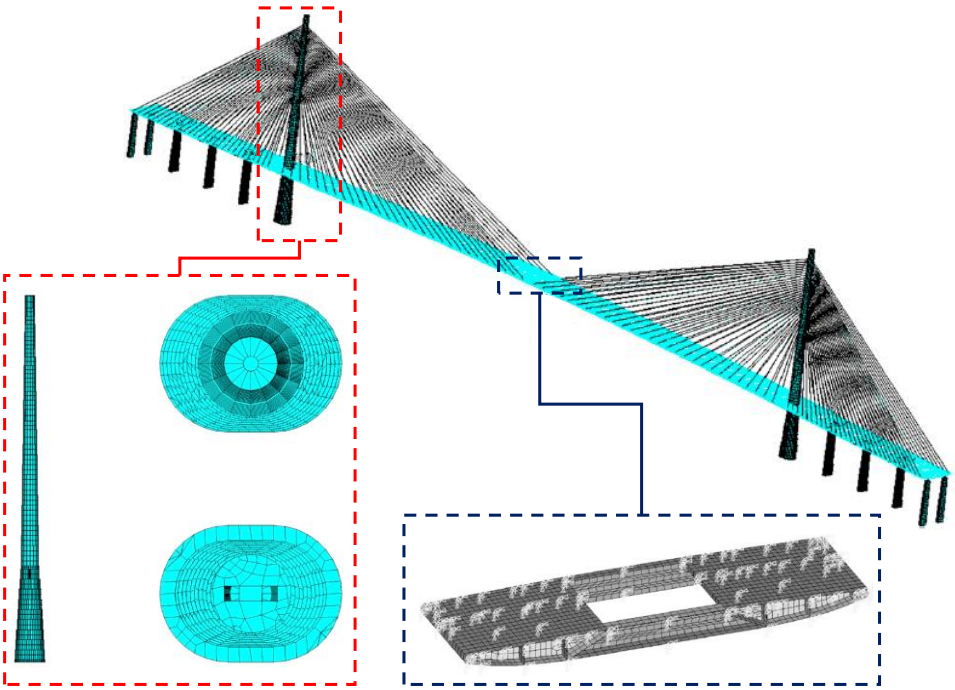

Figure 4.2-2 – MS-FEM of Stonecutters Bridge (Adapted from *Zhu et al., 2014*).

Li et al., 2007 performed MS-FEM of Tsing Ma Bridge in Hong Kong, China for fatigue damage estimation on welded details. The Authors also investigated the effectiveness of coupled and uncoupled damage models in interpreting detected fatigue cracks. Finally, *Mashayekhi & Santini-Bell, 2020* developed a MS-FEM for fatigue assessment of bridges via hotspot stress method. By simulating the dominant traffic scenarios of the bridges, the Authors derived stress histories on welded details and hence estimated remaining fatigue life.

4.3 Main features of the proposed methodology

The proposed methodology for fatigue assessment of steel bridges via MS-FEM is illustrated in Figure 4.3-1.

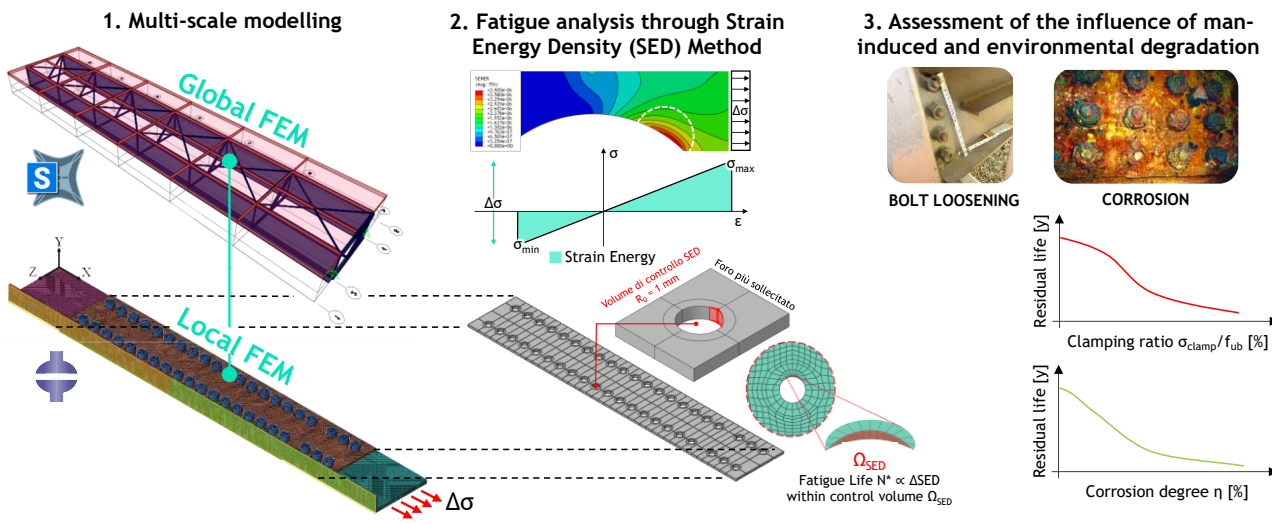

Figure 4.3-1 – Proposed methodology for fatigue assessment of steel bridges via MS-FEM.

Step 1 is represented by global modelling of the bridge through 1D frame and/or 2D shell elements. Priority is given to minimizing the computational effort in deriving influence lines (ILs) on critical members (e.g., bending moment ILs on main girders in correspondence of joints, axial force ILs on truss transverse beams, etc...). Fatigue analysis in terms of internal forces is hence performed by using equivalent truck loads as prescribed in Fatigue Load Model 4 (FLM4) encoded in EN1991-2. Nominal stress histories on details are hence derived based on cross-section properties, i.e., combining effects (e.g., M + N) when necessary.

Subsequently, stress histories can be conveniently reduced to a set of equivalent demand stress ranges $\Delta\sigma_{Ed,i}$ via the well-known Rainflow Method encoded in EN1993-1-9. Such demand values are used as inputs for local, refined FEM modelling of critical details (Step 2). Fatigue analysis is performed through numerical application of the Strain Energy Density (SED) method, the principles of which are outlined in subSection 4.4.

In order to assess the influence of man-induced and environmental degradation, local FEMs are parametrized and suitably manipulated to simulate corrosion, clamping loss, etc… (Step 3, see §4.6 for further details). Parametrization allows time-dependant assessment of residual bridge life based on traffic and inspection data.

Insights about each of the described aspects are provided in the following.

4.4 Principles of the Strain Energy Density method

The Strain Energy Density (SED) method was first introduced by *Lazzarin & Zambardi, 2001*, which first noticed that applying stress-based approach to fatigue analysis would lead in many cases to the prediction of a higher fatigue strength as respect to the value obtained by simply dividing the fatigue limit of a plain specimen by the theoretical value of the stress concentration factor.

This suggested that fatigue failure of notched/drilled components was not governed by the notch (hot-spot) stress, but rather by an averaged stress over a finite neighborhood of the notch tip. The Authors dealt with this aspect via an energetic formulation. Accordingly, an energetic, stress-related parameter was introduced to describe fatigue and fracture behavior of notched components, i.e., the averaged strain energy density (ASED or $\overline{W}$) over a control volume Ω_{SED} centered at (or nearby) the notch tip (see Figure 4.4-1 and (4.4-1):

$$\overline{W} = \frac{1}{\Omega_{SED}} \int_0^{\varepsilon_{ij}} \sigma_{ij}\, d\varepsilon_{ij} \quad [\text{over } \Omega_{SED}] = \frac{\sigma_{ij}\, \varepsilon_{ij}}{2\, \Omega_{SED}} \tag{4.4-1}$$

with σ_{ij} and ε_{ij} being the notch stress and strain components, respectively.

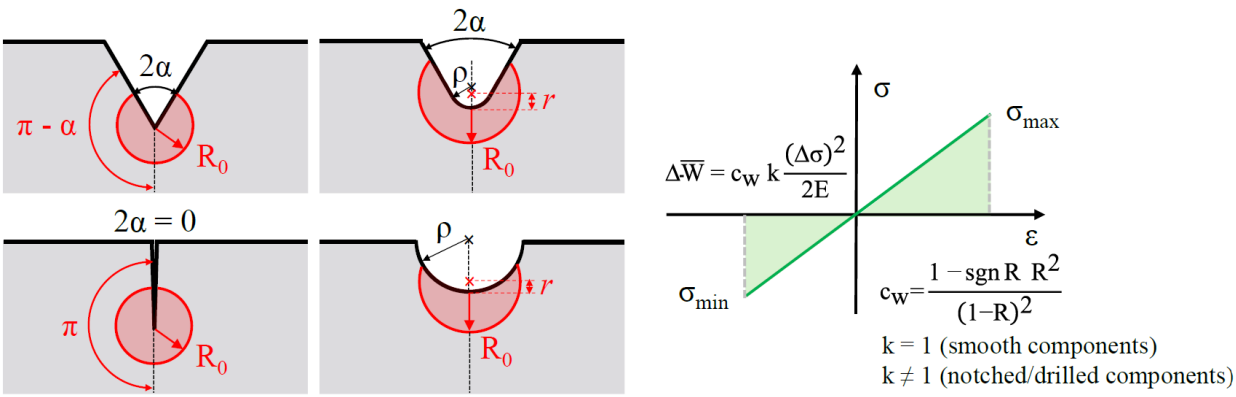

a)

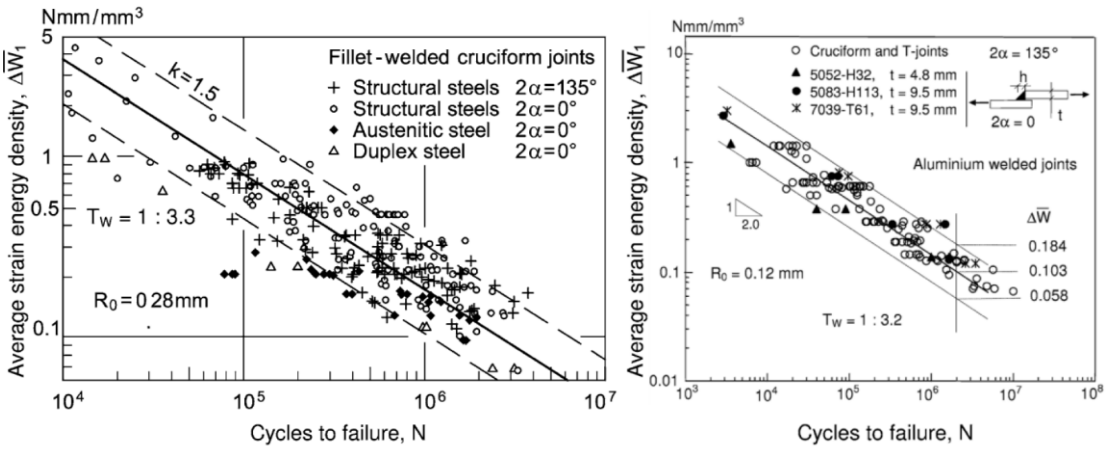

b)

Figure 4.4-1 – *a*) Control volumes for typical notched components and mechanical significance of ASED parameter and *b*) application of SED method to steel and aluminum fillet welded joints (Adapted from *Berto & Lazzarin, 2014*).

Shape and size of the control volume Ω_{SED} were determined based on theoretical considerations related to the stress distribution around the notch tip. Accordingly, a single material parameter (control volume radius R_0, see Figure 4.4-1a) is required to address ASED calculations.

In monotonic conditions, fracture is predicted to occur when a critical ASED value $\overline{W}_C$ is attained. For an ideally elastic, isotropic and brittle material having ultimate tensile strength (UTS) equal to f_u and Young Modulus equal to E_m, critical ASED can be directly estimated as follows (Equation (4.4-2)):

$$\overline{W}_C = \frac{f_u^2}{2\,E_m} \tag{4.4-2}$$

As for the relevant case of fatigue collapse, SED method can be successfully applied by introducing the *ASED range* $\Delta\overline{W} = \overline{W}_{max} - \overline{W}_{min}$ as a fracture indicator (*Berto & Lazzarin, 2014*). To this end, the well-known Basquin's formula can be conveniently expressed in terms of $\Delta\overline{W}$ as follows (Equation (4.4-3)):

$$N_f = C_{SED}\,(\Delta\overline{W})^{-m_{SED}} \tag{4.4-3}$$

with C_{SED}, m_{SED} being empirical parameters to be derived on a case-by-case basis.

Fatigue analysis through $\Delta\overline{W}$ parameter was successfully applied to a bulk of more than 900 experimental tests on fillet welded cruciform joints, both made of steel and aluminium (see Figure 4.4-1b).

It is worth mentioning that, differently from typical assumptions for fatigue analyses (e.g., referring to fully-reversal loading, stress ratio $R = \sigma_{min}/\sigma_{max} = -1$), ASED fatigue approach assumes zero-to-tension loading as a reference condition, i.e., R = 0. Nevertheless, mean-stress effect can be explicitly accounted for by means of a non-dimensional *prestress coefficient* c_w depending on the stress ratio as follows (Equation (4.4-4)):

$$\Delta\overline{W}|_{R\neq 0} = c_w\,\Delta\overline{W}_0 \qquad c_w = \frac{1 - \mathrm{sign}(R)\,R^2}{(1 - R)^2} \tag{4.4-4}$$

c_w can be graphically regarded as the ratio among the areas underlying stress-strain curves (that is, $\Delta\overline{W}$), bounded by the same stress range $\Delta\sigma$ but for $R \neq 0$ and $R = 0$, respectively. Notably, the above Equation yields $c_w = 1$ for zero-to-tension loading (R = 0) and $c_w = 0.5$ for fully-reversal loading (R = –1).

By recalling the well-known quadratic dependence of strain energy (variations) on applied stress (ranges), the above energy-based calculations can be easily expressed in terms of stress-equivalent results, thus enabling the use of properly calibrated S-N curves for each detail.

4.5 Multi-scale modelling of steel bridges for SED applications

4.5.1 Insights about global modelling and global-local interaction

In the proposed methodology, global FEMs are typically developed in SAP2000. All members are modelled via one-dimensional frame or two-dimensional shell elements (see Figure 4.5-1). In the relevant case of built-up or coupled members (e.g., typically found in railway bridges), equivalent cross-sectional properties (i.e., derived with a fiber model) can be introduced as *i*) this results in a significant reduction of the computational effort and *ii*) actual members' geometry and response can be later addressed via refined local FEMs.

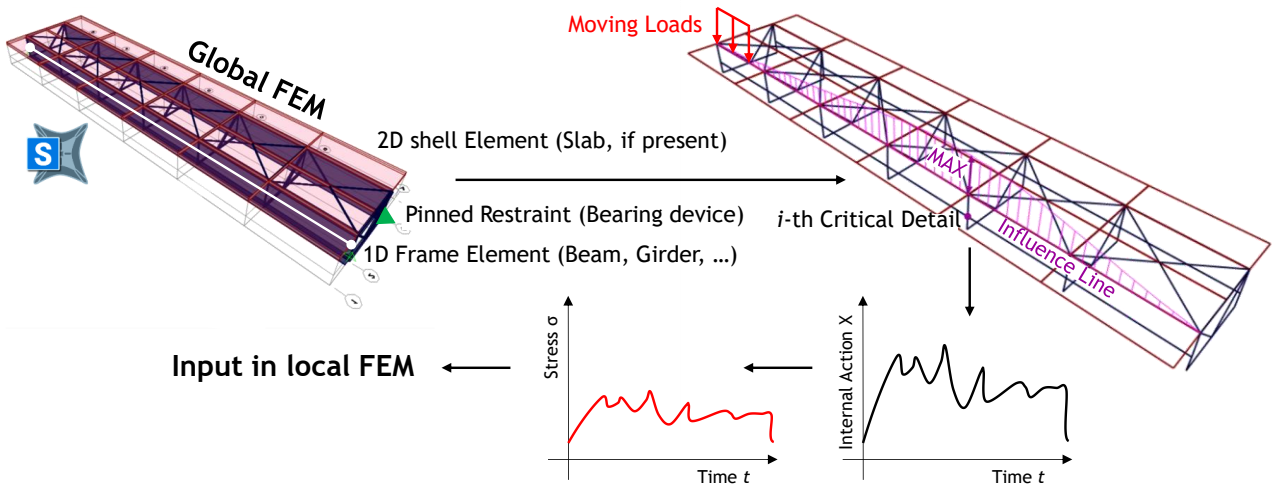

Figure 4.5-1 – MS-FEM of steel bridges for SED applications: Global modelling.

An approximate estimation of connections behavior can be performed via provisions encoded in EN1993-1-8. This enables the introduction of internal releases at member ends wherever required (e.g., in case of shear tab connections, truss KT joints, etc…). Moreover, proper restraints (i.e., typically pins and rollers) have to be introduced at the spans' ends to reproduce the intended structural scheme.

Internal action histories for critical connections are estimated through moving load analysis, i.e., based on ILs on members of interest. Dynamic load amplification should be considered depending on relevant factors (e.g., road roughness and span length for road bridges, train speed and span length for railway ones). For this purpose, a suitable dynamic factor φ can be used to amplify equivalent fatigue loads encoded in EN1991-2.

The collaboration among global and local models, i.e., the core of MS-FEM, is established by adopting the Rainflow processed stress histories as inputs for the energetic calculations.

4.5.2 Insights about local modelling and SED-based fatigue assessment

Once global FEAs outcomes have been derived, local FEMs for SED-based assessment of details are developed in ABAQUS environment (see Figure 4.5-2). Critical details can be conveniently chosen based on global FEMs results. For instance, parts in which *i*) non-negligible mean tensile stresses due to gravity loads and *ii*) significant stress histories due to traffic loads should be selected.

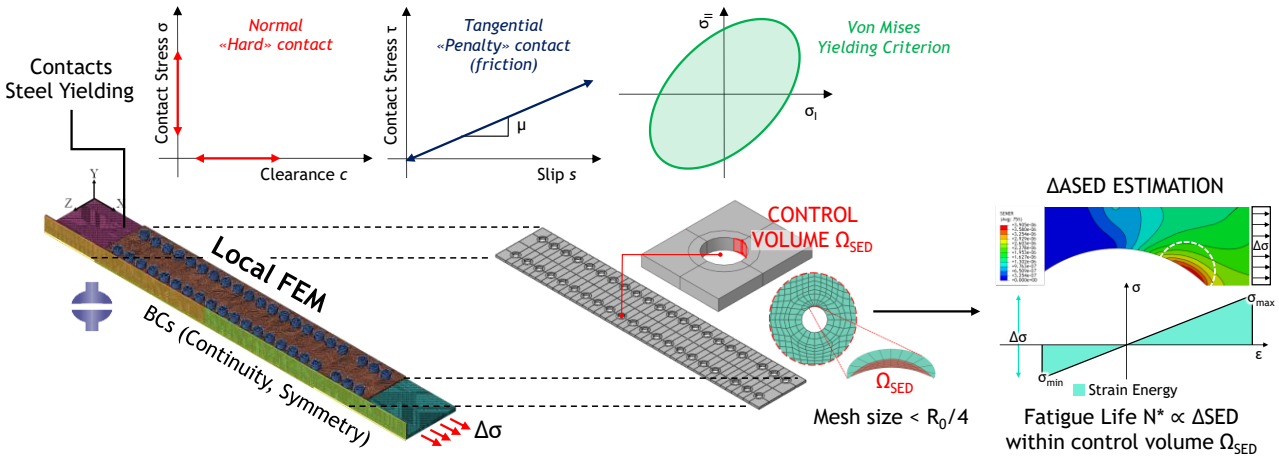

Figure 4.5-2 – MS-FEM of steel bridges for SED applications: Local modelling.

As first shown by *Lazzarin et al., 2010*, FEM can be suitably used to estimate $\Delta\overline{W}$ values. To this end, it is worth recalling that common finite elements (e.g. *solid bricks*, either *8-node linear* or *20-node quadratic* ones) feature displacement-based formulations. Therefore, calculated stresses (i.e., recollected in a stresses vector $\boldsymbol{\sigma}$) are strongly mesh-sensitive.

Contrariwise, strain energy density is directly estimated based on the vector of nodal displacements $\boldsymbol{\delta}$. Therefore, significantly coarser meshes can be used for ASED calculations with respect to stresses, as nodal displacement values are "exact" quantities within the framework of the FE method.

A further improvement in terms of computational effort for estimating $\Delta\overline{W}$ values is given in the work of *Foti et al., 2020*. Indeed, as mentioned in the previous subSection, the estimation of strain energy requires the knowledge of the spot in which the largest principal stresses σ_I are attained. Therefore, the definition of the control volume Ω_{SED} is usually done after a preliminary FEA devoted to lone stress calculations. The Authors overcame this issue by introducing the so-called *free mesh* SED estimation technique.

Accordingly, if free mesh (i.e., with no partitioned control volume) is adopted, accurate ASED estimations can be still achieved, provided that *i*) *quadratic* solid or shell elements are used and *ii*) the mesh size *s* in the neighbourhood of the notch tip is smaller or equal than $R_0/4$. To this end, it is worth reporting that typical R_0 values for non-welded steel details are in the range ≈ 0.7 – 1 mm, while for the heat affected zone of welded details R_0 = 0.28 mm can be used (*Radaj & Vormwald, 2013*), and hence *s* should be selected compliantly.

In order to balance computational effort and accuracy of analyses, geometrical and mechanical symmetries in critical details can be exploited, if appropriate. Structural continuity shall also be restored after sub-assemblage. These tasks are easily accomplished by means of proper boundary conditions (BCs). SED-based assessment of details can be hence investigated by applying surface pressures with magnitude $\Delta\sigma$ at members' ends.

The von Mises criterion can be adopted to model steel yielding, while proper kinematic and/or isotropic models can be used to account for strain hardening (see e.g., *Dutta et al., 2010*). To this end, materials' mean strength values should be adopted in compliance with indications from original design reports, if retrievable.

A strong attention has to be paid to contact among adjacent parts, as it represents the main source of non-linearity in fatigue conditions, i.e., as yielding and geometrical effects are usually negligible. To this end, "surface-to-surface" interactions can be introduced among adjacent parts. Both normal and tangential behaviour shall be accounted for by means of "hard contact" (i.e., rigid interface, no-tension) and "penalty" formulations, respectively (with a friction coefficient μ = 0.3 being suitable for steel).

4.6 SED-based assessment of the influence of man-induced and environmental degradation

One of the main simplified assumptions of the proposed methodology is to neglect the effect of man-induced and environmental degradation on the global behavior of CIs of concern. This simplification can be considered realistic for steel bridges in service, i.e., in which phenomena as clamping loss or metallic corrosion are characterized by a strong degree of localization. Moreover, due to the typical lack of redundancy of adopted structural schemes, the possible reduction of axial, bending and/or shear stiffness due to degradation would have a limited effect on internal action histories in any case.

This hypothesis enables the manipulation of the lone local FEM for the SED-based assessment of CIs. This results in a significant saving of time if refined models are properly parametrized as a function of degradation phenomena to be investigated.

With reference to man-induced degradation, the present subSection is focused on clamping loss, i.e., the reduction of pre-tightening in high-strength bolts due to vibrations induced by repeated traffic loads. Clamping loss can be strongly detrimental for the fatigue performance of connections due to the reduction of plies prestressing which *i*) reduces the connection stiffness and friction resistance, resulting in an increase of slips and bolt-to-hole contact pressures and *ii*) locally increments the stress ratio, i.e., promoting fatigue failure due to the well-known mean stress effect (*Milone & Landolfo, 2024*).

Clamping loss can be suitably modelled in ABAQUS through the Bolt-Load command, which simulates coaction in bolts due to tightening up to a prescribed value (see Figure 4.6-1a). Therefore, starting from the design value reported in EN1993-1-8 ($\sigma_{clamp} = 0.7\, f_{ub}$, with f_{ub} being the ultimate tensile strength of the bolt), the clamping stress can be reduced up to a null value in the worst case scenario. From a time-depending perspective, different trends of clamping loss can be adopted in analyses. As shown by *Basava & Hess, 1998*, bolt untightening due to vibration is characterized by a clearly non-linear trend which can be approximated by a downward parabola in the logarithmic σ_{clamp} - n space.

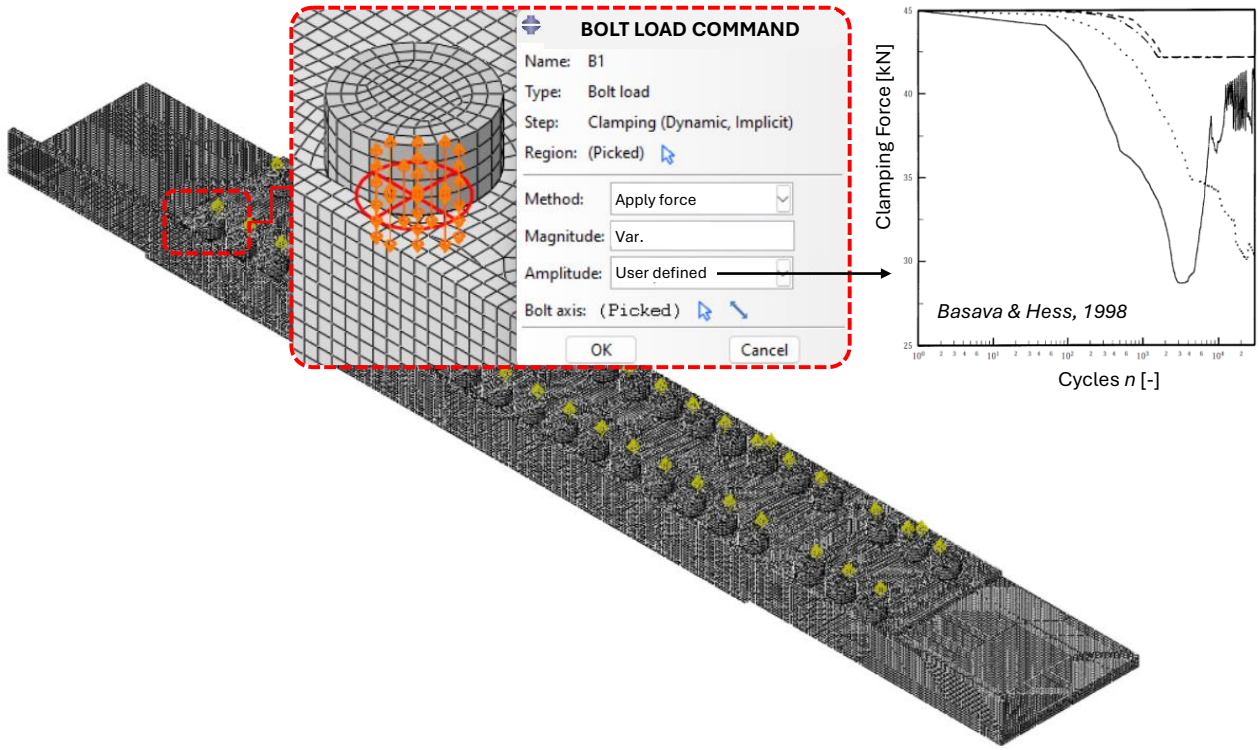

a)

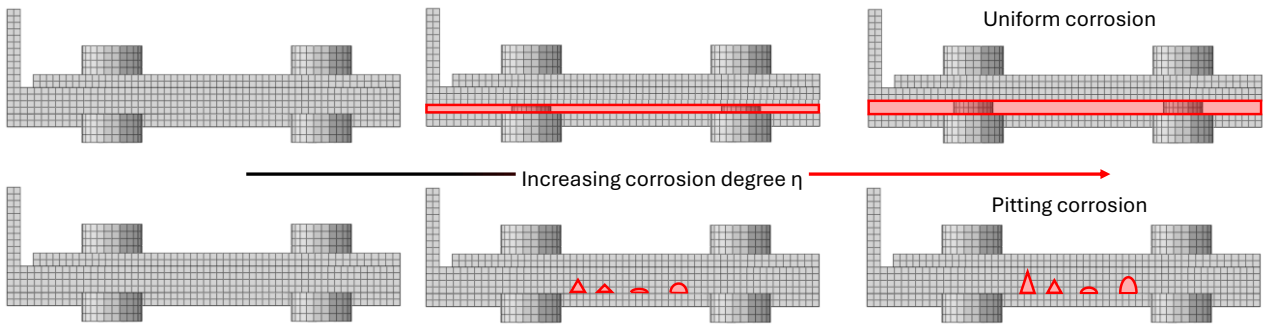

b)

Figure 4.6-1 – Modelling of typical degradation phenomena in steel bridges: *a*) clamping loss, *b*) metallic corrosion.

Nevertheless, in absence of more detailed indications, a (log-)linear reduction of clamping loss in time up to total loss for the assumed value of reference service life can be assumed. Alternatively, a fixed level of clamping loss during fatigue analyses can be assumed for a worst case scenario evaluation.

With reference to metallic corrosion, its effect for a given total corrosion degree η (= $\Delta m/m_0$ with m being the mass of the detail) can be evaluated through a suitable change in the detail geometry. A first, simplified assessment can be done by simply reducing the thickness of corroded parts, i.e., by assuming uniform corrosion on the element of concern (see Figure 4.6-1b).

On one hand, this condition enables an easy parametrization of local FEMs accounting for corrosion. On the other hand, some significant amplification phenomena may be neglected if pitting (i.e., non-uniform corrosion) is overlooked in analyses.

Alternatively, pits can be explicitly modelled as hemispherical or conical voids on the elements surface. If this is the case, the spatial distribution of pits and their depth should be randomly generated on the basis of empirical statistic distributions referred to real case studies. This approach, although enabling an higher level of verisimilitude in corrosion fatigue analyses, has the clear drawback of being very onerous and of requiring consistent experimental data.

Some other, notable options involve *i*) the use of cell automata models to simulate surficial corrosion on steel elements (see e.g., *Contreras et al., 2011*) or *ii*) the accurate reproduction of real corrosion scenarios through scanning and subsequent import in FEM environment (see e.g., *Liu & Kelly, 2019*).

Whichever is the adopted strategy, it is important to highlight that all cases should be governable trough a discrete set of synthetic such as the total corrosion degree η, the elements aspect ratio, etc…

4.7 Applicative example

4.7.1 Generality and geometrical features of the case study

The selected case-study is a double-girder steel-concrete composite bridge located in Naples, Italy. The structure, which was designed according to Italian normative provisions that were in force during 1960s (Circ. 384 14/02/1962), was completed during 1976 and opened to traffic shortly after. Due to its location (i.e., close to a commercial harbour), the structure experienced a significant heavy trucks flow since its opening.

Figure 4.7-1 depicts *a*) main geometrical features for the investigated composite bridge as retrieved in the original design drawings and *b*) a lateral view of the structure with the most critical detail being highlighted.

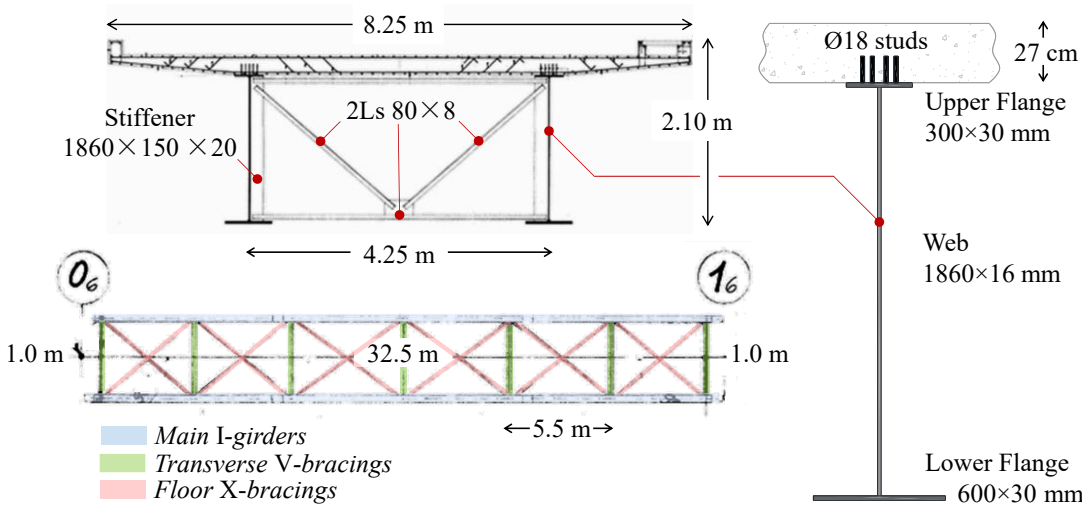

a)

b)

Figure 4.7-1 – Main features of the selected case study: *a*) geometrical features retrieved in the original design report, *b*) front view with the critical double covered joint being highlighted.

The structure, which is simply supported and covers a moderate span of 33 m, is composed of two identical, built-up I-shaped girders (H = 1.90 m) with unequal flanges.

The spacing among such main beams is constant and equal to 4.25 m. The cross-section is completed by a 20 cm thick precast concrete slab (B = 8.25 m). It is worth remarking that such a structural section is representative of a large number of existing road bridges being in service in Italy.

In order to further stiffen the structural system, both transverse and roof bracings (s = 5.5 m) are present, with coupled angle profiles being adopted in both cases.

The roadbed includes a 15 cm thick asphalt layer and a couple of heavy side barriers.

With reference to structural details, main girders are divided into three equal segments, whose structural continuity is restored via double covered joints (DCJs, see Figure 4.7-2) featuring high-strength bolts placed on both the lower flange and across the web. Moreover, braces are connected to main longitudinal members through bolted gusset plate connections. The composite action among steel girders and the upper slab is ensured by Ø18 Nelson studs (in groups of four on each flange, see Figure 4.7-1a).

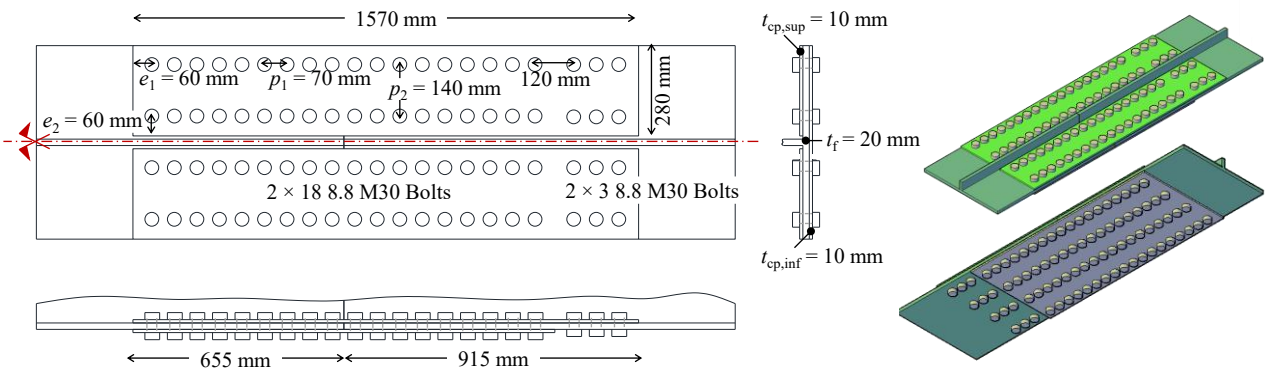

Figure 4.7-2 – Main features of most critical structural detail: longitudinal girder-to-girder DCJ.

4.7.2 MS-FEM of the case study

In compliance with remarks from previous subSections, the coupled global-local MS-FEM of the case study was developed based on retrieved data from drawings and on-site surveys. Namely, global modelling of the steel-concrete bridge was carried out in SAP2000 v.23 (see Figure 4.7-3, global FEM).

Main girders and bracings were modelled through mono-dimensional frame elements, while the upper slab was modelled through 2D shell elements. The degree of connection among structural members was accounted for through members' end releases, whenever relevant. For instance, truss connections among transverse elements and main girders were modelled as internal hinges. Moreover, support provided by either fixed or mobile bearings was modelled through equivalent pin restraints at the span ends.

Global FEM was used to perform to estimate mean stresses σ_m and maximum stress ranges $\Delta\sigma_{Ed,i}$ on details, the cyclic response of which governs the fatigue behaviour of the structure. From this perspective, as anticipated, the lower flange DCJ connecting consecutive segments of the main girders proved to be the most critical component. For fatigue analyses, the following load aliquots were accounted for:

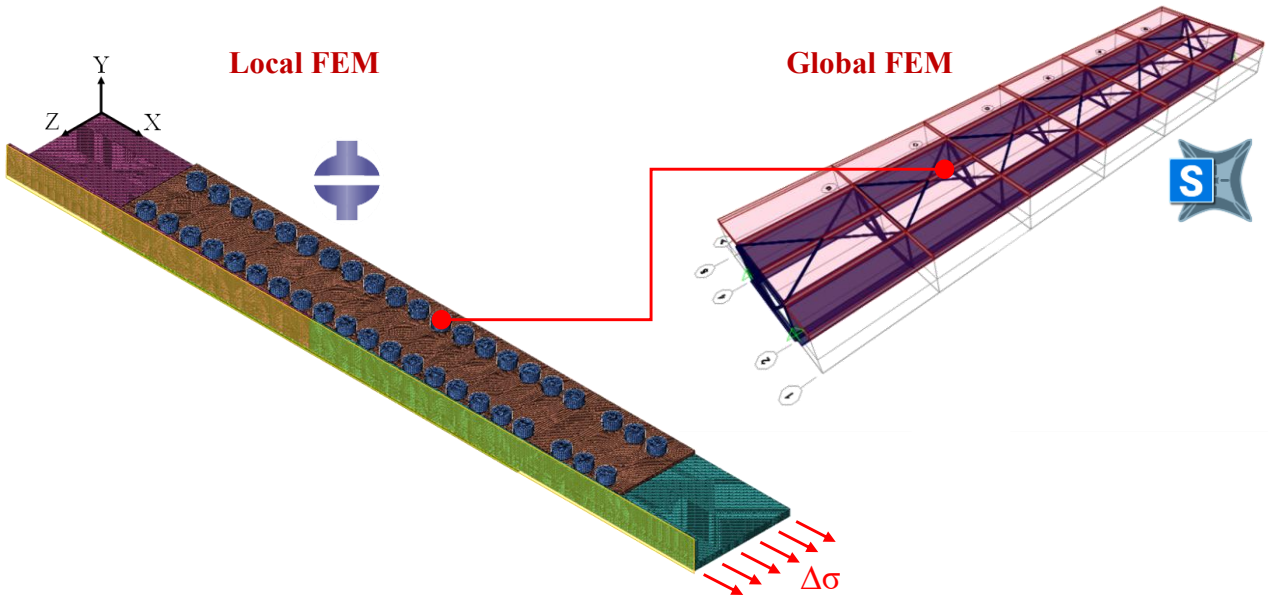

Figure 4.7-3 – MS-FEM of the selected case study.

- Self-weights, estimated assuming an unit weight of 78.5 kN/m^3 and 25.0 kN/m^3 for structural steel and reinforced concrete, respectively;
- Permanent loads, i.e., the asphalt layer (13 kN/m^3) and barriers (0.3 kN/m);
- «Standard» lorries from FLM4.

Subsequently, refined modelling of the DCJ was carried out in ABAQUS (see Figure 4.7-3, local FEM). 3D solid, 20-node brick elements were used to discretize all parts. In order to balance analyses accuracy with the computational effort, the developed local FEM accounted for the joint longitudinal symmetry. Surface contacts and clamping forces in bolts were modelled as described in subSection 4.5.2.

4.7.3 SED-based assessment in pristine conditions

Advanced cyclic assessment of the selected critical DCJ was performed through SED method as discussed in subSections 4.4 & 4.5.2.

As a first step, a "master" $\Delta\overline{W}$-N_f curve was derived for the specific detail of concern (DCJ with preloaded bolts). For this purpose, experimental results from *Razavi et al., 2017* (i.e., 21 tests – excluding runouts – on both uncoated and galvanized symmetrical butt joints with preloaded bolts) were used. According to prescriptions reported in EN1990, the characteristic value (P_F = 5%) of SED-related fatigue strength was used for service life estimations ($C_{SED} = \frac{1}{1514.8}$, m_{SED} = 1.46, see Figure 4.7-4a, b).

Subsequently, FEAs were performed with reference to the critical DCJ. In compliance with remarks reported in *Berto & Lazzarin, 2014*, the control volume for ASED calculations was identified nearby the most stressed hole and suitably picked in the local FEM. A control volume radius R_0 = 1 mm was adopted for European S355 mild steel, and mesh size was hence properly selected based on recommendations from *Foti et al., 2020*.

Compliantly with global FEAs results, Δσ values resulting from the passage of the five equivalent lorries (V1–V5) included in FLM4 were applied at the joint end, i.e., superimposed with clamping forces and static stresses due to self-weight and permanent loads.

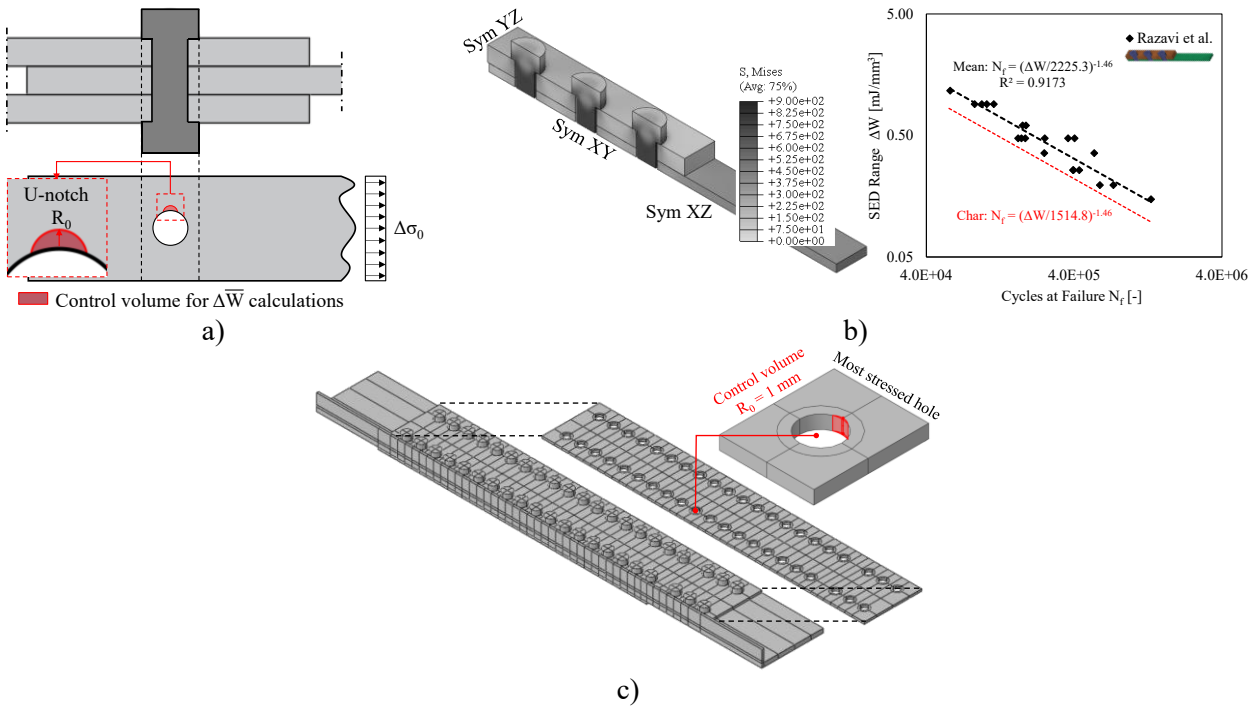

Figure 4.7-4 – SED-based fatigue assessment of the critical detail: *a-b*) derivation of the master fatigue curve from data reported in *Razavi et al., 2017*, *c*) definition of Ω_{SED} for the DCJ.

Results from SED-based assessment of the case study are summarized in Figure 4.7-5 in terms of *a*) outcomes from moving load analyses (stress histories deriving from standard lorries), *b*) ASED ranges estimations based on local FEAs and *c*) residual life estimations carried out through the well-known Palmgren-Miner (PM) rule.

For the sake of comparison, fatigue analysis was first performed with reference to normative provisions reported EN1993-1-9. Accordingly, a detail class DC 112 ($\Delta\sigma_C$ = 112 N/mm^2 for $N_f = 2 \cdot 10^6$ cycles) was selected for the DCJ of concern, with fatigue demand being calculated on the gross cross-section.

In light of its importance within the regional transportation network, an average yearly traffic of $0.5 \cdot 10^6$ heavy trucks was assumed for the bridge in accordance with EN1991-2. A medium-distance frequency distribution of standard lorries was also compliantly assumed. In absence of actual traffic data, a stationary distribution of traffic in time was assumed for residual service life estimations. To this end, the following expression was adopted (Equation (4.7-1)):

$$L_{res} = \frac{1 - \sum_{j=1}^{5} \sum_{i=1}^{L_{ref}} d_{i,j}}{\sum_{j=1}^{5} d_{L_{ref},j}} \tag{4.7-1}$$

where L_{res} is the residual service life, Lref is the reference structural life (= 50 years) and $d_{i,j}$ is the elementary fatigue damage deriving from the passages of the *j*-th lorry during the *i*-th year of service life.

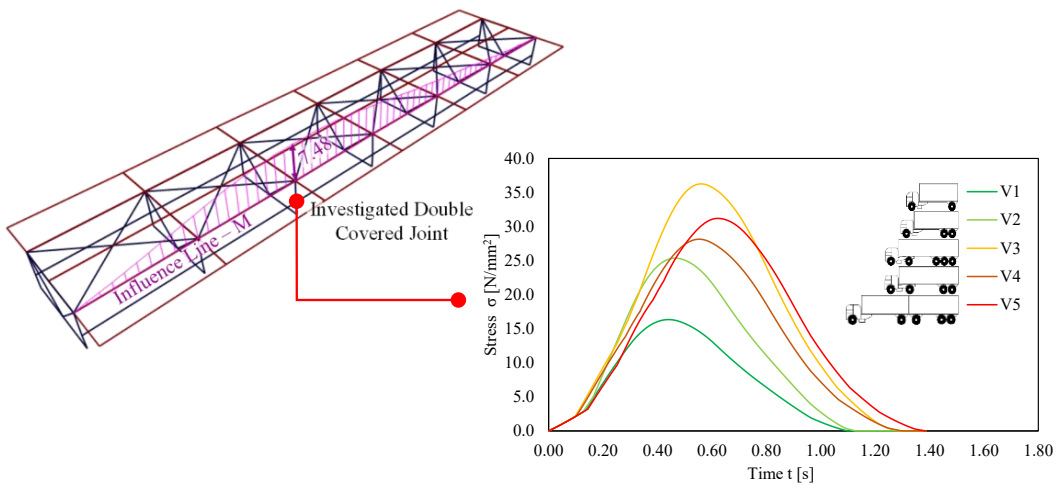

a)

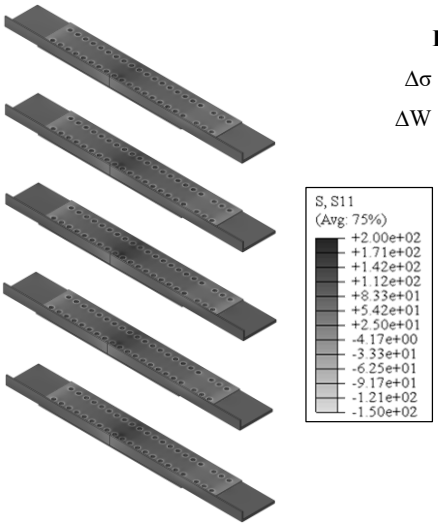

Lorry	V1	V2	V3	V4	V5
Δσ [N/mm²]	16.1	25.2	36.4	27.9	30.8
ΔW [mJ/mm³]	3 E-04	4 E-04	7 E-04	6 E-04	6 E-04

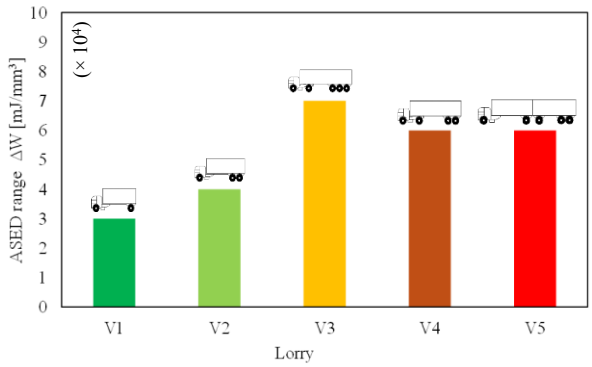

b)

$$D_{TOT} = \sum_i \frac{n_i}{N_i}$$

$$L_{res} = \frac{1 - D_{TOT}}{D_{avg}}$$

Lorry	V1	V2	V3	V4	V5
$Damage_{EC3}$	0.00	0.01	0.11	0.01	0.01
$Damage_{SED}$	0.03	0.01	0.06	0.04	0.01

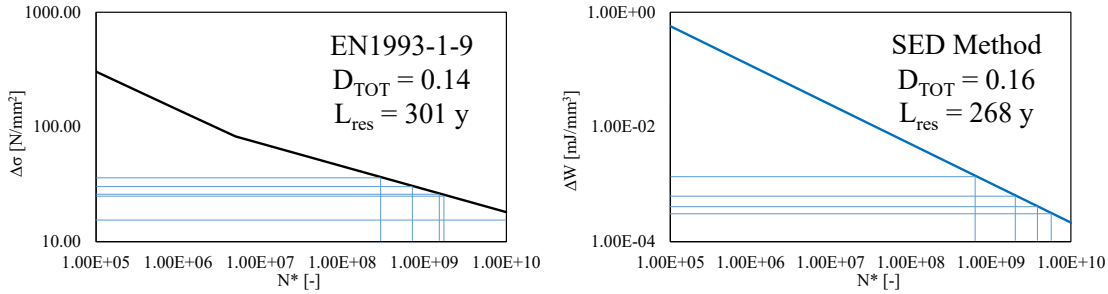

c)

Figure 4.7-5 – SED-based fatigue assessment of the critical detail: *a*) moving load analysis, *b*) estimation of ASED ranges, *c*) residual service life estimation through the PM rule.

With reference to advanced SED-based fatigue assessment, the same input parameters in terms of traffic flow and mean stresses were adopted. Equation (4.7-1) was still used for L_{res} estimations, i.e., by replacing S-N based elementary damage with SED-based elementary damage (see Figure 4.7-5c).

As expected, moderate stress ranges are induced by standard lorries (16–36 N/mm^2, see Figure 4.7-5a), with them being superimposed to a minimum stress of 47 N/mm^2 caused by permanent loads. According to Goodman's criterion, a percentage increment of about 15–18% in terms of fatigue demand is hence required to account for the mean stress effect.

With reference to refined local FEAs, stress and SED analyses confirm how principal stresses parallel to applied loads (S11) always reach their peak value nearby the ninth inner hole of the upper cover plate, that is, in correspondence of the first bolt installed in the right segment of the girder (see Figure 4.7-5b).

This clearly descends from *i*) the rather low thickness of the cover plate itself (half of the flange thickness) and *ii*) the peculiar load transfer mechanism (butt joint in shear). As expected, $\Delta\overline{W}$ values (= 0.03–0.07 mJ/mm^3) increase with increasing values of nominal $\Delta\sigma$.

L_{res} estimations for the critical detail yield a good agreement between results derived in compliance with EN1993-1-9 and with the SED method, i.e., both in terms of total fatigue damage D_{TOT} (0.14 against 0.16) and L_{res} (301 against 268 years), i.e., with the bridge being largely safe against standard fatigue loads. Remarkably, SED method proves to be slightly more conservative, i.e., especially with reference to lighter lorries – which induce negligible damage according to normative provisions.

Therefore, the two approaches can be considered comparable with reference to pristine conditions.

4.7.4 Effect of structural degradation

In order to reproduce a potential joint defectivity due to progressive clamping reduction, four different scenarios of pre-tightening loss were investigated. Accordingly, four different clamping loss scenarios were considered (see Figure 4.7-6):

A) Loss of pre-tightening action in the lone most stressed bolt;
B) Loss of pre-tightening action in three consecutive bolts, including the most stressed one;
C) Loss of pre-tightening action in all bolts surrounding the most stressed one;
D) Loss of pre-tightening in all the bolts.

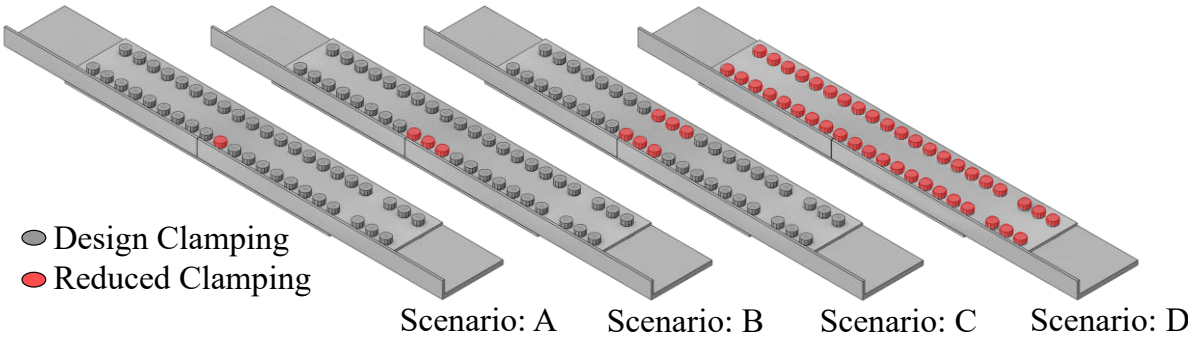

Design Clamping: 0.7× 800 MPa×707 mm^2 = 396 kN
Clamping loss ratios: 0.5 (283 kN), 0.3 (197 kN), 0.0 (0 kN)

Figure 4.7-6 – Clamping loss scenarios considered for the case study.

For each of the above scenarios, progressively lower clamping ratios (50%, 30%, 0%) were considered for SED calculations related to the passage of each standard lorry, resulting in a total of 4×3×5 = 60 refined FEAs.

Relevant residual service life estimations are summarized in Table 4.7-1 and Figure 4.7-7. It can be immediately noticed that, for moderate levels of clamping loss ($\sigma_{clamp}/f_{ub} \geq 0.5$), only a slight increase in terms of fatigue damage is observed, with a reduction of L_{res} in the range 20–25%. Nevertheless, for larger reductions of clamping force, residual life strongly decrease (-40–50% for $\sigma_{clamp}/f_{ub} = 0.3$).

As expected, most critical estimations are achieved when the pre-tightening force is completely lost, with the worst scenario being represented by a simultaneous loss of clamping in all bolts (Case D00, -98%). Nevertheless, it should be remarked that this case represent a lower bound in terms of potential fatigue performance, as contemporary and total untightening of all bolts in a DCJ due to traffic and vibrations is highly unlikely.

Interestingly, in other scenarios, similar degrees of L_{res} reduction are attained for the same value of clamping stress ratio, although a detrimental interaction among group of untightened bolts can still be observed. Such effect is more pronounced for $\sigma_{clamp}/f_{ub} \leq 0.3$. This descends from the localized reduction of friction resistance, which induces a modification of load transferring mechanism for bolts in shear.

Table 4.7-1 – SED-based fatigue assessment of the case study: total fatigue damage and residual service life for each considered clamping loss scenario.

CASE	**REF**	**A05**	**A03**	**A00**	**B05**	**B03**	**B00**	**C05**	**C03**	**C00**	**D05**	**D03**	**D00**
Lorry							d_{ij}						
V1	0.03	0.04	0.05	0.06	0.04	0.05	0.06	0.04	0.05	0.09	0.04	0.04	0.13
V2	0.01	0.02	0.03	0.03	0.02	0.02	0.03	0.02	0.02	0.05	0.02	0.02	0.08
V3	0.06	0.07	0.10	0.11	0.07	0.09	0.12	0.07	0.10	0.18	0.07	0.09	0.33
V4	0.04	0.05	0.07	0.08	0.05	0.07	0.08	0.05	0.07	0.12	0.05	0.06	0.28
V5	0.01	0.01	0.02	0.02	0.01	0.02	0.02	0.01	0.02	0.04	0.01	0.02	0.07
D_{TOT}	0.16	0.19	0.27	0.30	0.20	0.24	0.31	0.20	0.25	0.48	0.20	0.24	0.89
L_{res} **[y]**	268	213	134	117	206	156	110	205	148	55	203	162	6

REF: Reference scenario (no clamping loss)
XYY: Clamping loss scenario X (= A, B, C, D) – Clamping ratio σ_{clamp}/f_{ub} YY (= 0.5, 0.3, 0.0)

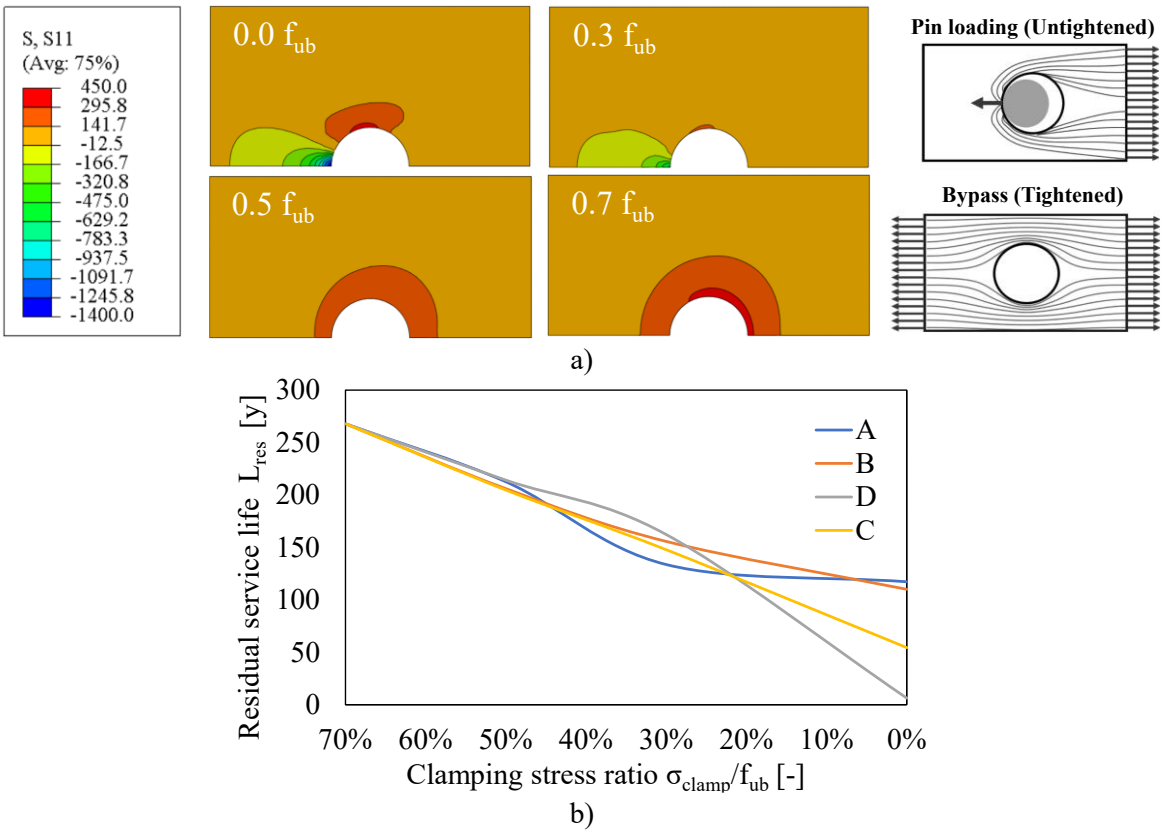

Figure 4.7-7 – Effect of clamping loss for the selected case study: *a*) alterations in load transfer mechanism and *b*) progressive reduction of residual service life.

4.8 Derivation of structural fragility using multi-scale modelling

As summarized in the previously, MS-FEM can be used to effectively and efficiently assessing the fatigue performance of steel/composite bridges affected by ongoing degradation phenomena. Nevertheless, each application of the proposed strategy leads to a single, time-depending trend of corrosion fatigue damage D(t), which strictly depends on the assumed evolution of environmental and man-induced degradation. This limitation can be overcome by introducing some simplified, yet plausible assumptions to account for alternative degradation paths which share a same intensity measure (IM – e.g., the maximum corrosion degree η_{MAX} or clamping loss $\Delta\sigma_{clamp,MAX}$ at the end of the reference service life V_{REF}), and hence estimate the conditioned failure probability for increasing IM values (fragility function P(D > 1| IM, t, V_{REF} … - with e.g., IM = η_{MAX}, $\Delta\sigma_{clamp,MAX}$, …). In the following analytical developments, a power trend with variable convexity is assumed for the evolution of degradation phenomena (see Figure 4.8-1):

$$\left(\frac{\mathrm{IM}}{\mathrm{IM}_{\mathrm{MAX}}}\right) = y = x^n = \left(\frac{t}{\mathrm{V}_{\mathrm{REF}}}\right) \tag{4.8-1}$$

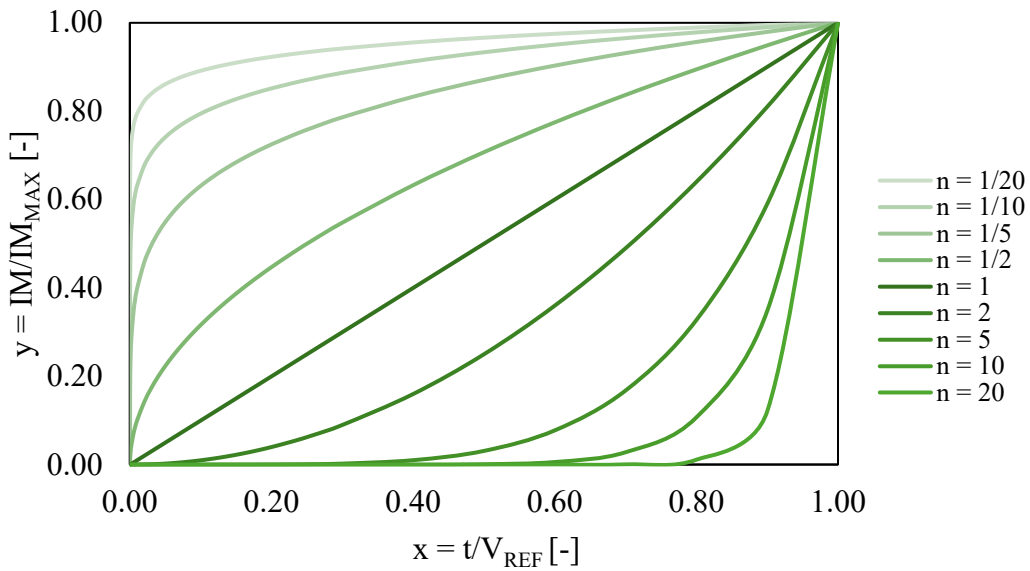

Figure 4.8-1 –Examples of normalized parametric trends for degradation evolution.

For each assumed trend, total corrosion fatigue damage $D_{max} = f(n, IM_{MAX,1}, IM_{MAX,2}, \ldots, t = V_{REF})$ is estimated on the basis of SED calculations and hence arranged in a *m*-dimensional matrix **[D]**, in which 1 degree of freedom (DOF) is assigned to *n* and the other *m* – 1 DOFs are associated to IM values. An example of such mathematical structure is depicted in Figure 4.8-2 with reference to the simplest case of a single degradation source (e.g., steel corrosion). In this case, the maximum value of corrosion at the end of fatigue life η_{MAX} varies along each column, while convexity parameter *n* varies along consecutive rows. Scenarios (e.g., matrix cells) associated with expected failure ($D \geq 1$) are highlighted in red.

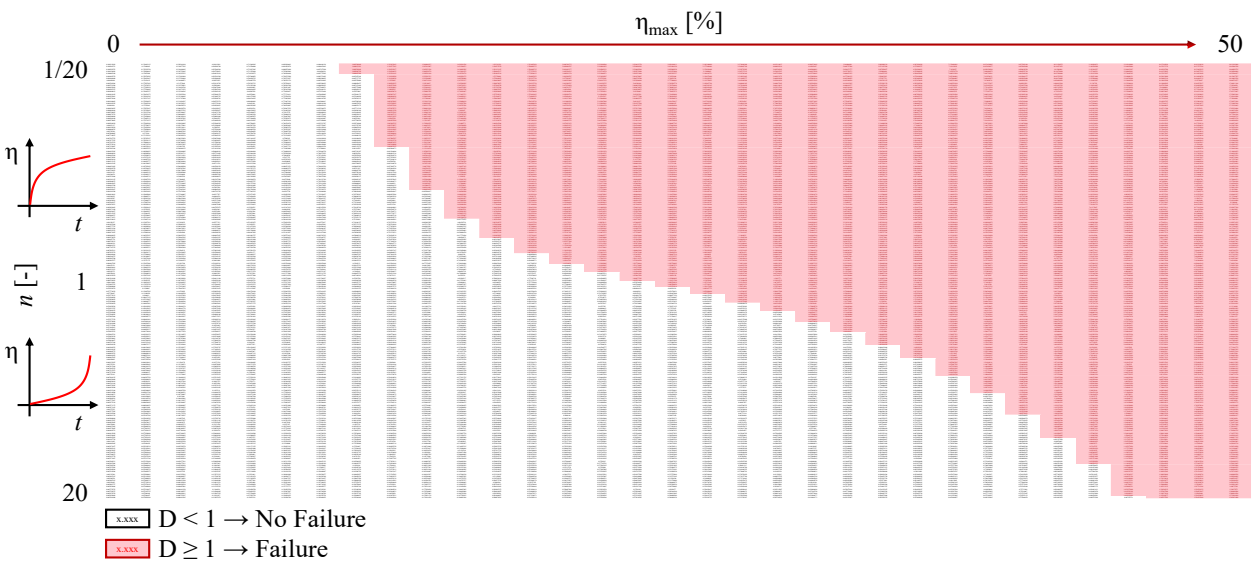

Figure 4.8-2– Damage matrix **[D]** in case of corrosion-depending degradation.

Two alternative approaches can be hence used to derive structural fragility based on the estimated damage matrix, e.g., a frequentist approach or a distribution-based approach. Relevant details are discussed in following.

4.8.1 Frequentist approach for fragility derivation

The simplest option to assess structural fragility starting from the damage matrix is to directly exploit the concept of event probability, i.e., by counting – for a given IM_{MAX} value – the number of scenarios n_{fail} |

IM_{MAX} in which $D \geq 1$ is achieved and dividing it for the total number of relevant scenarios n_{TOT} (i.e., which coincides with the dimension of the chosen set of possible values of n – see Figure 4.8-3).

$$P(D > 1 \mid IM = IM_{MAX}, V_{REF}) = \frac{n_{fail} \mid IM_{MAX}}{n_{TOT}} \tag{4.8-2}$$

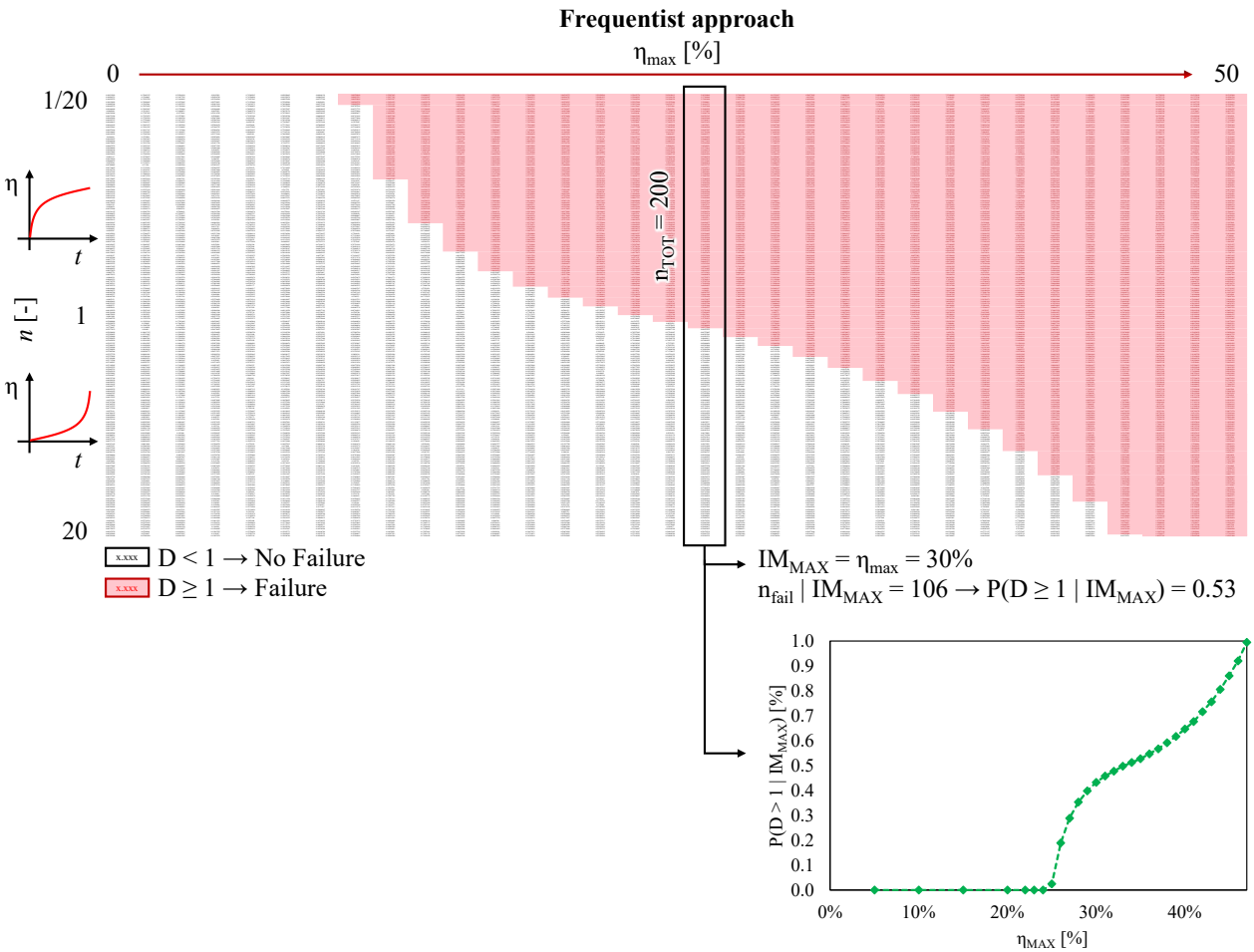

Figure 4.8-3 – Example of application of the proposed frequentist approach.

As a result, a point-by-point fragility function is obtained for increasing values of IM_{MAX}. In best scenarios, $n_{fail} \mid IM_{MAX} = 0$, while in worst ones (i.e., the ones associated with largest values of IM_{MAX}), $n_{fail} \mid IM_{MAX} = n_{TOT}$ is obtained, and hence the relevant probability is consistently bounded between 0 and 1. If needed, a parametric distribution (i.e., normal or lognormal) can be used to best-fit derived points, although non-convex probability trends could be obtained and should be addressed carefully. Indeed, after reaching a "critical" IM value IM* (i.e., the one associated with D = 1 for n = 1), the failure probability typically rises very sharply and hence stabilize until very large (and implausible) values of IM_{MAX} are assumed.

4.8.2 Distribution based approach for fragility derivation

A more robust statistical interpretation of the damage matrix can be obtained by using a distribution-based approach for fragility assessment (see Figure 4.8-4).

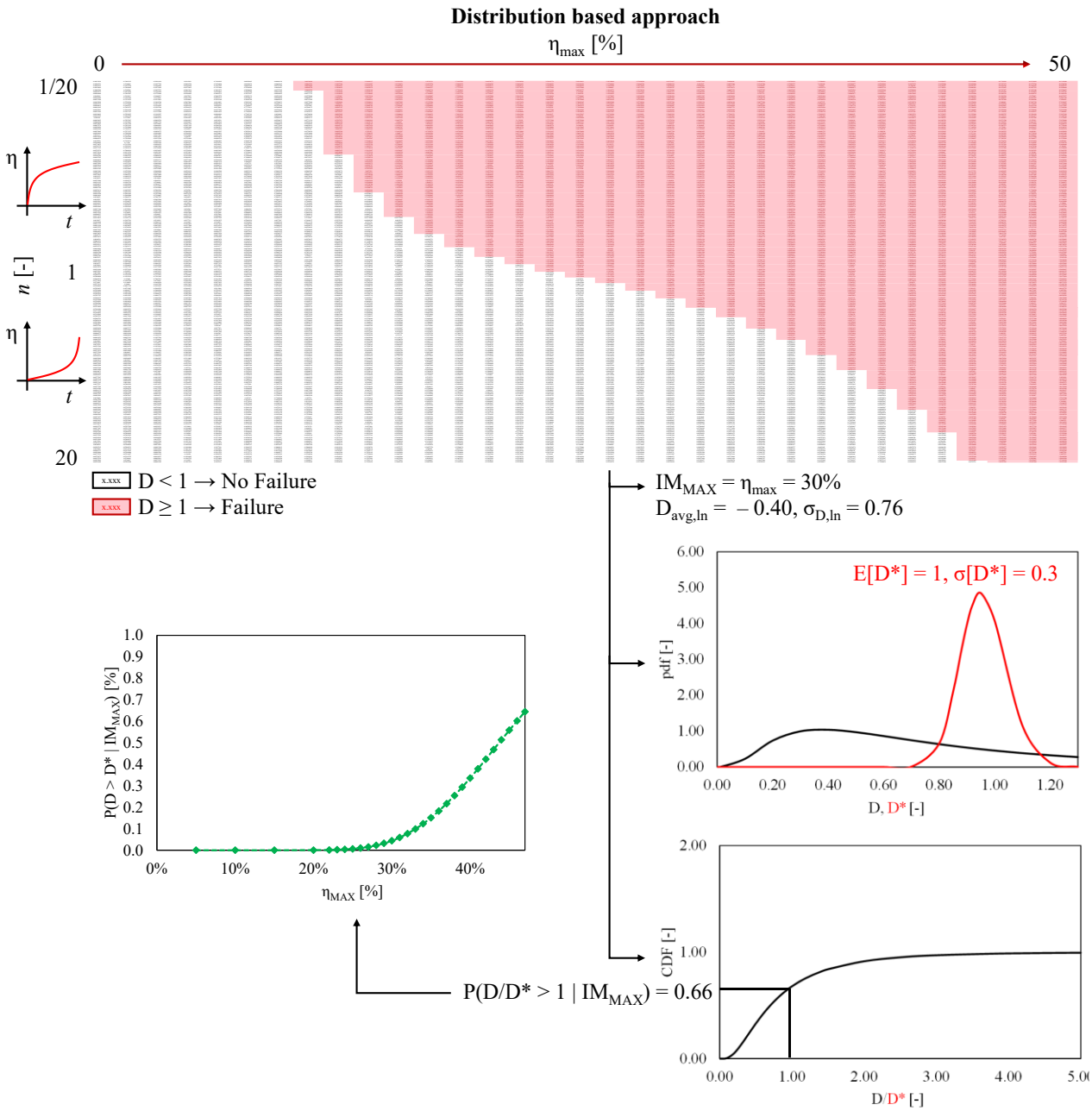

Figure 4.8-4 – Example of application of the proposed distribution-based approach.

Accordingly, for each column of **[D]**, the average value $D_{avg,ln} \mid IM_{MAX}$ and the relevant standard deviation $\sigma_{D,ln} \mid IM_{MAX}$ of the natural logarithm of damage is first estimated according to:

$$D_{avg,ln} \mid IM_{MAX} = \frac{\sum_{i=1}^{n_{TOT}} \ln D_{max,i} \mid IM_{MAX}}{n_{TOT}}$$

$$\sigma_{D,ln} \mid IM_{MAX} = \sqrt{\frac{\sum_{i=1}^{n_{TOT}} (\ln D_{max,i} \mid IM_{MAX} - D_{avg} \mid IM_{MAX})^2}{n_{TOT} - 1}} \qquad (4.8\text{-}3)$$

Damage for a given value of IM_{MAX} is hence assumed to behave as a lognormally distributed random variable $D \mid IM_{MAX} \sim LN(D_{avg,ln} \mid IM_{MAX}; \sigma_{D,ln} \mid IM_{MAX})$.

A similar assumption is hence made with reference to failure threshold. Namely, according to *Zhu et al. (1995)*, the threshold value D* after which fatigue failure for variable amplitude loadings is obtained should not be fixed (D* = 1), i.e., as its logarithm rather behaves as a normally distributed variable with unitary expected value and non-negligible scatter – ln D* ~ N(1; 0.3). By exploiting basic properties of lognormal distribution, it can be immediately observed that the demand/capacity ratio D/D* behaves as a lognormal variable as well, i.e., with expected value $E(D/D^*) = D_{avg,ln} \mid IM_{MAX}$ and standard deviation $\sigma(D/D^*) = \sqrt{\sigma^2_{D,ln} \mid IM_{MAX} + \sigma^2_{D^*}}$. Therefore, for a given value of IM_{MAX}, structural fragility can be hence derived as the probability of D/D* > 1 given its parametric definition. Also in this case, the resulting fragility function is obtained by points, and a parametric distribution (i.e., normal or lognormal) can be used to best-fit derived points is deemed relevant. Nevertheless, careful attention is needed with this approach as well, i.e., as the assumption of homoskedasticity of D/D* (i.e., constant scatter) for increasing values of IM_{MAX} is typically not satisfied.

4.9 Applicative example: POC2 Cadore Bridge

In this Section, the discussed MS-FEM based methodologies to estimate corrosion fatigue-related strutctural fragility are applied with reference to a representative case study, i.e., the Cadore Bridge over Piave River, which belongs to the POC2 (SS51 Alemagna) developed within the EP RETURN Project. All relevant details are discussed in the following.

4.9.1 Generalities

The Cadore bridge is a 272 m long, full-steel orthotropic steel deck (OSD) bridge. This bridge belongs to a series of viaducts erected to improve the viability on the Alemagna State Road 51 (i.e., one of the CIs selected as POC2 within RETURN project) between mountainous areas of Treviso, Belluno and Bolzano provinces. Cadore bridge crosses the Piave river in the locality of Perarolo di Cadore (BL – see Figure 4.9-1).

Figure 4.9-1 – Geolocalization and lateral view of the Cadore Bridge in Perarolo di Cadore (BL).

Being designed by Matildi Engineering firm and built by the Cimolai Costruzioni company in about three years – Cadore bridge was opened to traffic in 1985. The relevant, global structural scheme involves an arch-frame arrangement, i.e., with two pairs of box-shaped steel piers inclined of ≈ 40°, (H = 55 m, variable section). The deck is divided into a central span (L = 128 m) and two lateral spans (L = 72 m). It features a

double box section with variable dimensions along the bridge length (H = 6 m). The upper box constituting the road platform is composed by a 13.3 m wide open-stiffener orthotropic slab, the upper plate of which is in direct contact with the asphalt layer without the presence of any concrete slab. All the described plate elements and profiles described above are made of self-passivating steel.

4.9.2 Constructional details

Due to well-known complex geological conditions, Cadore bridge foundations had to be conceived as light as possible. This, in conjunction with the considerable span to be crossed (272 m), lead to the definition of the mentioned arch-frame scheme in place of a bulkier arch scheme. The longitudinal bridge profile exhibits a slope of ≈5% (ΔH ≈ 15 m among the two ends of the bridge). The structure is restrained on four sides, i.e., at the base of each couple of piers and at the deck ends. In the first case, fixed hinge restraints were adopted, and appropriate structural details were developed (see Figure 4.9-2a). As for deck restraints, a fixed hinge was adopted on Tai side, while the other side was equipped with a roller, i.e., leaving the deck free "to breathe" under thermic excursions.

Transferring of horizontal actions from deck to piers to abutments was aided through special girders (steel-concrete composite “tie-girders” equipped with anti-seismic devices), which were also crucial in the assembly phase of both the pier legs and relative semi-girders.

As for cross-sections of the arch-frame system, the deck girder features a double box section (W = 6.60 m, H = 6 m in the central span, H = 3 ÷ 6 m in side spans – see Figure 4.9-2b). The 13.3 m wide is made with an open-stiffener orthotropic plate composed by transverse sheets spaced at a distance of 3 m and 0.3 m spaced flat ribs placed longitudinally. In the same fashion, the webs and the bottom flange of the lower box (core) are also stiffened by transverse sheets (p = 3 m) and longitudinal flat ribs (webs)/half-IPE segments (flange). Transverse stiffening system is completed by X-braces made of coupled L profiles, (p = 6 m).

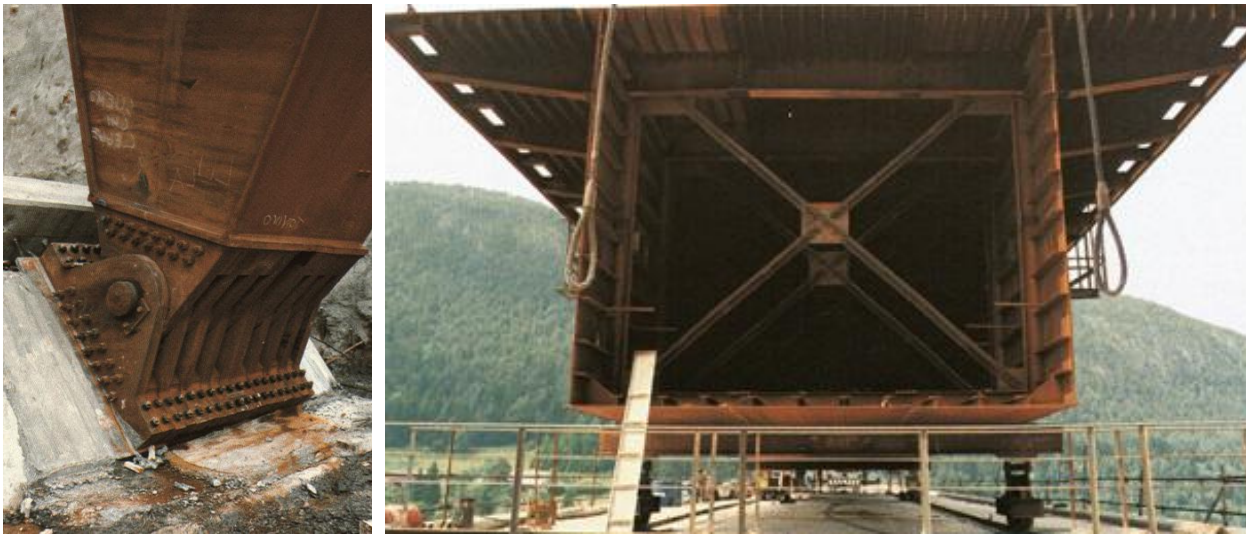

Figure 4.9-2 – Structural details of Cadore bridge: a) base hinge, b) central span OSD.

With regards to piers, each one is made up of a pair of legs inclined along both main axes (longitudinal slope ≈40°, transverse opening at the base ≈19.2 m). Legs are connected by a box-shaped transverse rod placed at about ⅓ H_{pier} from the hinges (4 × 3 m). Each leg features a rectangular hollow section (H = 3 ÷ 6 m increasing towards the deck, W = 2 m) being stiffened through flat ribs (p = 0.3 m) on all internal sides. 6 m-pitched Z-braces are present also in this case.

Both girder and piers were conceived as an assemblage of multiple, 6 m long segments due to shipment reasons. Structural continuity was hence restored on-site through double covered joints equipped with high-strength bolts. In a similar fashion, girder-to-legs connections were made through welded special segments at the piers' upper ends which were in turn bolted to the adjacent deck segments.

4.9.3 Geometric reconstruction of POC2 Cadore bridge

On the basis of data provided by the bridge manager and recollected from literature, a thorough geometric reconstruction of Cadore bridge was carried out. Namely, global dimensions, plates' thicknesses and configuration of stiffeners were derived for each deck and pier segment. As a consequence of structural optimization, 10 different cross-section configurations were adopted for the girder (see Figure 4.9-3a, blue markers), while 8 configurations were adopted for each pier (see Figure 4.9-3a, cyan markers). With reference to the specific purpose of the following developments (corrosion fatigue analysis and study of the effectiveness of low-impact retrofit strategies), reconstructed details were rationally simplified, i.e., in order to derive computationally addressable cross-section configurations for which mechanical properties could be easily estimated and used for global FEM modelling. An example of application of such logic is depicted in the following with reference to the middle girder segment (Cross-section A-A' – Figure 4.9-3b).

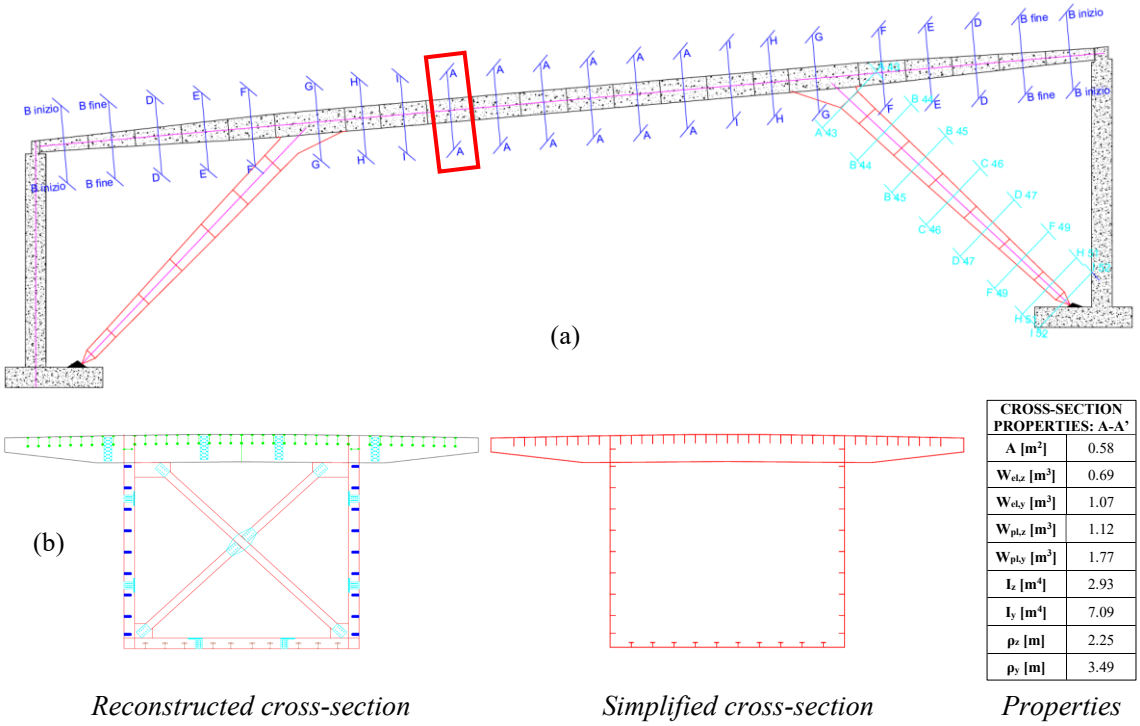

CROSS-SECTION PROPERTIES: A-A'	
A [m²]	0.58
$W_{el,z}$ [m³]	0.69
$W_{el,y}$ [m³]	1.07
$W_{pl,z}$ [m³]	1.12
$W_{pl,y}$ [m³]	1.77
I_z [m⁴]	2.93
I_y [m⁴]	7.09
ρ_z [m]	2.25
ρ_y [m]	3.49

Figure 4.9-3: a) Structural lateral view of the Cadore bridge with different cross-section configurations being highlighted in blue (girder) and cyan (piers), b) Example of cross-section reconstruction for Girder segment A-A'.

4.9.4 Global FE modelling of POC2 Cadore bridge

Global FE modelling of the Cadore bridge was carried out in SAP2000 environment (see Figure 4.9-4). Each girder and pier segment was modelled through a 1D frame element being aligned with the relevant cross-section centroid. In compliance with the intended response of structural details, no releases were placed in the connection zone among piers' legs and the girder (full-rigid joints). In the same fashion, base joints and deck ends' detailing were modelled through equivalent hinge or roller restraints.

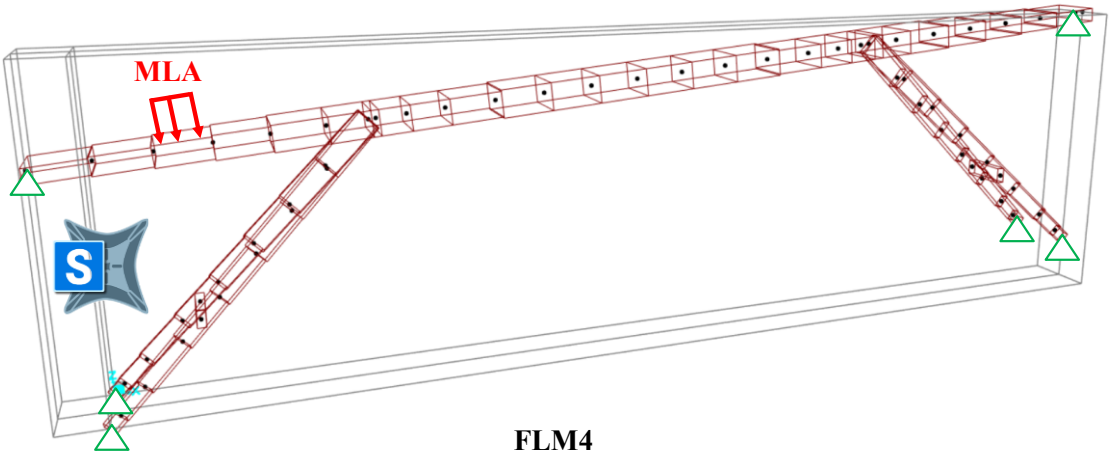

FLM4

Tab. 5.1.X – *Flusso annuo di veicoli pesanti sulla corsia di marcia lenta*

Categorie di traffico	Flusso annuo di veicoli di peso superiore a 100 kN sulla corsia di marcia lenta
1 - Strade ed autostrade con 2 o più corsie per senso di marcia, caratterizzate da intenso traffico pesante	$2{,}0 \times 10^6$
2 - Strade ed autostrade caratterizzate da traffico pesante di media intensità	$0{,}5 \times 10^6$
3 - Strade principali caratterizzate da traffico pesante di modesta intensità	$0{,}125 \times 10^6$
4 - Strade locali caratterizzate da traffico pesante di intensità molto ridotta	$0{,}05 \times 10^6$

Tab. 5.1.VIII - *Modello di carico di fatica 4 – veicoli equivalenti*

	Sagoma del veicolo	Tipo di pneumatico (Tab.5.1-IX)	Interassi [m]	Valori equivalenti dei carichi asse [kN]	Composizione del traffico: Lunga percorrenza	Media percorrenza	Traffico locale
V1	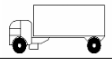	A B	4,50	70 130	20,0	40,0	80,0
V2	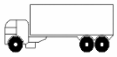	A B B	4,20 1,30	70 120 120	5,0	10,0	5,0
V3		A B C C C	3,20 5,20 1,30 1,30	70 150 90 90 90	50,0	30,0	5,0
V4	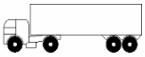	A B B B	3,40 6,00 1,80	70 140 90 90	15,0	15,0	5,0
V5		A B C C C	4,80 3,60 4,40 1,30	70 130 90 80 80	10,0	5,0	5,0

Figure 4.9-4: Global FE modelling of the Cadore bridge: structural scheme and assumed fatigue loads as per FLM4.

In order to perform MLAs, influence lines in performance-governing sections S (e.g., midspan segment, deck-to-pier connection, pier base joint, etc.) were derived. For this purpose, vertical unitary forces $F_Y = 1$ were considered as moving entities on a path coinciding with the roadway profile. Subsequently normal stress histories $\sigma(t)$ (oscillograms) were derived based on the combined effect of bending moments and axial forces. This enabled the derivation of equivalent stress ranges $\Delta\sigma_{eq}$ (fatigue demand) via the Rainflow method. In this regard, it is worth mentioning that a "medium distance" composition of traffic was assumed for FLM4-based calculations (see Figure 4.9-4). As for the total number of heavy trucks per year (average yearly traffic AYT), $n = 500000$ vehicles/year was assumed in compliance with NTC2018, Tab. 5.1.X, i.e., considering a moderate flow of heavy trucks due to the presence of a single slow lane per travel direction. An example of oscillograms (i.e., referred to deck section F-F') is shown in Figure 4.9-5.

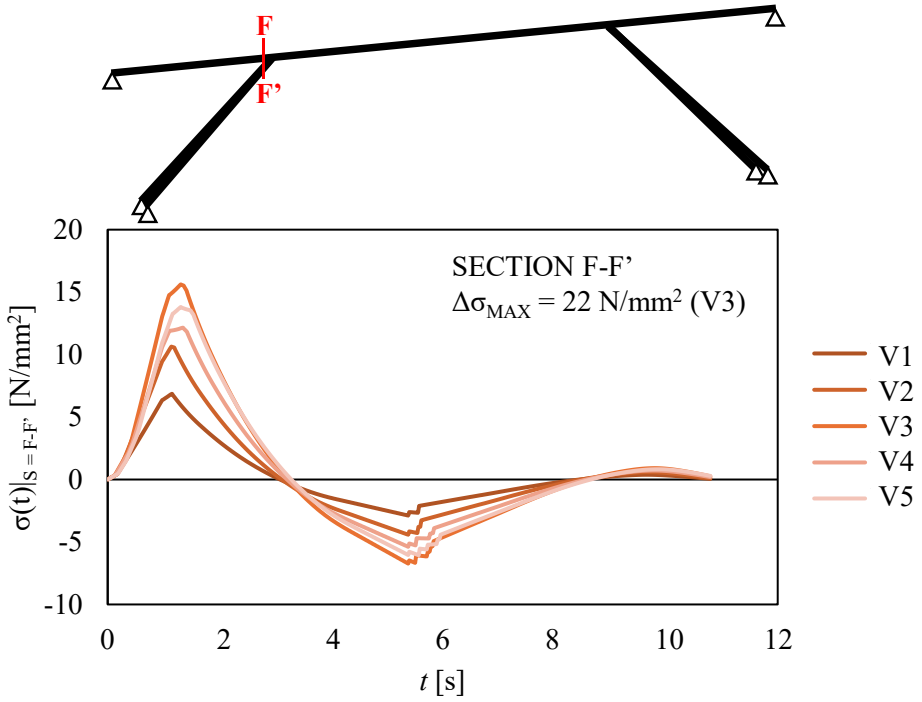

Figure 4.9-5: NTC2018-compliant stress oscillograms for deck section F-F'.

4.9.5 Considerations about spatial development of corrosion in Cadore bridge

As stated previously, all plates and members of the Cadore bridge viaduct are made of weathering steel. This choice, in principle, results in a superior corrosion performance of the structure due to the well-known process of formation of a protective (passivated) layer on exposed surfaces. Nevertheless, as reported in scientific literature, in presence of multiple factors such as *i*) persistent moisture, *ii*) reduced ventilation and *iii*) insufficient maintenance, even weathering steel components can deteriorate due to material loss. For the relevant case of Cadore bridge, these condition can potentially occur due to the peculiar configurations of cross-sections, i.e., closed boxes in which internal ventilation is limited and meteoric water can leak in from continuity joints and stagnate on the bottom. As a result, localized corrosive phenomena could potentially occur on deck lower flanges (see Figure 4.9-6).

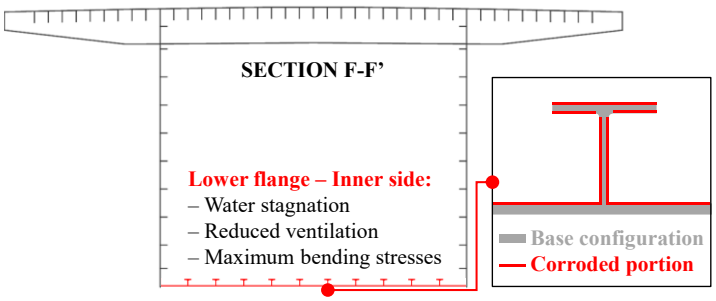

Figure 4.9-6: Assumed spatial development of corrosion for Cadore Bridge (Section F-F').

To this end, it is noteworthy reporting that even very large levels of local corrosion on the lower flange plate would still only result in very moderate "global" corrosion level. This condition justifies the assumption of neglecting any global stiffness reduction due to corrosive phenomena.

4.9.6 Local FE modelling of POC2 Cadore bridge

Local FE modelling of Cadore bridge was developed in ABAQUS 2017 environment (see Figure 4.9-7).

In order to balance computational effort and analyses accuracy, only a segment of the open-stiffened lower flange was modelled, i.e., the portion enclosed among two consecutive stiffeners (half IPE 240 segments) being welded to the 300 × 10 mm transverse plates. The peculiar 120 × 20 mm cutout below the IPE flange was also explicitly modelled to accurately detect stress concentrations, i.e., in compliance with recommendations from the European Technical Document CEN/TS 1993-1-901. In order to equivalently restore the structural continuity, the rear part of the transverse plate was assumed to be fixed ($U_{X,Y,Z} = R_{X,Y,Z} = 0$), while periodicity boundary conditions (BCs) were introduced on both sides ($U_Z = R_X = R_Y = 0$). Due to the small size of the considered detail with respect to global cross-section dimensions, uniform tension was assumed to act on the detail.

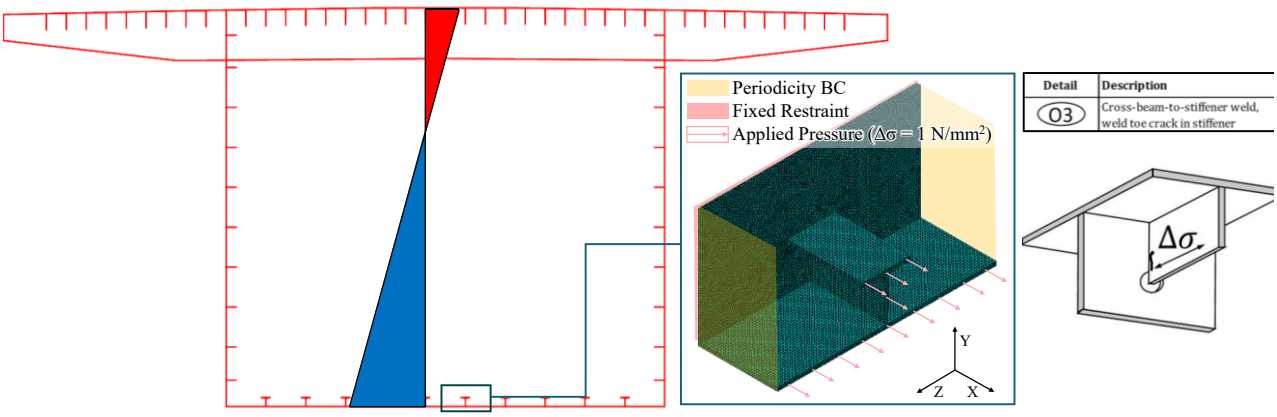

Figure 4.9-7: Local FE modelling of Cadore bridge for SED calculations.

Results of local FE analyses are depicted in Figure 4.9-8 for a pristine detail (Figure 4.9-8a) and a worn detail (Figure 4.9-8b). As expected, most severe stress concentration always occur nearby the flange-to-cutout weld toe, around which the SED-related control volume (R_0 = 0.28 mm) was hence identified. Notably, a local reduction of the lower flange cross-section of 10% results in a +10%, +4% and +22% increase of maximum principal stress, peak strain energy density and averaged strain energy density, respectively.

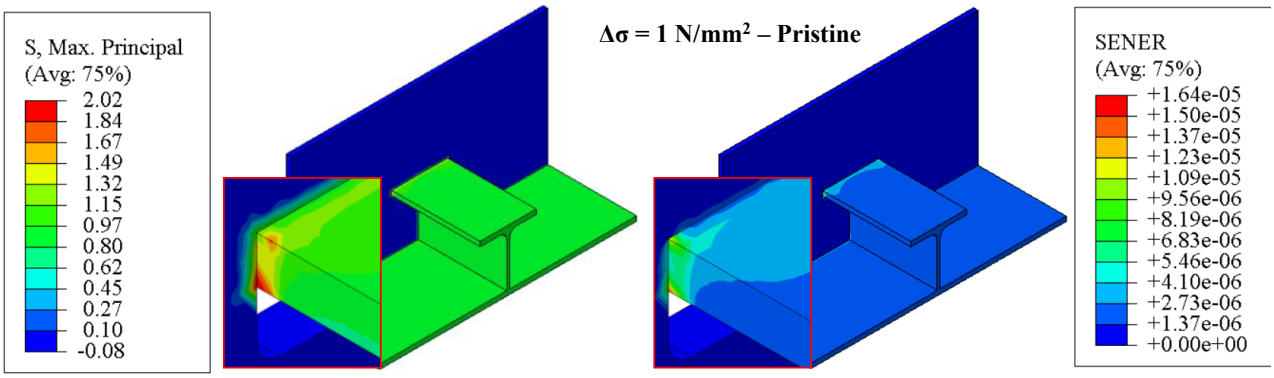

a)

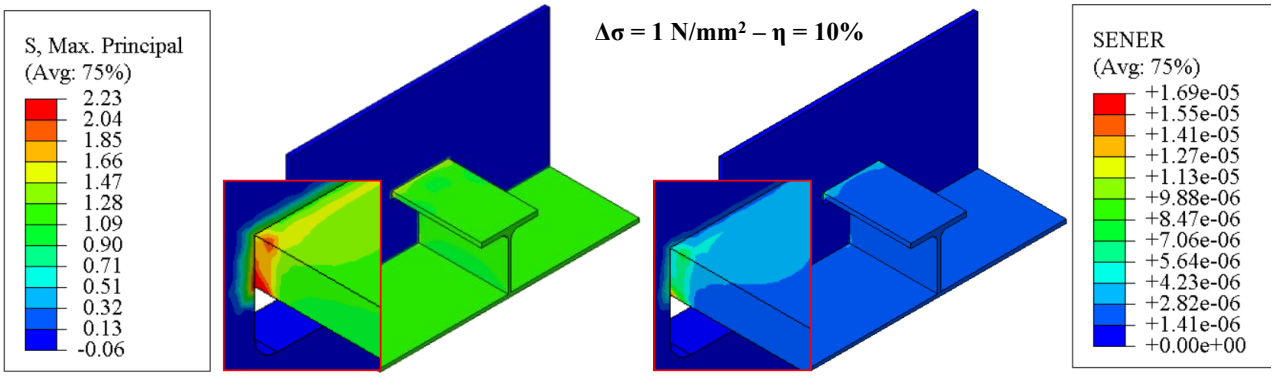

b)

Figure 4.9-8: Results of local FE analyses: distribution of maximum principal stresses and strain energy density for a) pristine detail (η = 0%), b) worn detail (η = 10%).

4.9.7 Fragility estimation of Cadore bridge

On the basis of the above MS-FE analyses, fragility estimation as per §4.8.1 and §4.8.2 has been carried out.

For instance, n_{TOT} = 200 scenarios were considered, i.e., assuming a variation of n in the range [1/6; 6] as suggested in *Guo et al., 2019*. With reference to IM values, η_{MAX} in the range [0%; 50%] was investigated, i.e., with the relevant mass loss being referred to the lone lower flange cross-section.

Relevant results are depicted in Figure 4.9-9 in terms of *a*) trend of key analysis parameters (i.e., n_{fail} for the frequentist approach and $D_{avg,ln}$; $\sigma_{D,ln}$ for the distribution-based approach) and *b*) resulting fragility curves.

It can be easily observed how the frequentist approach yields a sharp increase of n_{fail} for η_{MAX} > 25%, with an increase rate of about ≈17 failure cases per 1% increment of corrosion degree until η_{MAX} = 30%. Subsequently, a stabilization is observed in the range η_{MAX} = 30-40% before n_{fail} becomes equal to n_{TOT} for η_{MAX} = 47%.

In a similar fashion, the distribution-based approach depicts a clear linear trend of $D_{avg,ln}$ for increasing values of η_{MAX}. Most notably, the average value of ln D approaches 0 (→ D = 1 → failure threshold) for similar values of η_{MAX} (≈32%) with respect to the frequentist approach. Moreover, a clear heteroskedasticity of results is observed, i.e., with results being far more scattered as the maximum corrosion degree increases ($\sigma_{D,ln,10\%}$ = 0.33, $\sigma_{D,ln,20\%}$ = 0.59, $\sigma_{D,ln,30\%}$ = 0.76).

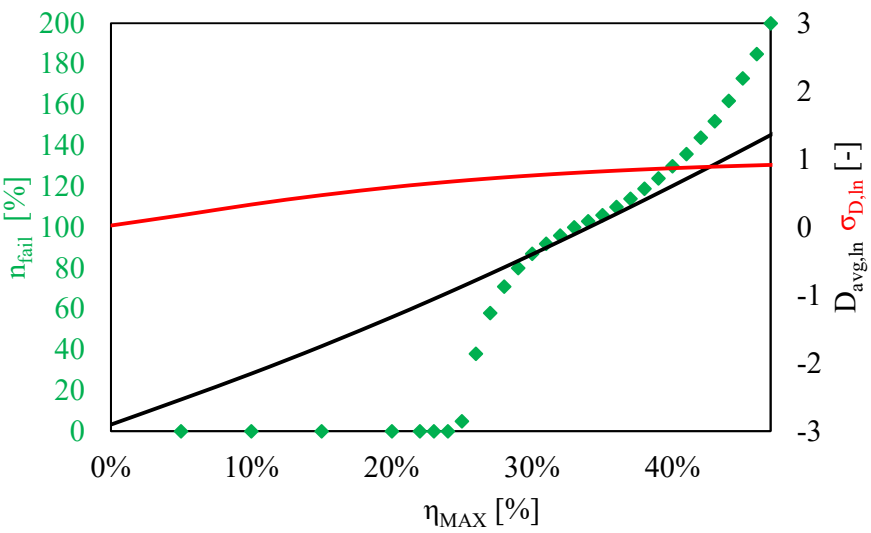

a)

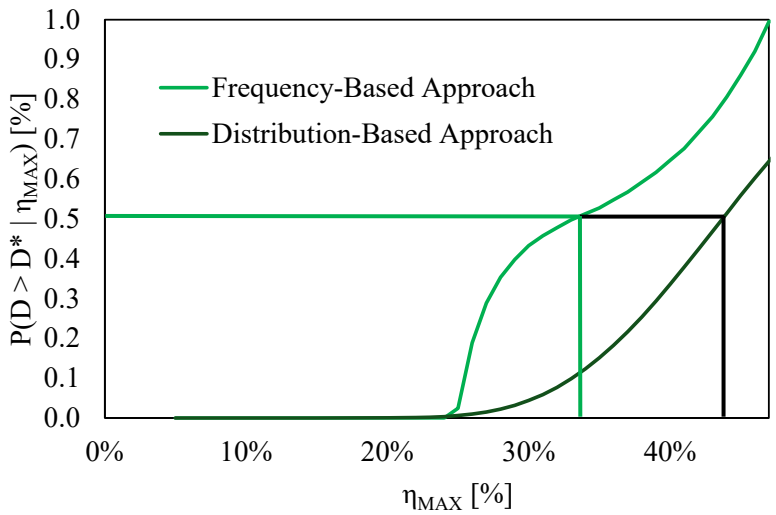

b)

Figure 4.9-9: Fragility assessment of Cadore Bridge: a) relevant parameters for the frequentist and distribution-based approach and b) resulting fragility curves.

Consistently, corrosion fatigue fragility curves are almost null for $\eta_{MAX} < 25\%$, and hence they sharply increase. Significantly, the frequentist approach proves to be more severe, i.e., with a median value of η_{MAX} (i.e., associated with $P_F = 0.5$) of $\approx 33\%$, while $\eta_{MAX,MEDIAN} \approx 43\%$ is achieved according to the distribution-based approach.

4.10 Conclusions

In this Section, the proposed methodology for MS-FEM of steel/composite bridges affected by fatigue and degradation phenomena has been used to estimate structural fragility.

To this regard, two different approaches, i.e., a frequency-based and distribution-based one, have been proposed and applied with reference to a representative case study, i.e., the Cadore Bridge belonging to the POC2 SS51 Alemagna developed within the EP RETURN Project.

Accordingly, thorough geometric reconstruction of the bridge was first carried out based on information provided by the bridge manager and found in literature. Subsequently, global FEM was developed in SAP2000 environment, i.e., using 1D frame elements accounting for the variation of cross-section properties along critical cross-section of the bridges. Subsequently, refined local FEMs were developed in ABAQUS 2017 environment to evaluate the energy-based fatigue demand on critical welded details.

MS-FEM of Cadore bridge enabled the estimation of the damage matrix, and relevant fragility curves were hence derived. Remarkably, similar median values of "critical" corrosion (i.e., in the range 30-40% in terms of mass loss of the lower flange) were derived in both cases, i.e., providing a first significant application of proposed methodologies.

4.11 References

Basava S, Hess DP. Bolted Joint Clamping Force Variation Due To Axial Vibration. Journal of Sound and Vibration (1998), 210(2), 255-265.

Berto F, Lazzarin P. Recent developments in brittle and quasi-brittle failure assessment of engineering materials by means of local approaches. Materials Science and Engineering: R: Reports (2014), 75, 1-48.

Contreras G, Goidanich S, Maggi S, Piccardi C, Diamanti MV, Pedeferri MP, Lazzari L. Representing localized corrosion processes through cellular automata. Corrosion Reviews (2011), 29, 241-245.

Dutta A, Dhar S, Acharyya S. Material characterization of SS 316 in low-cycle fatigue loading. Journal of Materials Science (2010), 45(7), 1782-1789.

European Committee for Standardisation (CEN). EN1990: Basis of Structural Design.

European Committee for Standardisation (CEN). EN1991-2: Actions on Structures –Traffic Loads on Bridges.

European Committee for Standardisation (CEN). EN1993-1-8: Design of Steel Structures – Design of Joints.

European Committee for Standardisation (CEN). EN1993-1-9: Design of Steel Structures – Fatigue.

Foti P, Berto F. Strain Energy Density evaluation with free coarse mesh model. Material Design & Processing Communications (2020), 2(5), 1-4.

Italian Ministry for Public Works (Min. LL. PP.). Circolare n. 384, 14/02/1962 – Norme relative ai carichi per il calcolo dei ponti stradali [In Italian].

Lazzarin P, Zambardi R. A finite-volume-energy based approach to predict the static and fatigue behavior of components with sharp V-shaped notches. International Journal of Fracture (2001), 112, 275-298.

Lazzarin P, Berto F, Zappalorto M. Rapid calculations of notch stress intensity factors based on averaged strain energy density from coarse meshes: Theoretical bases and applications. International Journal of Fatigue (2010), 32, 1559-1567.

Li ZX, Sun ZH, Guo L, Chan T, Yu Y. Concurrent multi-scale modeling of structures and damage analyses. Journal of Southeast University (2007), 37(2), 251-260.

Liu C, Kelly RG. A Review of the Application of Finite Element Method (FEM) to Localized Corrosion Modeling. Corrosion (2019), 75(11), 1285-1299.

Mashayekhi M, Santini-Bell E. Fatigue assessment of a complex welded steel bridge connection utilizing a three-dimensional multi-scale finite element model and hotspot stress method. Engineering Structures (2020), 214, 110624.

Milone A, Landolfo R. Advanced Cyclic Assessment of an Existing Steel-Concrete Composite Road Bridge. Proceedings of the 11th International Conference on the Behaviour of Steel Structures in Seismic Areas (STESSA 2024).

Milone A, Tartaglia R, D'Aniello M, Landolfo R. Seismic upgrade of a non-code compliant multi-storey steel building: A case study. Journal of Building Engineering (2024), 95, 110151.

Radaj D, Vormwald M. Advanced Methods of Fatigue Assessment, Springer-Verlag, Berlin (2013).

Razavi SMJ, Peron M, Torgesen J, Berto F, Mutignani F. Effect of hot dip galvanization on the fatigue strength of steel bolted connections. Frattura ed Integrità Strutturale (2017), 41, 432-439.

Tartaglia R, Milone A, D'Aniello M, Landolfo R. Retrofit of non-code conforming moment resisting beam-to-column joints: A case study. Journal of Constructional Steel Research (2022), 189, 107095.

Wang /, Li Z, Wang C, Wang H. Concurrent multi-scale modelling and updating of long-span bridges using a multi-objective optimisation technique. Structure and Infrastructure Engineering: Maintenance, Management, Life-Cycle Design and Performance (2013), 9(12), 1251-1266.

Zhu Q, Xu YL, Xiao X. Multiscale Modelling and Model Updating of a Cable-Stayed Bridge. I: Modeling and Influence Line Analysis. Journal of Bridge Engineering ASCE (2015), 20(10), 04014112.

5. Physics-based models, surrogate models and experimental assessment of the vehicle-bridge interaction in braking conditions

5.1 Introduction

Braking is a common excitation source for roadway bridges. Previous studies have shown that it can be a dynamic loading scenario more severe than the one originated by a vehicle moving at constant speed. The effects of braking on bridge dynamics can be conveniently measured using the so-called impact factor, which expresses the ratio between the maximum bridge response (e.g., displacement) under braking conditions and the value corresponding to a vehicle that moves with constant speed. Dynamic effects due to braking often lead to impact factors larger than one, which can also exceed those prescribed in bridge design codes. This is especially evident if the vehicle brakes almost instantaneously in the first half-span of the bridge. Compared to a vehicle moving at constant velocity, it has been found that braking can amplify the bridge response by 30% and more. The effects attributable to braking can be further amplified in curved bridges.

The comprehensive numerical simulation of vehicle dynamics under braking would require a multiphysics approach. In this sense, Guner et al. (2004) carried out a thermodynamic analysis of the braking effect while Broniszewski et al. (2019) estimated the influence of the vehicle aerodynamics on the braking length. Although these studies provide relevant information about vehicle dynamics under variable speed, their computational effort is too prohibitive for bridge assessment applications. For the sake of simplicity, therefore, most of the available studies implement somewhat similar and less sophisticated dynamic models. In doing so, a hard braking condition is typically assumed and the inherent nonstationary random process attributable to the road roughness is not considered. This modelling approach is meant at maximizing the dynamic response of the bridge under traffic load. Nonetheless, neither stationary road roughness nor a hard braking condition can often simulate the actual bridge dynamics. Hence, it is evident that a quantitative comparison among modelling strategies with different levels of sophistication is needed for the proper assessment of all the phenomena and variables involved in the vehicle-bridge dynamic interaction under braking conditions. This is the essential premise for using any model with the right confidence level in bridge assessment. Vehicle-bridge dynamic modelling is also relevant for the studies that investigate the feasibility of drive-by identification techniques (Cheema et al. 2022, Mokalled et al. 2022) as well as the structural health monitoring of bridges based on the response of the vehicles (Li et al. 2022) or using traffic-induced energy harvesting devices (Cahill et al. 2016).

Indeed, the realistic simulation of the bridge dynamics under the passage of vehicles calls for the proper consideration of the road roughness (Yang and Sun 2020). In this regard, most of the previous studies do not account for the nonstationary random excitation that arises when the bridge is crossed by vehicles moving at variable speed (Chompooming and Yener 1995), or the nonstationary random response of the system is approximated assuming a stationary stochastic process in the time domain (Ju and Lin 2007). Nonetheless, road roughness can generally be simulated as a stationary random process in the space domain provided that the vehicle moves with a constant speed only. In such cases, the tire response induced by road roughness is a stationary random process in the time domain. Conversely, when a vehicle moves at variable speed, the tire response induced by the road roughness is essentially a nonstationary random process in the time domain (Zhang et al. 2002). A few approaches have been developed so far to analyze nonstationary random vibrations due to a vehicle subjected to acceleration or braking. A state-space formulation has been originally proposed for simulating the nonstationary response of a vehicle that travels on a homogeneous rough road. Herein, vehicle dynamics is modelled via linear ordinary differential equations in the time domain. In contrast, a differential equation models the excitation process of rough roads in the spatial domain. Furthermore, Sasidhar

and Talukdar (2003) use Monte Carlo simulations to reproduce the actual rough deck profile. For the sake of completeness, it is highlighted that most studies assume perfect contact between the wheel and the road surface, but there are a few recent attempts that also account for the wheel separation (Zhang et al. 2018). Azimi et al. (2013) and Yu et al. (2018) showed that road roughness can have a significant effect on the vertical responses of the bridge, but it has limited influence on the longitudinal reaction forces at the hinged supports. The negligible effect of braking on longitudinal acceleration is also confirmed in other studies (Gao et al. 2022).

Vehicle modelling also plays an important role when studying the effects of braking on bridge dynamics. A large variety of vehicle models has been proposed so far, spanning from quarter-vehicle models to two-dimensional and three-dimensional models. Regarding the analysis of the bridge response under moving vehicles, there are two main strategies. The simplest approach assumes that vehicle dynamics do not affect the bridge response. Such an approach is widely used in engineering practice due to its easy implementation, reduced computational cost (Zhu and Law 2015), and robustness against numerical instability (Deng et al. 2015). Hence, the vehicle-bridge system is divided into two subsystems, so as the corresponding dynamic equations are solved separately using an iterative procedure. However, the assumption of uncoupled vehicle-bridge dynamics cannot always be accepted. Therefore, more refined strategies to solve the coupled dynamical system have been also proposed. For example, Henchi et al. (1998) solve the coupled equations of motion by means of the central difference method while Yang and Lin (1995) develop a vehicle-bridge interaction element. Finally, it is important to recall that, since the response of the vehicle tires is a random process, the effects of braking conditions should be investigated on a statistical basis. Despite this evidence, only deterministic analyses are reported within the current literature.

Regardless of their fidelity level, all existing models about the vehicle-bridge dynamic interaction in braking conditions are derived on a physical basis and call for the solution of some differential equations. Regrettably, the associated computational effort is an issue for several practical applications where the governing equations must be solved several times (e.g., scenario and vulnerability analysis). This issue has recently motivated the exploitation of data-driven approaches for developing efficient, yet accurate, surrogate models. For instance, Ni et al. (2021) develop a Kriging surrogate model for the reliability-based design of bridges taking into account the vehicle-bridge interaction. Such a study has the merit of being the only one that explores the use of surrogate models for addressing vehicle-bridge interaction problems, but it neglects the braking effects.

Within this framework, the present work aims at providing new insights into the dynamic vehicle-bridge interaction in braking conditions. In this perspective, an extensive numerical investigation is first performed by means of both physics-based models and surrogate models. On the one hand, the critical examination of the obtained results reveals some effects of the vehicle-bridge interaction in the braking conditions that were not pointed out previously. On the other hand, it is demonstrated for the first time that surrogate models are able to capture the complex dynamics of the vehicle-bridge interaction in braking conditions. The present study concludes with an experimental investigation that aims at evaluating the accuracy of the considered numerical (physics-based and surrogate) models.

5.2 Numerical modeling

5.2.1 Dynamic analysis of the vehicle-bridge interaction in braking conditions

Braking often constitutes a more critical scenario for bridge dynamics as compared to a vehicle moving at a constant speed. The peculiar dynamics induced by braking depend on the concurrent effects of three relevant factors.

- *Road roughness*. If a vehicle moves at a variable speed, then the roughness level of the road is also variable and depends on the vehicle's speed impacting the road asperities. Therefore, road roughness cannot be accurately represented in such cases through a stationary random process. Conversely, it acts as a nonstationary random process for vehicle dynamics. While a nonstationary random process can simulate the reduction of the frequency content in the excitation due to the lowering of vehicle speed, a stationary random process always reflects a constant velocity condition, even if the vehicle is braking.
- *Inertial effects*. When the vehicle moves at a constant speed, the bouncing and pitching of the vehicle are uncoupled. In the case of braking, a horizontal inertial force applied to the vehicle's centroid couples bouncing and pitching. This contributes to amplifying the excitation level and thus can increase the dynamic response of the bridge.
- Braking friction. Braking cannot be realistically considered an instantaneous phenomenon. This implies that a finite, non-zero braking length is always needed in order to reduce the speed of the vehicle until it stops. This phenomenon is governed by dynamic friction forces that originate between the tires and the road. These horizontal forces represent an eccentric axial load for the bridge and can amplify its dynamic response.

The displacement impact factor IF is commonly considered in order to quantify the effects of braking on bridge dynamics under traffic loads. It is defined as follows:

$$\mathrm{IF}=\frac{w_{b,braking}}{w_{b,constant}}, \tag{5.2-1}$$

where $w_{b,braking}$ and $w_{b,constant}$ are the maximum bridge deflection under braking conditions and the value corresponding to a vehicle that moves at a constant speed, respectively. Although the realistic analysis of the vehicle–bridge dynamic interaction should account for all these factors, several studies are based on similar models that take into account a limited set of them. The lack of comparative studies among different modelling approaches, in turn, does not allow us to understand the effects of all the assumptions and parameters involved. The critical examination of alternative modelling approaches accounting for their complexity and accuracy, as well as the associated computational cost, are also crucial towards practical applications, such as sensitivity and reliability analyses. Hence, two classes of modelling approaches are herein considered to investigate the dynamics of the vehicle–bridge interaction in braking conditions. The first class of approaches encompasses physics-based models (i.e., models ruled by dynamic laws). Specifically, six models characterized by different levels of complexity and accuracy are considered. They are listed in Table 5.2-1 together with the corresponding assumptions.

Table 5.2-1 – Physics-based models of the vehicle-bridge interaction in braking conditions.

Model label	IF label	Model assumptions			
		Roughness	Vehicle model	Inertial effects	Braking friction
1dof-hb-st	$\mathrm{IF}_{1,hb,st}$	Stationary	1-degree-of-freedom	No	No
1dof-hb-st	$\mathrm{IF}_{1,bl,st}$	Stationary	1-degree-of-freedom	No	Yes
1dof-sb-nst	$\mathrm{IF}_{1,bl,nst}$	Nonstationary	1-degree-of-freedom	No	Yes
2dof-hb-st	$\mathrm{IF}_{2,hb,st}$	Stationary	2-degree-of-freedom	Yes	No
2dof-sb-st	$\mathrm{IF}_{2,nl,st}$	Stationary	2-degree-of-freedom	Yes	Yes
2dof-sb-nst	$\mathrm{IF}_{2,bl,nst}$	Nonstationary	2-degree-of-freedom	Yes	Yes

The synoptic scheme in Figure 5.2-1 resumes the assumptions underlying the estimation of the IF according to the considered physics-based models.

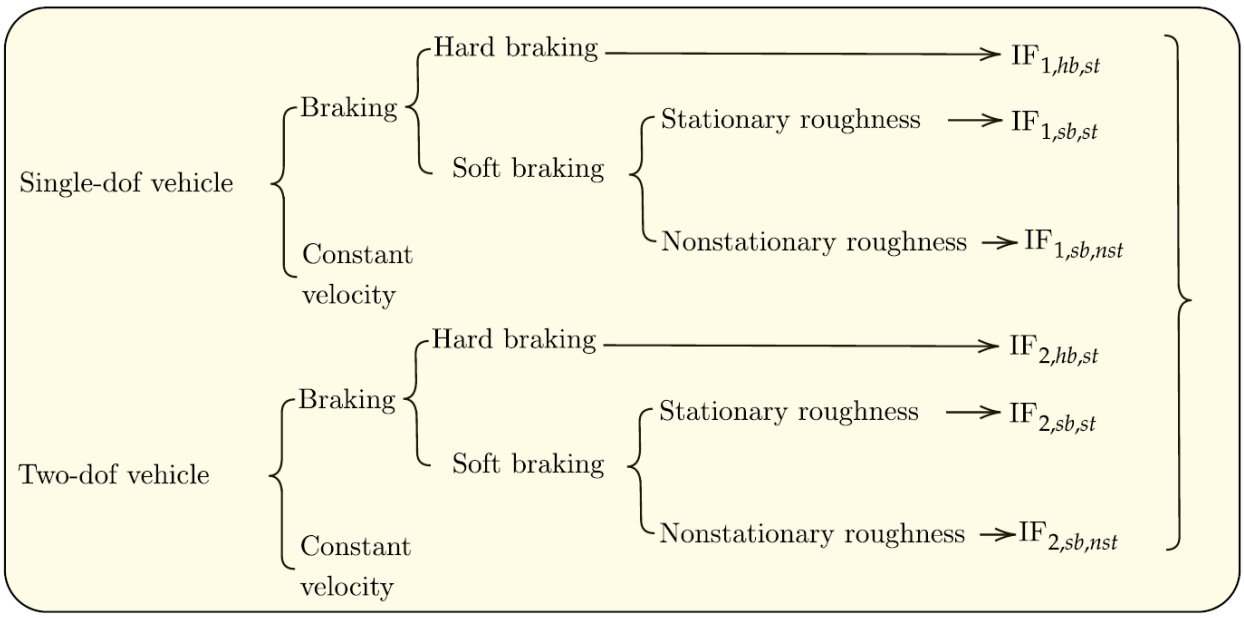

Figure 5.2-1 – Synoptic scheme that resumes the assumptions underlying the estimation of the IF according to the considered physics-based models.

Since these physics-based models are ruled by differential equations, their use can require a tremendous computational effort if they must be solved many times. Surrogate models (also known as metamodels) can provide a convenient way to cope with the computational burden required by these applications. In this context, the basic idea is to develop a data-driven approximation of the vehicle-bridge interaction in breaking conditions that is more efficient to execute, in such a way to obtain a direct estimate of the desired output starting from a set of relevant parameters. The development of surrogate models requires discovering the correct function that fits the data and the appropriate numeric coefficients of the function. Machine learning techniques have proven especially suitable to deal with this task in several scientific fields. Therefore, their feasibility in approximating the dynamics of the vehicle–bridge interaction under braking conditions is investigated here. Specifically, the following two supervised machine learning techniques are considered (Quaranta et al. 2020).

- *Neural network*. The elaboration of the data-driven model for the vehicle–bridge dynamic interaction leverages the well-known capability of neural networks as universal function approximators.
- *Genetic programming*. Evolutionary computing is exploited to look for a proper model function in symbolic form, which approximates as best as possible the desired output.

Neural networks usually provide data-driven models that are more accurate than those carried out using genetic programming. However, depending on the neural network's complexity, it may be hard to write down the corresponding final model function as a compact symbolic expression. Genetic programming sometimes leads to less accurate predictions than neural networks, but it provides a symbolic function that can be conveniently employed in practice.

5.2.2 Physics-based vehicle-bridge dynamic modelling

Figure 5.2-2 and Figure 5.2-3 shows a vehicle represented as one-degree-of-freedom and two-degrees-of-freedom oscillator, respectively, moving on a bridge (represented as a pinned-pinned beam).

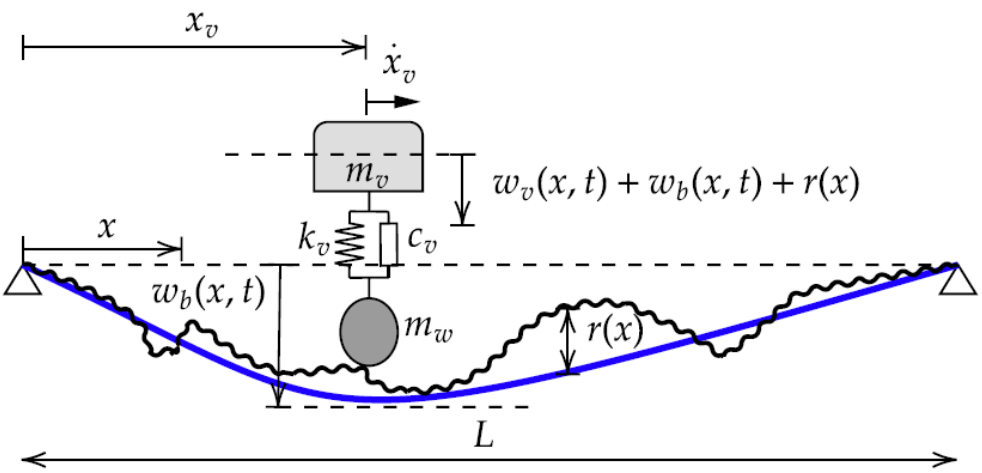

Figure 5.2-2 – Single degrees-of-freedom vehicle model moving on a pinned-pinned beam-type bridge model.

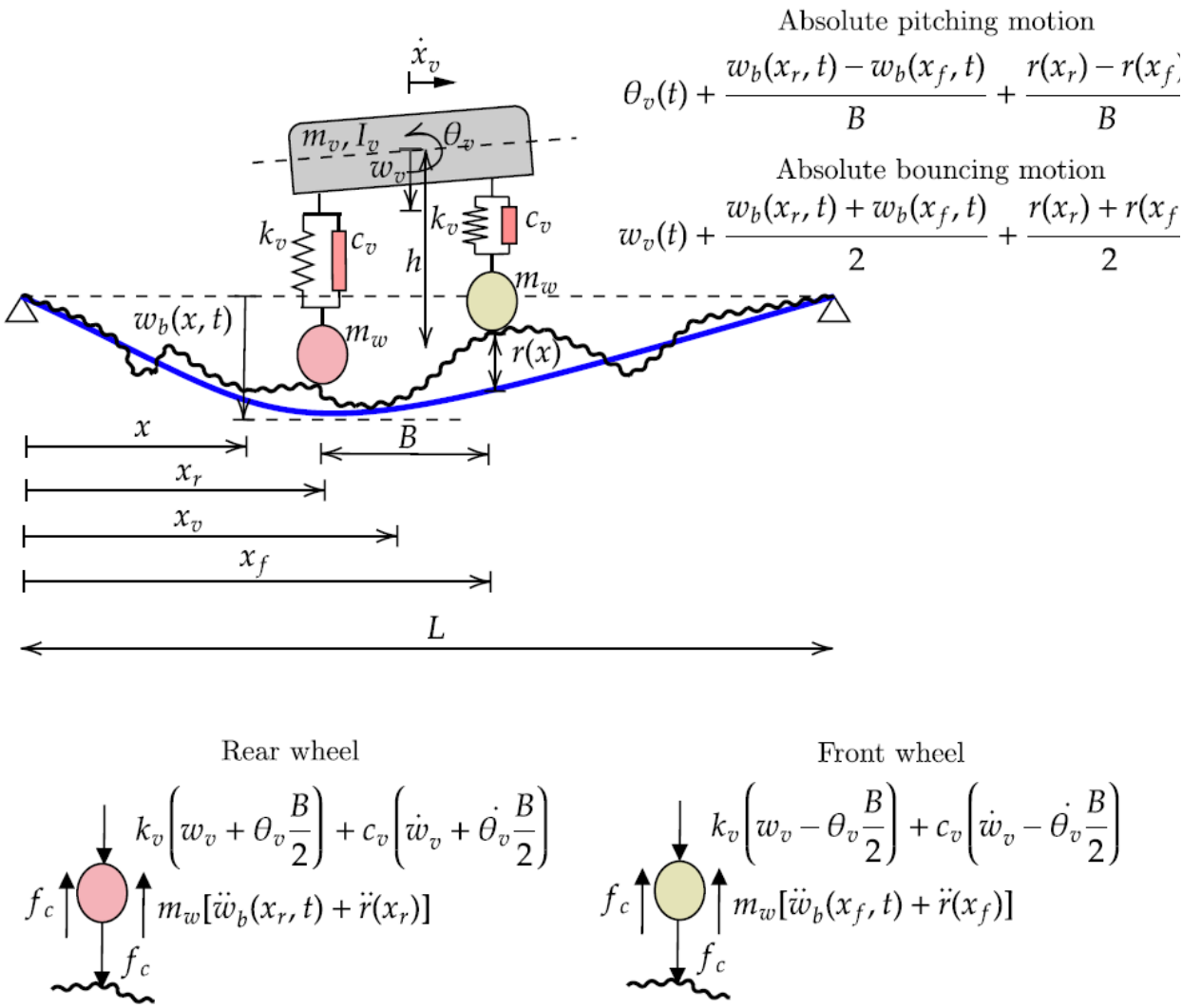

Figure 5.2-3 – Two degrees-of-freedom vehicle model moving on a pinned-pinned beam-type bridge model.

Taking the two-degrees-of-freedom vehicle mode as reference, translation and rotational dynamic equilibrium equations of the vehicle mass can be written as follows:

$$m_v\left[\ddot{w}_v+\left(\frac{\ddot{r}(x_r)+\ddot{r}(x_f)}{2}\right)+\left(\frac{\ddot{w}_b(x_r,t)+\ddot{w}_b(x_f,t)}{2}\right)\right]+2c_v\dot{w}_v+2k_vw_v=0, \tag{5.2-2}$$

$$I_v\left[\ddot{\theta}_v+\left(\frac{\ddot{r}(x_r)-\ddot{r}(x_f)}{B}\right)+\left(\frac{\ddot{w}_b(x_r,t)-\ddot{w}_b(x_f,t)}{B}\right)\right]+m_vh\ddot{x}_v+\frac{B^2}{2}c_v\dot{\theta}_v+\frac{B^2}{2}k_v\theta_v=0. \tag{5.2-3}$$

The bridge is modelled as a linear elastic Euler–Bernoulli beam with constant mass per unit length and constant bending stiffness. The continuous vertical displacement of the bridge is governed by the following partial differential equation:

$$\rho A\ddot{w}_b(x,t)+EJw_{r,xxxx}(x,t)=\delta_r(x_r-\dot{x}_vt)\left(f_{c,r}+m_wg+\frac{1}{2}m_vg\right)+ \\ \delta_f(x_f-\dot{x}_vt)\left(f_{c,f}+m_wg+\frac{1}{2}m_vg\right)+\frac{\partial m(x)}{\partial x}. \tag{5.2-4}$$

All the equations ruling the vehicle–bridge interaction can be written in matrix form by discretizing the beam span into n degrees-of-freedom and N elements whose length is Δx. The spatial discretization is performed using the finite difference method. For more details, the interested reader is referred to the work by Aloisio et al. (2023).

5.2.3 Machine-learning-aided surrogate vehicle-bridge dynamic modelling

The development of surrogate models for predicting the bridge response via neural networks and genetic programming is now addressed. It is understood that both these machine learning techniques must undergo a proper training stage, which also defines the application of the corresponding surrogate models against new data. The training dataset can be obtained using any one of the considered physics-based models. The accuracy of the predictive capability of the resulting surrogate models is then corroborated by considering a validation dataset (i.e., new data that was not included in the training dataset). A multi-layer feedforward artificial neural network is herein investigated. Optimizing the artificial neural network layout is critical in maximizing its accuracy level and its predictive capability against new data. Among the different strategies proposed to optimize the artificial neural network layout, a genetic-algorithm-based approach has been adopted in the present work. The general procedure is outlined in Figure 5.2-4. The genetic algorithm is designed to optimize the number of hidden layers, the number of artificial neurons for each hidden layer and their activation function (the same activation function is assumed for all hidden artificial neurons). The activation function for the artificial neurons in the output layer and the training solver is assigned a priori. The chromosome encoding of the candidate solution consists of two parts. The length of the first part is equal to the assigned maximum number of hidden layers. Herein, an integer variable identifies the number of hidden layers and hidden artificial neurons: the number of non-zero elements in this chromosome segment defines the number of hidden layers, whereas the corresponding values identify the number of hidden artificial neurons for each layer. The last element of the chromosome encodes the activation function for the hidden artificial neurons using another integer number. An artificial neural network is thus built for each chromosome, which is next trained by the selected training solver. The genetic algorithm optimizes the layout of the net in an attempt to maximize its accuracy, which is quantified by evaluating the root mean squared error function against the training dataset.

The search for the symbolic form of the best model function via genetic programming is performed by adopting a tree-based representation of the candidate solutions. The initial population is obtained according to the ramped half-and-half method. This initial population is then manipulated iteratively by applying standard genetic operators. The following combination of genetic operators is implemented throughout the iterative procedure, namely tournament selection, subtree crossover, point mutation, and reproduction. Common arithmetic, logarithmic, exponential and power operators are selected as candidates for the model formulation. One of the most critical issues in implementing genetic programming algorithms is the uncontrolled growth of the model complexity. This phenomenon is also known as bloat and identifies an excessive growth of the model complexity that leads to a small increment of the model accuracy over the training dataset. In contrast,

it often goes with a significant worsening of the predictive capability against new data. Out of the available approaches to cope with bloat in genetic programming, the strategy implemented in the present work assumes model accuracy and model complexity as conflicting criteria following Ekart and Nemeth (2001).

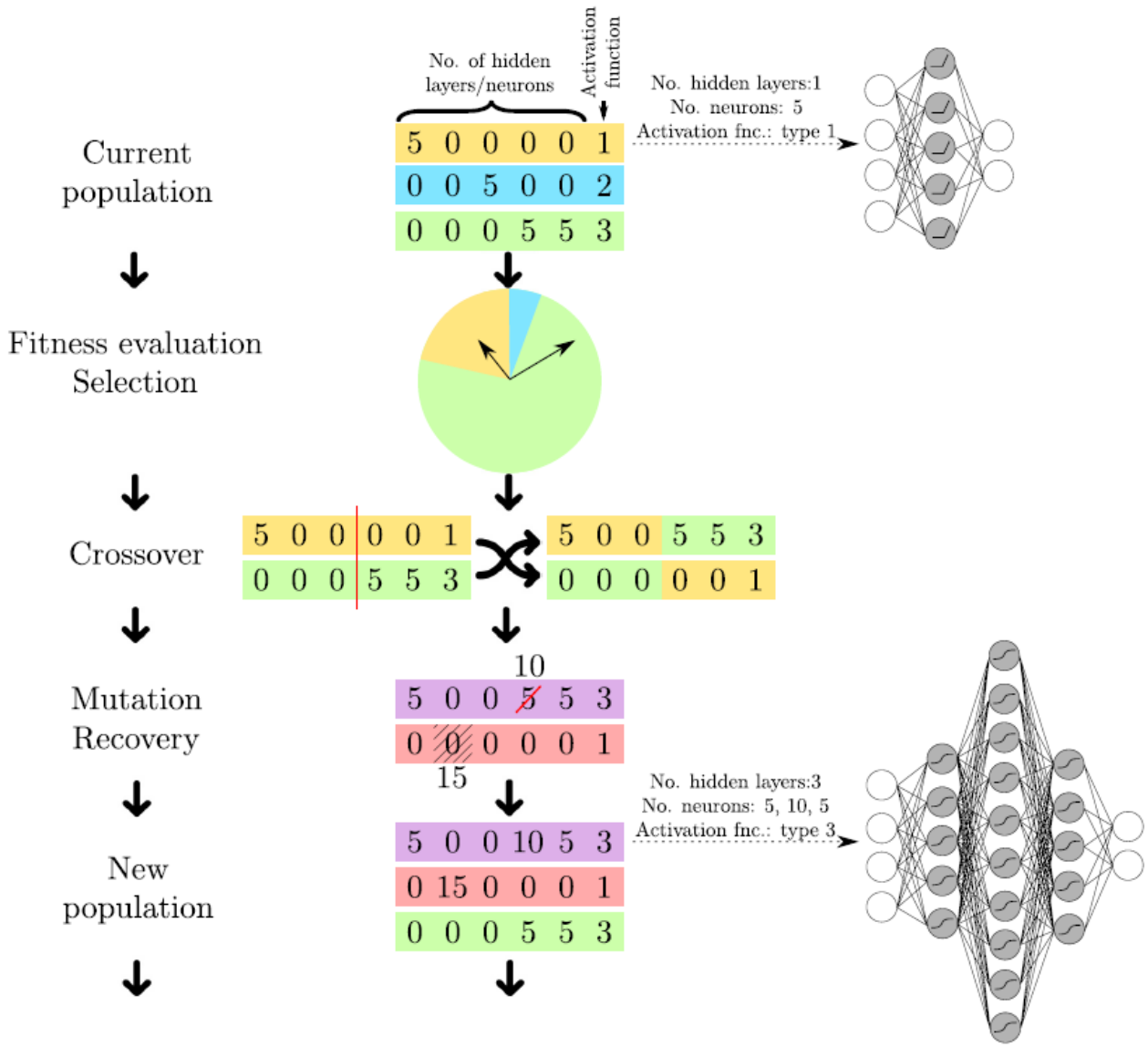

Figure 5.2-4 – Genetic-algorithm-based optimization of the artificial neural network architecture.

5.3 Numerical and experimental applications

An existing bridge is considered as case study for the following numerical and experimental investigations. It is a simply supported pre-stressed concrete girder bridge belonging to the Italian motorway network. The cross-section has a trapezoidal shape and is 2.3 m high, with two cantilevered wings 3.85 m wide, which are pre-stressed by bonded post-tensioned tendons. A pair of piers, whose center distance is about 40 m, sustains each bridge span. This bridge has been selected as a case study since it can be considered representative of medium-span prestressed concrete girders of the Italian motorway network.

Numerical investigations have been performed by varying randomly the road roughness in each simulation. Three roughness classes are considered according to ISO 8608 specifications. Attention is paid on road and vehicle parameters that might influence the vehicle-bridge dynamic interaction in braking conditions according

to the current state-of-the-art. The parameters selected for the following numerical investigations together with their ranges of variation reflect the usual variability of road and vehicle characteristics. Particularly, viscous damping coefficient of the vehicle and friction coefficient values are based on existing literature.

Experimental tests have also been performed to corroborate the accuracy of the numerical predictions. The dynamic bridge deflection of the bridge under the applied dynamic load has been measured using a laser sensor. The portable equipment installed for the dynamic measurement of the bridge displacements is shown in Figure 5.3-1. It consists of an easel supporting a laser sensor (Microepsilon optoNCDT 1420). The sampling rate was 1000 Hz. The C-Box/2 A controller (Micro-epsilon) digitizes the signal, which is then acquired through a personal computer using an Ethernet cable. A lead–acid battery provides power to the laser sensor, the controller and the personal computer.

(a) (b)

Figure 5.3-1 – Some views of the bridge under investigation from the road level (a) and from beneath the deck (b), where it is also possible to note the equipment that was installed to measure the deflection under the applied dynamic load..

5.3.1 Monte Carlo simulations

Monte Carlo simulations are conducted to evaluate the statistics of the IF calculated according to the considered physics-based models. These simulations are accomplished by sampling the numerical values of vehicle and road parameters through the Latin hypercube technique. lists the statistics of the IF estimates obtained using the considered models. On the one hand, this statistical analysis confirms some well-established results.

- Hard braking is the most severe dynamic loading scenario for the bridge on average since the corresponding mean values of the IF are larger than one. For such braking conditions, the use of a two degrees-of-freedom vehicle model leads to mean IF values slightly larger than those obtained by means of a single degree-of-freedom vehicle model because the latter does not account for the inertial effects due to pitching.
- If the friction forces manifesting in the braking length are considered, then a nonstationary road roughness model leads to mean IF values slightly larger than those obtained under the assumption of a stationary road roughness model. This result does not depend on the vehicle model and is attributable to the fact that a nonstationary roughness model yields effects at frequencies closer to those of the bridge.

On the other hand, this statistical analysis also highlights some effects of the dynamic modelling of the vehicle-bridge interaction that are not pointed out in the existing studies.

- The vehicle model has a different influence depending on which braking scenario is considered. In the case of soft braking, a single-degree-of-freedom vehicle model yields mean IF values much larger than those estimated using a two-degrees-of-freedom model, given the road roughness. This heavily contrasts with what has been just observed in case of hard braking and may appear counter-intuitive. Ultimately, it implies that pitching motion can be negligible in the case of soft braking if the vehicle is approximated with a concentrated mass (i.e., the effect of the lumped mass in the single-degree-of-freedom vehicle model can dominate the contribution due to pitching-induced inertial effects arising in the two degrees-of-freedom vehicle model during soft braking).
- The mean value of the IF is almost constant or can slightly reduce as the road roughness level increases. Ultimately, this implies that the contribution to the total bridge displacement attributable to the road roughness under the passage of a vehicle travelling at a constant speed over the entire span can compensate or dominate the dynamic amplification generated by braking as the road roughness level increases.
- The dispersion of the IF values largely depends on which braking conditions and vehicle model is considered. The CoV of the IF values corresponding to hard braking conditions is much lower than those obtained under soft braking conditions. Notably, the most severe estimates of the IF in terms of the mean value (corresponding to hard braking condition) are associated with lower dispersion. And the CoV of the IF values corresponding to a two-degrees-of-freedom vehicle model are significantly larger than those estimated considering a single-degree-of-freedom vehicle model. Another interesting finding is that an increment of the road roughness level corresponds to a reduction of the CoV for the IF in the case of hard braking conditions while it does not produce significant effects otherwise.

Table 5.3-1 – Statistics of the IF estimates (CoV: coefficient of variation).

Parameters	Roughness	$IF_{1,hb,st}$	$IF_{1,bl,st}$	$IF_{1,bl,nst}$	$IF_{2,hb,st}$	$IF_{2,nl,st}$	$IF_{2,bl,nst}$
Mean	Class A	1.048714	0.663515	0.700208	1.053947	0.527481	0.532239
Variance		0.004231	0.039081	0.048095	0.021834	0.063127	0.064687
CoV		0.062026	0.297944	0.313202	0.140201	0.476322	0.47786
Mean	Class B	1.011531	0.669867	0.673822	1.038816	0.530142	0.530422
Variance		0.000258	0.038312	0.039582	0.004709	0.062202	0.062297
CoV		0.015892	0.292199	0.29526	0.066057	0.470446	0.470556
Mean	Class C	1.011531	0.669867	0.673822	1.038816	0.530142	0.530422
Variance		0.000258	0.038312	0.039582	0.004709	0.062202	0.062297
CoV		0.015892	0.292199	0.29526	0.066057	0.470446	0.470556

5.3.2 Experimental validation

An experimental investigation has been finally performed to evaluate the accuracy of the numerical predictions. Dynamic tests have been carried out for the considered case study by employing a two-axes vehicle. A single bridge span is considered in experimental tests. It is pointed out that vehicle model parameters in Table 7 are retrieved from the available technical documentation expect for vehicle frequencies and viscous damping coefficient, which have been estimated through dynamic tests. Regrettably, it was not possible to evaluate the roughness of the road profile. Therefore, it is assumed a road roughness level corresponds to class A since the bridge belongs to a motorway network. Experimental values and numerical predictions of the IF are compared in Figure 5.3-2. As regards the numerical predictions of the IF through the physics-based model, mean and confidence bounds are estimated from the set of 2,000 random simulations. Conversely, the estimates of the IF obtained from surrogate models should be considered as nominal values.

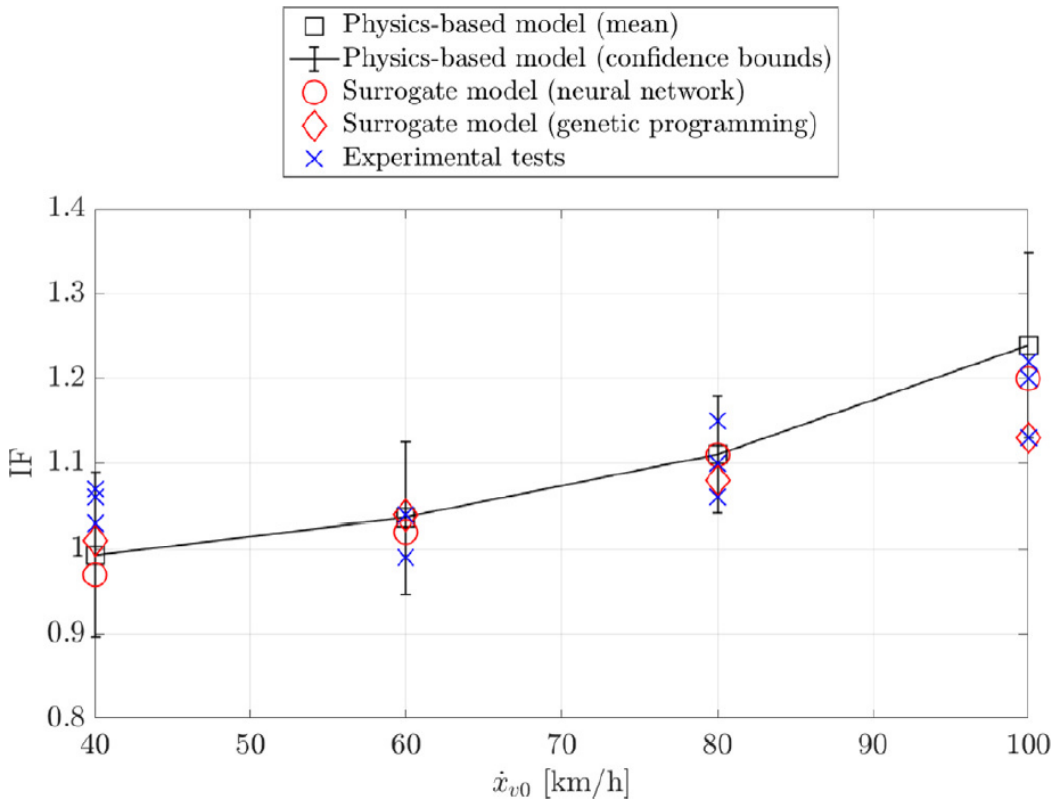

Figure 5.3-2 – Variation of IF as a function of the vehicle velocity: confidence bounds estimated using the physics-based model, nominal values carried out through surrogate modelling, and experimental data.

In agreement with Deng and Wang (2015), the experimental values in Figure 5.3-2 demonstrate that the IF can be close to or larger than 1.3, even under good road surface conditions. Figure 5.3-2 also shows that experimental values of the IF fall within the confidence bounds estimated by using the physics-based model of the dynamic vehicle–bridge interaction. A general overview of the results confirms that physics-based models and surrogate models are both able to predict accurately the IF.

5.4 References

Aloisio, A., Contento, A., Alaggio, R., & Quaranta, G. (2023). Physics-based models, surrogate models and experimental assessment of the vehicle–bridge interaction in braking conditions. Mechanical Systems and Signal Processing, 194, 110276.

Azimi, H., Galal, K., & Pekau, O. A. (2013). A numerical element for vehicle–bridge interaction analysis of vehicles experiencing sudden deceleration. Engineering Structures, 49, 792-805.

Broniszewski, J., & Piechna, J. (2019). A fully coupled analysis of unsteady aerodynamics impact on vehicle dynamics during braking. Engineering Applications of Computational Fluid Mechanics, 13(1), 623-641.

Cahill, P., Jaksic, V., Keane, J., O'Sullivan, A., Mathewson, A., Ali, S. F., & Pakrashi, V. (2016). Effect of road surface, vehicle, and device characteristics on energy harvesting from bridge–vehicle interactions. Computer-Aided Civil and Infrastructure Engineering, 31(12), 921-935.

Cheema, P., Alamdari, M. M., Chang, K. C., Kim, C. W., & Sugiyama, M. (2022). A drive-by bridge inspection framework using non-parametric clusters over projected data manifolds. Mechanical Systems and Signal Processing, 180, 109401.

Chompooming, K., & Yener, M. (1995). The influence of roadway surface irregularities and vehicle deceleration on bridge dynamics using the method of lines. Journal of Sound and Vibration, 183(4), 567-589.

Deng, L., & Wang, F. (2015). Impact factors of simply supported prestressed concrete girder bridges due to vehicle braking. Journal of Bridge Engineering, 20(11), 06015002.

Deng, L., Yu, Y., Zou, Q., & Cai, C. S. (2015). State-of-the-art review of dynamic impact factors of highway bridges. Journal of Bridge Engineering, 20(5), 04014080.

Ekart, A., & Nemeth, S. Z. (2001). Selection based on the pareto nondomination criterion for controlling code growth in genetic programming. Genetic Programming and Evolvable Machines, 2, 61-73.

Gao, W., Li, G., Su, Q., & Han, W. (2022). Impact of rigid central clamps on longitudinal deformation of long-span suspension bridges under vehicle excitations. Structure and Infrastructure Engineering, 18(6), 760-774.

Guner, R. U. K. İ. Y. E., Yavuz, N., Kopmaz, O., Ozturk, F. E. R. R. U. H., & Korkmaz, I. (2004). Validation of analytical model of vehicle brake system. International Journal of Vehicle Design, 35(4), 331-348.

Henchi, K., Fafard, M., Talbot, M., & Dhatt, G. (1998). An efficient algorithm for dynamic analysis of bridges under moving vehicles using a coupled modal and physical components approach. Journal of Sound and Vibration, 212(4), 663-683.

Ju, S. H., & Lin, H. T. (2007). A finite element model of vehicle–bridge interaction considering braking and acceleration. Journal of Sound and Vibration, 303(1-2), 46-57.

Li, J., Zhu, X., & Guo, J. (2022). Enhanced drive-by bridge modal identification via dual Kalman filter and singular spectrum analysis. Structural Control and Health Monitoring, 29(5), e2927.

Mokalled, S., Locke, W., Abuodeh, O., Redmond, L., & McMahan, C. (2022). Drive-by health monitoring of highway bridges using Bayesian estimation technique for damage classification. Structural Control and Health Monitoring, 29(6), e2944.

Ni, P., Li, J., Hao, H., & Zhou, H. (2021). Reliability based design optimization of bridges considering bridge-vehicle interaction by Kriging surrogate model. Engineering Structures, 246, 112989.

Quaranta, G., Lacarbonara, W., & Masri, S. F. (2020). A review on computational intelligence for identification of nonlinear dynamical systems. Nonlinear Dynamics, 99(2), 1709-1761.

Sasidhar, M. N. V., & Talukdar, S. (2003). Nonstationary response of bridge due to eccentrically moving vehicles at variable velocity. Advances in Structural Engineering, 6(4), 309-324.

Yang, J. P., & Sun, J. Y. (2020). Pitching effect of a three-mass vehicle model for analyzing vehicle-bridge interaction. Engineering Structures, 224, 111248.

Yang, Y. B., & Lin, B. H. (1995). Vehicle-bridge interaction analysis by dynamic condensation method. Journal of Structural Engineering, 121(11), 1636-1643.

Yu, H., Wang, B., Li, Y., Zhang, Y., & Zhang, W. (2018). Road Vehicle-Bridge Interaction considering Varied Vehicle Speed Based on Convenient Combination of Simulink and ANSYS. Shock and Vibration, 2018(1), 1389628.

Zhang, L. J., Lee, C. M., & Wang, Y. S. (2002). A study on nonstationary random vibration of a vehicle in time and frequency domains. International Journal of Automotive Technology, 3(3), 101-109.

Zhang, Y., Zhao, H., & Lie, S. T. (2018). A nonlinear multi-spring tire model for dynamic analysis of vehicle-bridge interaction system considering separation and road roughness. Journal of Sound and Vibration, 436, 112-137.

Zhu, X. Q., & Law, S. S. (2015). Structural health monitoring based on vehicle-bridge interaction: accomplishments and challenges. Advances in Structural Engineering, 18(12), 1999-2015.

6. Data-driven numerical modeling of water infrastructure

6.1 Introduction

Water infrastructures systems intrinsically recall the systemic nature being defined as the set of elements distinct in terms of properties and functions, mutually interconnected, interacting with each other and with the external environment, to allow the collection, adduction, purification and distribution of water resources; they react or evolve as a whole connected to the environmental, economic and social context in a bidirectional way. This definition is consistent with the identification of water systems as critical infrastructures because of their impact on the socio-economic context of the environment in which they develop (Mohammed et al., 2022). As regards drinking water distribution systems, the progressive extension of the networks is superimposable to urban expansion, often sharing the lack of a harmonious project in their development (Agathokleous et al., 2017). The growing territorial extension of the water distribution systems has shown the need for a regulation of water services to harmonize the economic-financial goals with the general objectives of social nature, environmental protection and efficient use of resources. A significant route could therefore be one that allows promoting the investments needed to address a specific criticality, such as water losses or continuity of the water service, and the planning of interventions that enhance the overall increase in the resilience of water distribution systems, also including the quality of water from the withdrawal from the environment to the users. Data-driven numerical modeling uses information about the infrastructure and the monitoring of hydraulic parameters, water consumption and water quality. If overall assessments of the impact of environmental changes are introduced, including those related to climate and the economic and social context, numerical modeling can provide indications from the overall to the local, both in terms of impact understood as the criticality that is generated, and in terms of efficiency of actions that can be implemented at a structural, managerial level or intended to impact on water demand. Numerical modelling can therefore support the process of identifying interventions, allowing the creation of scenarios and the evaluation of impacts; in fact, planning and design are intrinsically multi-criteria and multi-phase (Cunha et al., 2019). The approach consequently requires considering the uncertainty of the boundary conditions and being dynamic, incremental and adaptive. Also, acute challenges such as cyber-attacks and extreme weather events, together with future pressures, such as climate change, population growth, and economic and social change, may increase in intensity and unpredictability (Ofwat, 2017). The impact of technological advances in the possibilities of monitoring and data transmission allows to have useful information to describe the infrastructural and operational status of water distribution systems, as well as to understand the impact of management choices.

6.2 Main features of the proposed methodology

Urban areas, by virtue of the concentration of population and human activities, represent particularly critical contexts. Ofwat (2015) propose a non-exhaustive map of the interdependencies between water infrastructure and the environmental, social and economic context (Figure 6.2-1). Future scenarios must therefore be linked to the evolution of domestic water needs and industrial and agricultural activities. Furthermore, the characterization of users, facilitated by the installation of smart meters, can allow the subsequent transition to georeferenced scenarios of water needs. The availability of digital models of the water infrastructure, at the georeferenced graph and hydraulic model level, can help in defining critical scenarios that consider interdependencies (Aljadhai S. & Abraham, 2018) and therefore in the implementation of intervention and mitigation measures (Figure 6.2-2). Data-driven numerical modeling includes multiple dimensions, closely connected due to the systemic nature of the water distribution networks: topological dimension, that can be addressed based on graph theory; structural dimension, with models representing the state of degradation of

the infrastructure; hydraulic dimension, reproduced by means models that represent the fluid motion; environmental dimension, based on the representation of boundary conditions; social and economic dimension, based on models representing water demand by quantifying current and future needs. The proposed methodology aims to connect the different dimensions of modeling by communicating data and models for an approach oriented to an analysis and therefore to a global vision of water distribution systems.

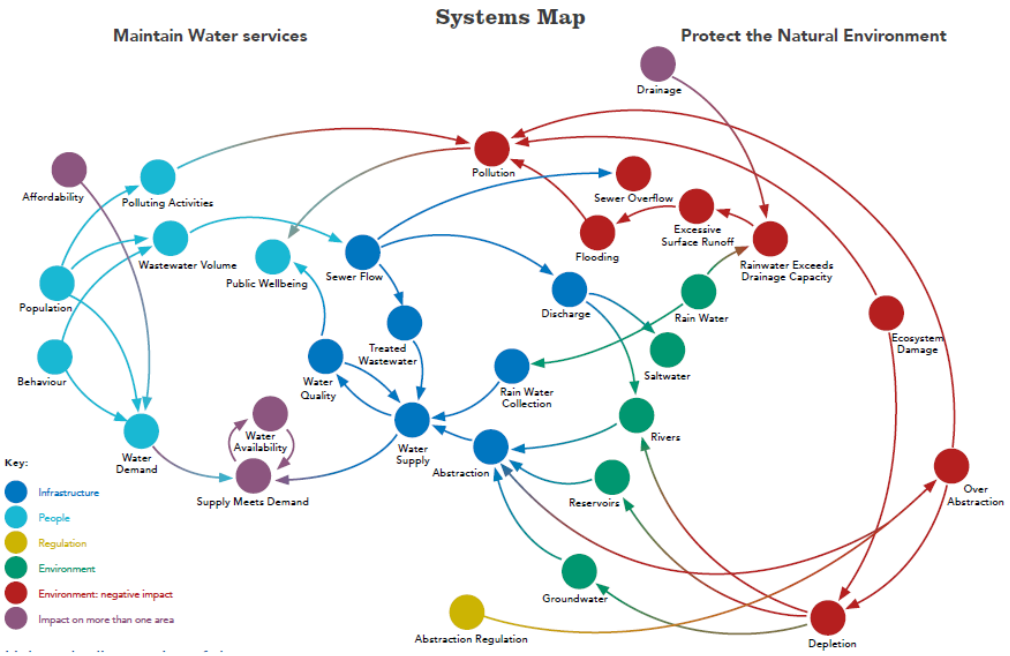

Figure 6.2-1 – Map of interdependencies between water infrastructure and the environmental, social and economic context (Ofwat, 2015).

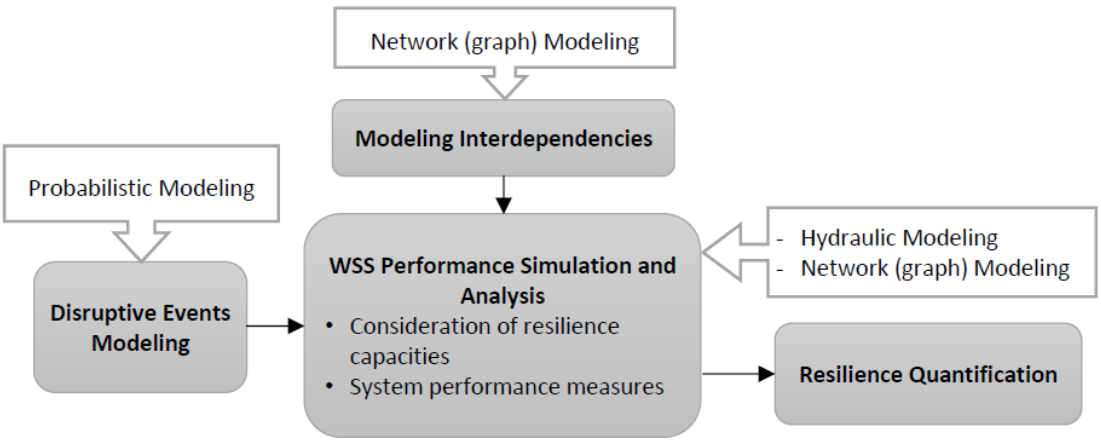

Figure 6.2-2 – Framework components and tools used (Aljadhai et al., 2018).

6.2.1 Topological dimension in numerical modeling

Water Distribution Systems (WDS) can be modeled in the topological dimension as complex graphs whose development took place in successive stages. Porse E. & Lund J. (2016) use graph theory to characterize a network and identify the connectivity as a measure of resilience from the infrastructure point of view. If the network as a whole is seen as a connected graph, each edge has a different importance within the real system. The concept of a subset of continuously connected pipes mainly dedicated to transport water from the sources to the pipes instead dedicated to supply users is consolidated, but in large looped WDN the identification of

this subset is not uniquely determined. A part of literature is indeed dedicated to the degree of importance of each pipeline, often measured on the impact in terms of hydraulic operation and satisfaction of water consumption that an interruption of its flow could cause. Identifying the main connections between water production, processing and distribution sites can give a clearer comprehension of their structure, importance and criticality (Fortini et al., 2014). If in a completely open WDN, this distinction between pipes mainly dedicated to transport water and pipes instead dedicated to supply users has lost importance, it becomes a key aspect in a sectorization design. An approach to determine the pipes mainly dedicated to transport water is presented by Brentan et al. (2018) in which they define the trunk main through a process based on the shortest-path concept derived from graph theory associated to the flow in each pipe. Several general criteria distinguish the trunk network from the distribution network, such as diameters, connections, and locations. In general, the connection to the trunk network is restricted to medium-diameter and large-diameter pipes. Ferrari et al. (2014) identify water transmission mains as the series of connected pipes having a diameter equal to or greater than a threshold used to extend and convey water between sources, such as storage facilities, external water supply networks, wells, springs. Thus, the distinction made in the definition of transmission mains and distribution mains is a function of the size of the water system itself. The concept of pipes mainly dedicated to transport water in the sectorization of WDN is also considered in Liu and Lansey (2020), in which the feed pipes are determined as first phase of a multiphase approach to design a defined number of sectors. Identification of the trunk network is not a trivial matter as it determines to some extent the final partition of WDN and thus the implementation of sectors costs and the hydraulic performance of the sectorized WDN (Herrera et al., 2016; Zhang et al., 2019, 2021). These main pipes refer to the pipes that have large diameters and transport a large amount of water. Each branch pipe on the main pipes can be considered as a possible outset of the sectors in design and the water is supplied from the main pipes to sectors through the branch pipes (Zhang et al., 2019). In Diao et al. (2016), the WDS is decomposed into a twin-hierarchy pipeline structure consisting of backbone mains and community feeders. The backbone mains refer to all the most critical paths forming the backbone network of the system. For instance, trunks connecting critical infrastructures, e.g., reservoirs, tanks, and pump stations, thus changes of any backbone mains will have significant impacts on the whole system's water supply (e.g., water demand supplied, pressure, energy consumption). Graph theory and standard graph metrics of betweenness centrality (Freeman, 1977) and connectivity were adapted to account for connectivity to supply points in the system by Giustolisi et al. (2019) and Chen et al. (2021). This approach to define pipeline criticality assessments can be used as a mirror reading in terms of importance of the pipes; this type of approach can be further refined if the hydraulic model is available (Dunn & Wilkinson, 2013; Meijer et al., 2021).

6.2.2 Numerical modeling for Primary network analysis

WDS is assumed to be described by means an undirected weighted graph G = (N, E) where N is the set of nodes and E is the set of edges. Each edge is associated with a nonnegative weight. The graph G can comprehend multiple edges between the same pair of nodes. The node set N includes a subset NP ⊂ N of primary nodes, which correspond to water resources inlet nodes, storage volumes as reservoirs or tanks, nodes for providing water to other WDSs or users of particular strategic importance (as hospitals, schools, military zones). Given the undirected weighted graph G = (N, E), the Primary Network (PN) is identified by means the algorithm proposed in Zingali et al. (2024) in which PN is defined as a connected sub-graph which meets some criteria: (i) given the strategic relevance of primary nodes, PN is request to connects the subset NP ⊂ N by means the minimum weighted path; (ii) PN is a non-tree subgraph to guarantee a certain degree of redundancy; (iii) PN must transport a proper fraction of the water consumption within its edges. The criteria (i) and (ii) are mainly direct to the interconnection of primary nodes; all the criteria (i), (ii) and (iii) are mostly applied to sustain an eventual WDS sectorization.

6.2.3 Structural dimension in numerical modeling

In the modeling of the structural dimension, identifying the key factors that influence the pipe failure is a key task in developing reliable prediction models (Farmani et al., 2017). According to a recent review, these factors can be generally grouped into three types according to their attributes in WDS: physical, operational, environmental, social and economic (Fun et al., 2023; Taiwo et al., 2023). In Taiwo et al. (2023) and Forero-Ortiz et al. (2023) a systematic review of the techniques used in modeling the failure probability of water pipes, including physical, statistical, machine-learning (ML)-based (Fun et al., 2023; Zali et al., 2024) and combined models are presented (Figure 6.2-3). In Figure 6.2-4a, a brief discussion about the frequency analysis of the factors that influence the failure of water pipes, which are resultantly used in developing the prediction models and material types used in prior investigations, are shown.

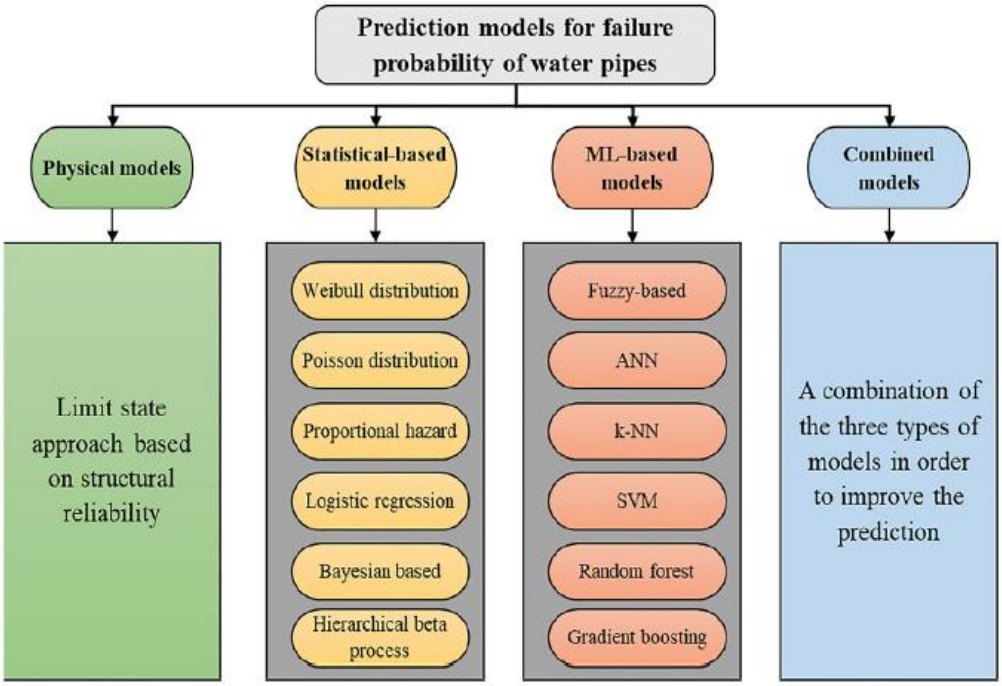

Figure 6.2-3 – Prediction models for failure probability of water pipes (Taiwo et al., 2023).

6.2.4 Hydraulic dimension in numerical modeling

The hydraulic analysis is based on the Water Network Tool for Resilience (WNTR) that is an EPANET compatible Python package designed to simulate and analyze resilience of water distribution networks (Klise et al., 2017). The official WNTR software repository is hosted in the U.S. EPA's GitHub organization (USEPA/WNTR). WNTR is a Python package, which requires Python along with several Python package dependencies, including NetworkX, Pandas, Matplotlib, NumPy, and SciPy. Leveraging the object-oriented programming capabilities of Python, WNTR easily performs many complex analyses. The primary modeling components in WNTR include: (1) disaster models (e.g., attenuation models to predict ground movement after an earthquake), (2) fragility curves used to assign the probability of damage to network components, (3) flexible controls to change the status and operation of network components, (4) models to estimate leaks in the network, (5) PDD hydraulic simulation to model the network during low pressure conditions, (6) resilience metrics to evaluate the effect of the disruption and repair strategies, and (7) the ability to perform Monte Carlo simulations. WNTR uses a PDD model proposed by Wagner et al. (1988):

$$d = \begin{cases} 0 & p \leq P_0 \\ D_f \sqrt{\dfrac{p - P_0}{p_f - P_0}} & P_0 < p < P_f, \\ D_f & p \geq P_f \end{cases} \tag{6.2-1}$$

where d is the actual demand delivered to customers (m^3/s), D_f is the customers expected demand (m^3/s), p is the pressure (Pa), P_f is the pressure above which the customer should receive the expected demand (Pa), and P_0 is the pressure below which the customers cannot receive any water (Pa). P_f and P_0 can be defined at each node and can be modified by the user. The available water resource derived from abstraction from the aquifer was modeled with reference to the scheme shown in Figure 6.2-5. It is modeled as a reservoir with constant hydraulic head and infinite capacity (fixed-head element), to which a hydraulic head equal to zero was assigned, connected with a pump. The rule of this pump is to reproduce the dynamic behavior of the aquifer; it is therefore assigned a characteristic curve with a linear trend as a function of the abstracted flow rate. The data used to construct this curve were provided by the water utility and cross-checked with data supplied by ARPAE. The second pump, installed in series with the first one, represents the actual well pump and it is characterized by the performance curve of the installed hydraulic machine.

Category	Predictors	Frequency	Normalized frequency
Physical and pipe related	Age	26	0.546
	Burial depth	4	
	Coating	2	
	Crack depth	4	
	Diameter	35	
	Length	22	
	Material type	27	
	Number of hydrants	2	
	Number of valves	2	
	Elastic modulus	8	
	Thickness	14	
Total		146	
Environment-related	Bedding condition	2	0.288
	Cold days	2	
	Corrosion depth	3	
	Corrosion length	2	
	Surface load	3	
	Frost load	4	
	Groundwater condition	1	
	Hot days	2	
	Land use	2	
	Precipitation	2	
	Soil corrosivity	13	
	Soil elastic modulus	5	
	Soil type	6	
	Temperature	9	
	Traffic load	13	
	Unit weight of soil	8	
Total		77	
Operation-related	Internal pressure	25	0.161
	Number of previous breaks	12	
	Water age	1	
	Water pH	2	
	Water temperature	1	
	Water velocity	2	
Total		43	
Social-related	Population	1	0.003
Total		1	
Grand total		267	

(a)

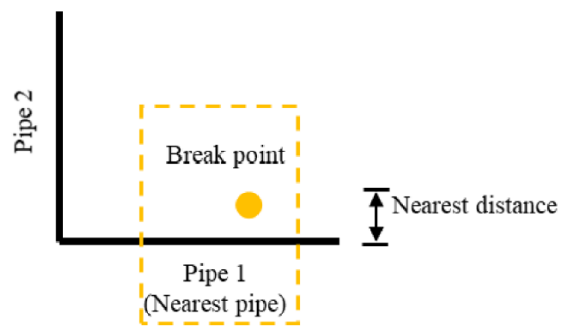

(b)

Figure 6.2-4 – Descriptive statistics of the influencing factors (Taiwo et al., 2023); (b) pipe break dataset aggregated based on nearest distance of break point to the pipe (Fun et al., 2022).

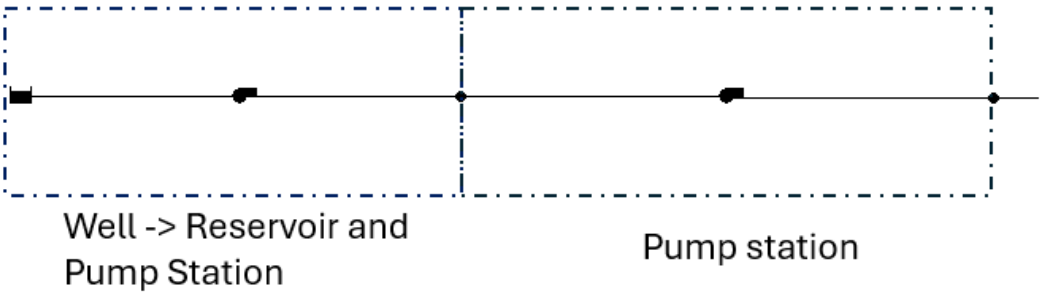

Figure 6.2-5 – Well system modeling scheme.

6.3 Case study: Parma water distribution systems

The water distribution system (WDS) of Parma was identified as case study within the area managed by IREN SpA. An advanced hydraulic (physically-based) model of a real-world water supply network has been implemented in WNTR Python package able to perform multiple analysis. The pressure-driven model will be used on long-term simulation under changeable water resources and water demand scenarios. The results will be able to be included in the assessment of a realistic vulnerability and in the validation of possible interventions for the mitigation of the associated risk.

The model is composed of 24020 nodes of which 23990 junctions, 5 tanks, and 25 reservoirs and 25052 links of which 18503 pipes, 6476 valves and 73 pumps. The length of the pipes is 832.7 km. The average demand allocated to the nodes is 612 l/s of which 68% water consumption and 32% leakage. In the model, demand pattern is characterized by type of user and area. The reservoirs represent suction tanks of a pumping station and 24 wells. In order to model the drawdown of a water table due to withdrawal depending on the pumping rate, the well was modeled as a reservoir with a pump that has a linear characteristic curve which at zero flow rate gives a head equal to the height of the water table without withdrawal and which at the maximum withdrawal rate gives a head corresponding to the lowering of the water table for that withdrawal. WDS in the modeled scenario is supplied by 13 active wells and the reservoir, that represent a suction tank of pumping station. There are 3 junctions in the hydraulic model, which are transfer nodes that supply other water distribution systems.

6.3.1 Topological dimension: Primary Network analysis of Parma WDS

The connection of the primary nodes of WDN (the network's resources Reservoirs and Tanks) was analyzed by the algorithm proposed in Zingali et al. (2024). In Figure 6.3-1 a Steiner tree was determined, which represents the minimum tree that connects the network's 29 primary nodes A weight were assigned at the pipes equal to L/D^5. The resulting Steiner tree, as shown in the figure, has a length of 48.8 km and an equivalent diameter (D) of 166 mm, which the weighted average of the diameters based on the length.

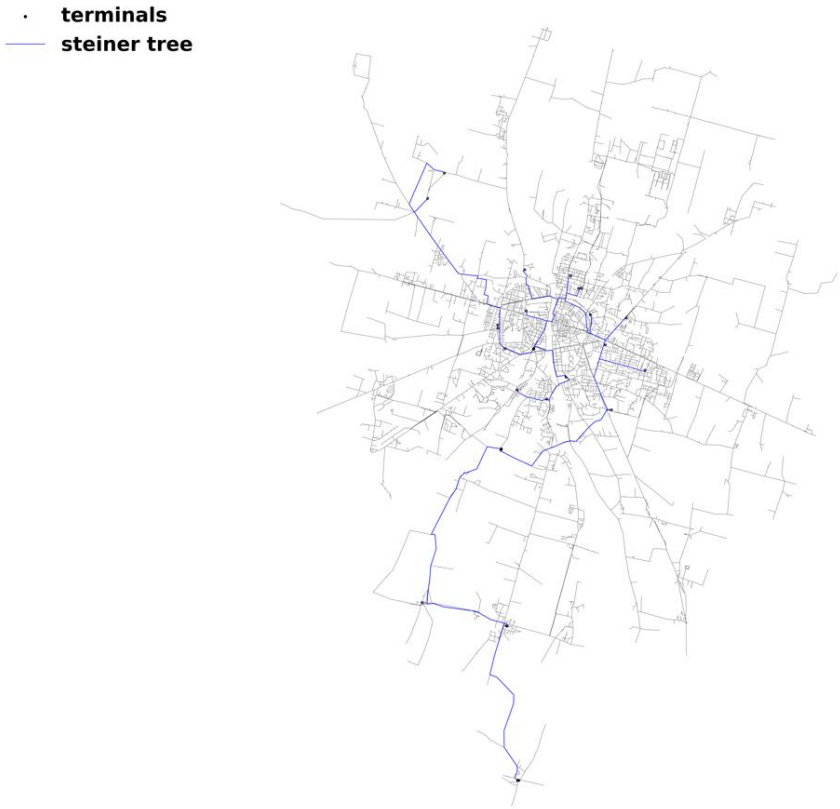

Figure 6.3-1 – Primary Network by the algorithm proposed in Zingali et al. (2024): Steiner Tree Network.

6.3.2 Hydraulic dimension: WNTR analysis with the numerical model of Parma WDS

The hydraulic model is able to simulate the dependence of the leakage on pressure. The nodes in which the leakage is allocated are emitter nodes with a discharge coefficient. In Figure 6.3-2 the global water balance results from Pressure Driven Analysis (PDA) is shown, the black line represents the total demand in the network (users consumption, leakage and transfer nodes), the flow in blue represents the demand withdrawn into the system (user consumption and leakage) or the total demand in the network minus the flow outgoing to other WDSs, and in red it can observe the variable trend of the leakage over the simulation time due to the pressure dependence.

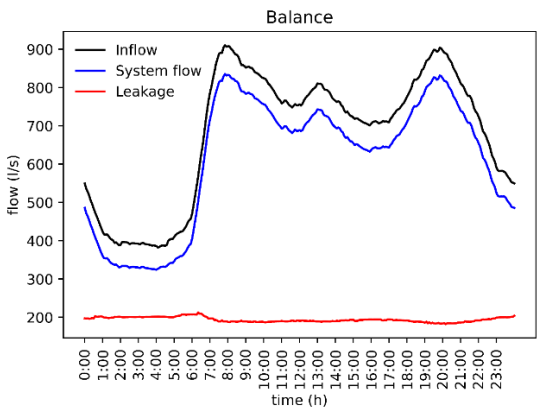

Figure 6.3-2 – WNTR PDA results: flow rate entering the system is represented in black; the system demand (user consumption and leakage) in blue, obtained subtracting water transfers to other systems; finally, leakage flow rate in red.

The simulation model does not identify critical pressure conditions in the simulation period, except for isolated cases at nodes without user demand. In Figure 6.3-3 WNTR PDA results obtained by the hydraulic model are presented showing the maps of maximum, average and minimum pressures and relative percentage distribution at the nodes of the Parma water distribution system model, respectively in (a), (b) and (c).

6.3.3 Structural dimension in numerical model of Parma WDS

The data were processed in the open source QGIS environment (https://www.qgis.org/), which allows to visualize, organize, analyze and represent spatial data. For a more in-depth analysis of the state of the water infrastructure, the breaks shapefile of the years 2022 and 2023 was uploaded into the QGIS project. Thanks to the potential of QGIS and the geo-localization of the interventions provided by IREN SpA, it was possible to have an overlapping view of the water distribution model of Parma with the associated interventions (Figure 6.2-4b). The purpose of this processing is to extract from the data provided the information useful for conducting a study on the fragility of the network, trying to understand the main causes. Furthermore, this analysis creates the base for attempting to interpret the degradation phenomena and therefore can provide information on the priority of interventions.

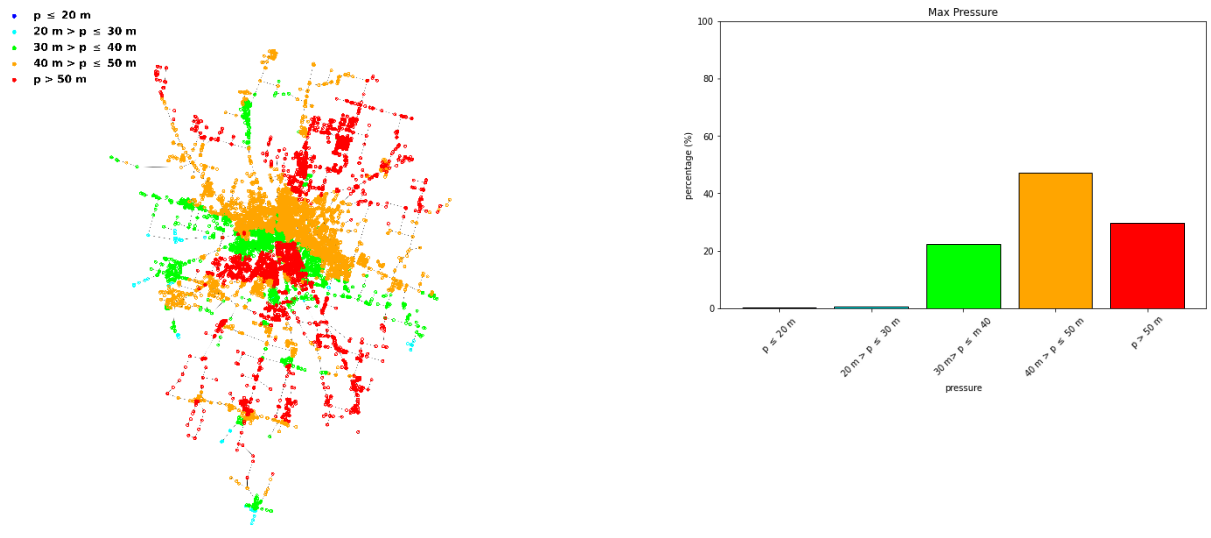

(a)

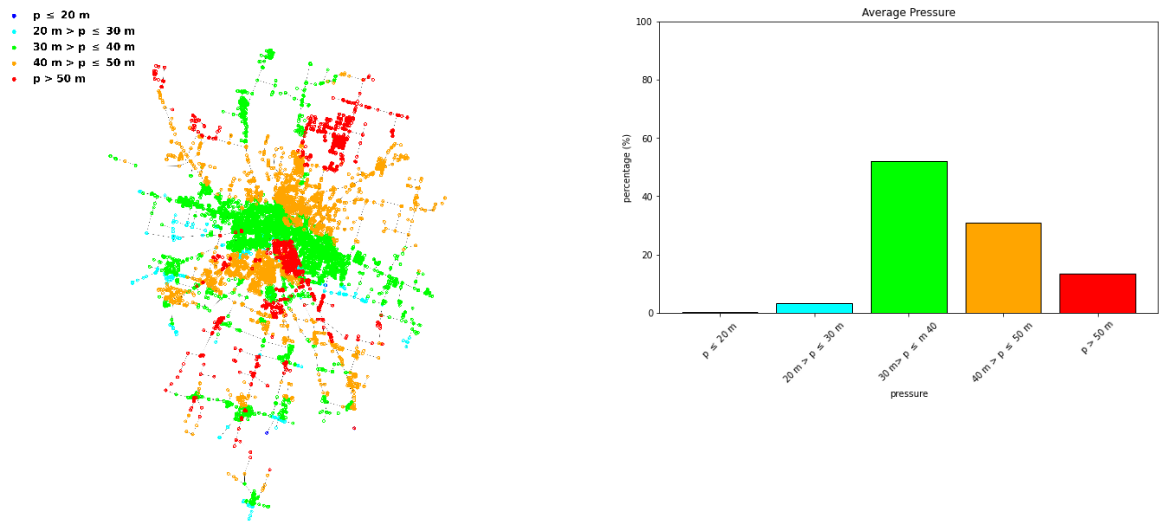

(b)

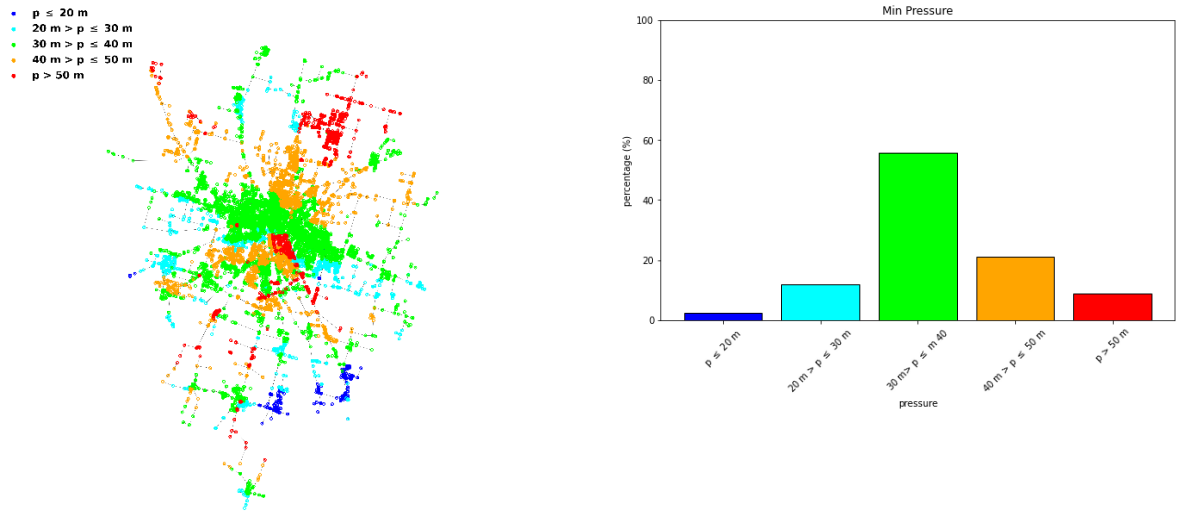

(c)

Figure 6.3-3 – WNTR PDA results: maps of maximum, average and minimum pressures and relative percentage distribution at the nodes of the Parma water distribution system model, respectively in (a), (b) and (c).

Figure 6.3-4 shows the analyses of georeferenced breaks in the water distribution networks of Parma in the period 2022-2023. Table 6.3-1 shows the analysis of the breaks in the period 2022-2023 that affected the pipelines present in the Parma water distribution network model in relation to the material; the percentage of the total breaks that occurred for each material and the relative percentage in terms of length of the network corresponding to each material are indicated; furthermore, the average break rate (number of breaks per km in a year) in the observation period 2022-2023 is also indicated. Table 6.3-2 shows the analysis of the breaks in the period 2022-2023 that affected the pipes present in the Parma water distribution network model in relation to the diameter; the percentage of the total breaks that occurred for each diameter class and the relative percentage in terms of length of the corresponding network are indicated; furthermore, the average break rate (number of breaks per km in a year) in the observation period 2022-2023 is also indicated.

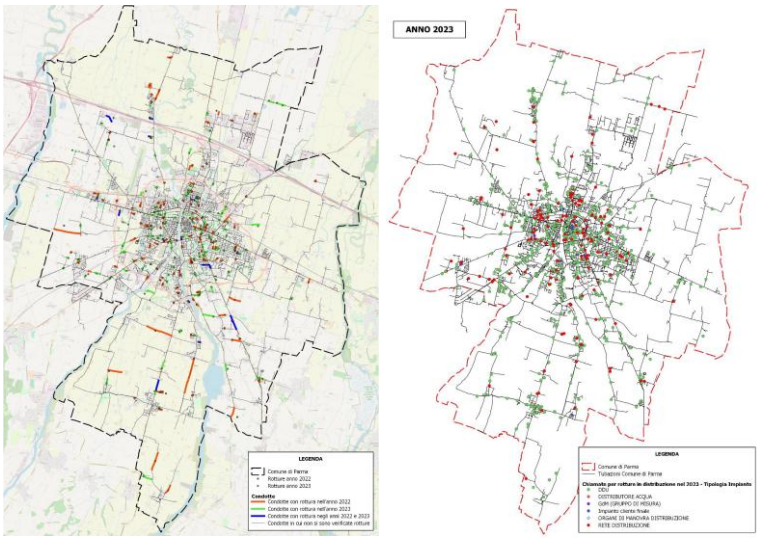

(a) (b)

Figure 6.3-4 – (a) grouping of pipelines that did not suffer any breaks in the period 2022-2023 (black line), that suffered breaks in 2022 (orange line), in 2023 (green line) or that suffered breaks in both years (blue line); (b) interventions on water network in 2023 based on the type: breaks on water pipelines (red dots) and breaks on user connections (green dots).

Table 6.3-1 – Water distribution network of Parma: distribution of breaks as a function of the pipe material.

Material	%breaks	% relative length	Rate of failure breaks/(km*year)
Cast iron	28,6	9,5	0,308
Asbestos cement	39,2	47,7	0,155
Polyethylene	25,4	17,5	0,189
Welded Steel	6,8	25,3	0,134

Table 6.3-2 – Water distribution network of Parma: distribution of breaks as a function of the diameter.

Diameter (mm)	% relative length	% breaks	Rate of failure breaks/(km*year)
D≤50	1,6%	7,9%	0,927
50≤D<90	14,8%	50,3%	0,651
90≤D<125	39,0%	33,3%	0,163
125≤D<175	27,3%	3,5%	0,024
175≤D<300	9,0%	1,3%	0,027
D≥300	8,3%	3,8%	0,086

6.4 Vulnerability assessment scenarios

The vulnerability analysis identified realistic future criticalities that could affect the security of drinking water supply for the case study. The analysis of population projections did not indicate significant population growth, as the population balance in the absence of immigration is negative. The drinking water demand was therefore assumed to be stationary, and the focus was placed on water resource availability. The vulnerability of the supply system was analyzed by considering two types of scenarios. The first vulnerability analysis concerns the current conditions and assumes the unavailability of a group of wells, a scenario attributable either to pumping system malfunction or to the inability to use the related water resource due to quality issues. The second vulnerability analysis, instead, considers a future generalized lowering of the groundwater table, in order to assess whether the current pumping facilities are capable of compensating for this drawdown. The results of these scenarios, particularly those of the future scenario, should be interpreted considering that the operation of the water distribution network was simulated while maintaining the constraints imposed by the current district-based configuration. Consequently, in the future, the structure of the district-based distribution network could be revised to mitigate the effects induced by changes in water resource availability.

6.4.1 Vulnerability assessment on the current scenario

The vulnerability assessment on the current scenario concerns the unavailability of an important groups of wells, which at present provides an average flow rate of 91 l/s. Figure 6.4-1 illustrates a representative trend of the production from the well group, which is no longer available in this scenario. The capacity of the water system to compensate for this unavailable flow rate through a different pumping regulation was therefore evaluated. Furthermore Figure 6.4-2illustrates a reduction in the average pressure in the central area of the city compared with the current distribution. This is accompanied by an increase in the number of nodes exhibiting

pressures within the range of 20 to 30 m. In details, numerical results do not identify critical pressure conditions in the simulation period, except for isolated cases at nodes without user demand (Figure 6.4-2).

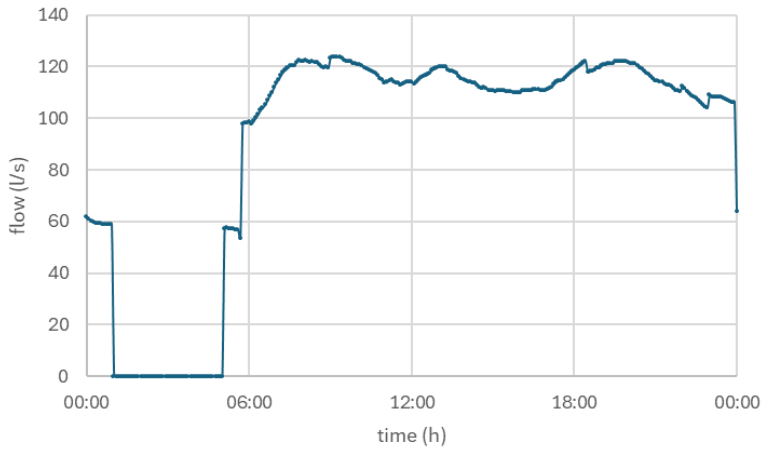

Figure 6.4-1 – WNTR PDA results: representative trend of the production from the well group, which is no longer available in this scenario.

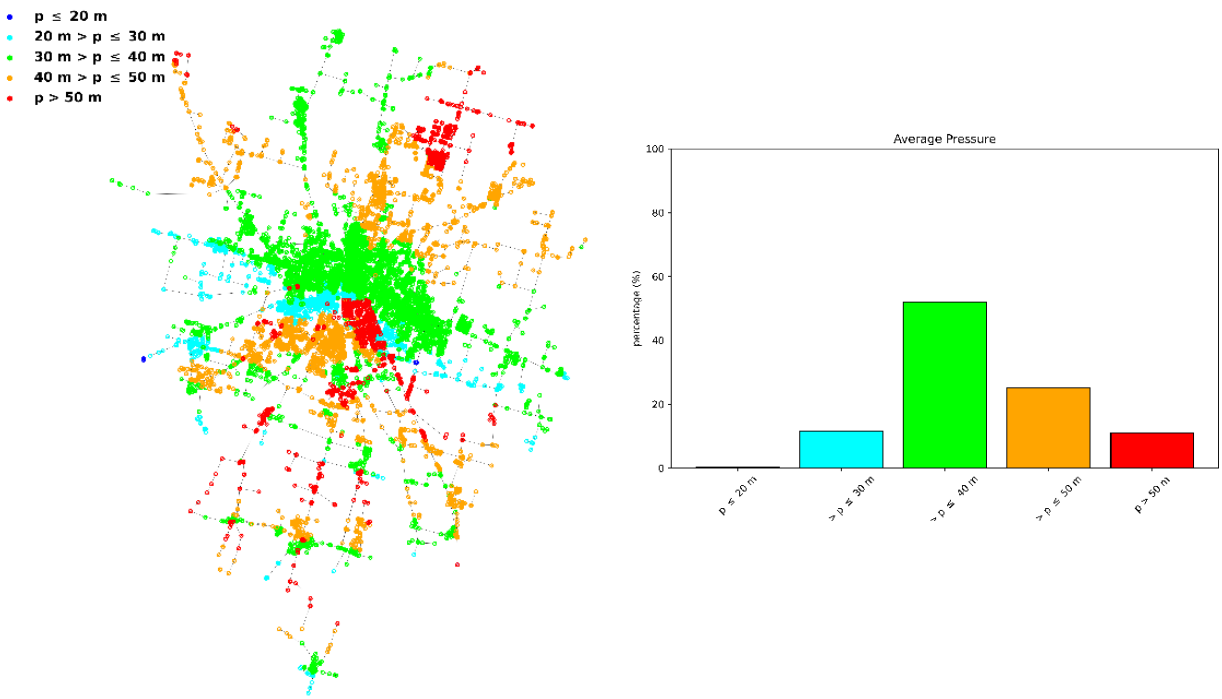

Figure 6.4-2 – WNTR PDA results vulnerability assessment on the current scenario concerns the unavailability of an important groups of wells: maps of average pressures and relative percentage distribution at the nodes of the Parma water distribution system model.

6.4.2 Vulnerability assessment on the future scenario

The vulnerability assessment in the future scenario considers a generalized lowering of the groundwater table, in order to evaluate whether the current pumping stations are capable of compensating for this drawdown. Consequently, in the well system modeling scheme the curve representing the drawdown of the water level as a function of the abstracted flow rate was lowered, as illustrated in Figure 6.4-3.

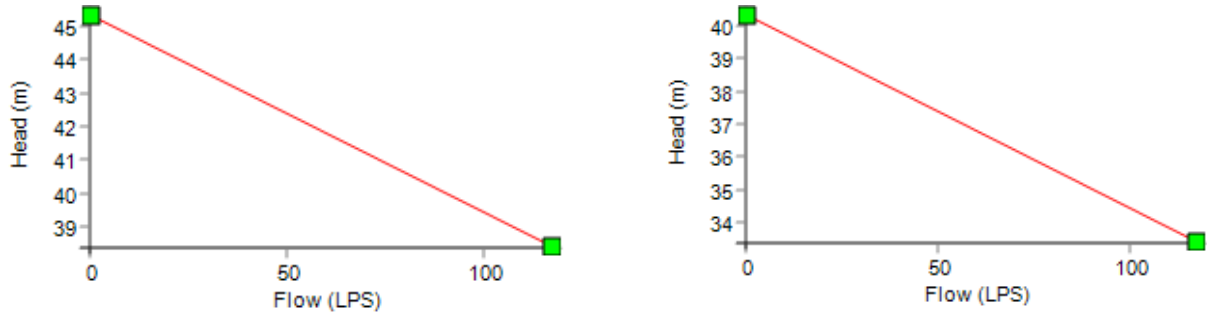

Figure 6.4-3 – WNTR PDA model: drawdown of the dynamic groundwater level as shown in the curve, consistently with the well system modelling scheme shown in Figure 6.2-5.

The results shown in Figure 6.4-4are related to an uniform drawdown of 5 m. Despite the lowering of the groundwater table, the current pumping system can adapt to the new conditions through a different inverter regulation. It should be noted that the proposed configuration is not optimal in terms of pressure control or well selection, but rather represents a limiting scenario designed to test whether the existing pumping facilities can effectively compensate for the variation assumend in this scenario.

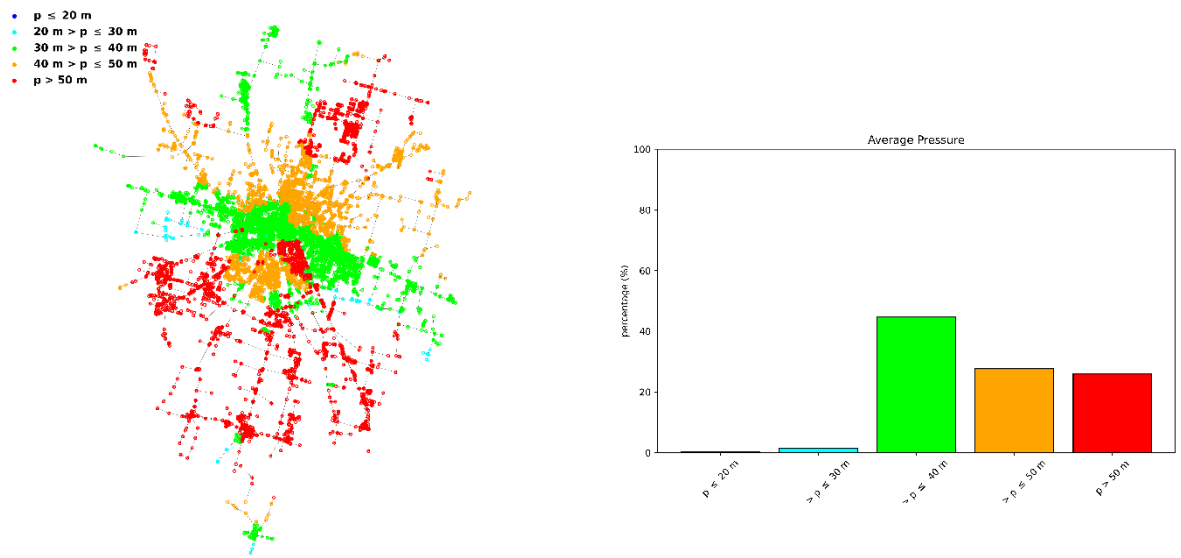

Figure 6.4-4 – WNTR PDA results: maps of average pressures and relative percentage distribution at the nodes of the Parma water distribution system model considers a future generalized lowering of the groundwater table equal to 5 m, in order to assess whether the current pumping facilities are capable of compensating for this drawdown.

6.5 References

Agathokleous A., Christodoulou C., Christodoulou S. E. Topological Robustness and Vulnerability Assessment of Water Distribution Networks, Water Resour Manage (2017) 31:4007–4021.

Aljadhai S. & Abraham D. Quantifying the Resilience of Water Supply Infrastructure Systems: The Role of Infrastructure Interdependency ASCE Construction Research Congress 2018

Brentan, B., Campbell, E., Goulart, T., Manzi, D., Meirelles, G., Herrera, M., Izquierdo, J., Luvizotto, E. (2018). Social network community detection and hybrid optimization for dividing water supply into district metered areas. Journal of Water Resources Planning and Management, 144(5):04018020.

Chen, T. Y.-J., Vladeanu, G., and Daly, C. M. (2021). Pipe Criticality Assessment without a Hydraulic Model, pages 115–124.

Cunha M., Marques J., Creaco E., Savic D. A Dynamic Adaptive Approach for Water Distribution Network Design J. Water Resour. Plann. Manage., 2019, 145(7).

Diao, K., Fu, G., Farmani, R., Guidolin, M., and Butler, D. (2016). Twin-hierarchy decomposition for optimal design of water distribution systems. Journal of Water Resources Planning and Management, 142(5):C4015008.

Dunn S., Wilkinson S. M. Identifying Critical Components in Infrastructure Networks Using Network Topology J. Infrastruct. Syst. 2013.19:157-165.

Fan, X., Wang, X., Zhang, X., Xiong B.Yu (2022). Machine learning based water pipe failure prediction: The effects of engineering, geology, climate and socio-economic factors. Reliability Engineering & System Safety, 219, 108185.

Farmani R., Kakoudakis K., Behzadian K., Butler D. (2017). Pipe Failure Prediction in Water Distribution Systems Considering Static and Dynamic Factors, WDSA Procedia Engineering 186, 117 – 126.

Ferrari, G., Savic, D., and Becciu, G. (2014). Graph-theoretic approach and sound engineering principles for design of district metered areas. Journal of Water Resources Planning and Management, 140(12):04014036.

Forero-Ortiz E., Martinez-Gomariz E., Sanchez-Juny M., Gonzalez J. C., Cucchietti F., Viader F. B., Monton M. S. (2023). Models and explanatory variables in modelling failure for drinking water pipes to support asset management: a mixed literature review, Applied Water Science, 13:210.

Fortini, M., Bragalli, C., and Artina, S. (2014). Identifying the high-level flow model of water distribution networks using graph theory. Procedia Engineering, 89:1192–1199. 16th Water Distribution System Analysis Conference, WDSA2014.

Freeman, L. C. (1977). A set of measures of centrality based on betweenness. Sociometry, 40(1):35–41.

Giustolisi, O., Ridolfi, L., and Simone, A. (2019). Tailoring Centrality Metrics for Water Distribution Networks. Water Resources Research, 55(3):2348–2369.

Herrera M., Abraham E., Stoianov I. A Graph-Theoretic Framework for Assessing the Resilience of Sectorised Water Distribution Networks. Water Resour Manage (2016) 30:1685–1699.

Klise K. A., Bynum M., Moriarty D., Murray R. (2017). A software framework for assessing the resilience of drinking water systems to disasters with an example earthquake case study Environmental Modelling & Software 95, 420-431

Liu, J., Lansey, K. E. (2020). Multiphase DMA Design Methodology Based on Graph Theory and Many-Objective Optimization. Journal of Water Resources Planning and Management, 146(8):04020068.

Meijer, D., Post, J., van der Hoek, J. P., Korving, H., Langeveld, J., and Clemens, F. (2021). Identifying critical elements in drinking water distribution networks using graph theory. Structure and Infrastructure Engineering, 17(3):347–360.

Mohammed A., Kaddoura K., Zayed T., Moselhi O., Hawari A. (2022). Integrated Reliability Assessment Model for Drinking Water Networks: A Case Study of the City of London, Canada, J. Perform. Constr. Facil., 36(5).

Ofwat. Towards resilience: how we will embed resilience in our work, 2015.

Porse E. & Lund J. Network Analysis and Visualizations of Water Resources Infrastructure in California: Linking Connectivity and ResilienceJ. Water Resour. Plann. Manage., 2016, 142(1)

Taiwo, R., Ben Seghier, M. E. A., & Zayed, T. (2023). Toward sustainable water infrastructure: The state-of-the-art for modeling the failure probability of water pipes. Water Resources Research 59, e2022WR033256. https://doi.org/10.1029/2022WR033256.

Wagner, J.M., Shamir, U., Marks, D.H., 1988.Water distribution reliability: simulation methods. J. Water Resour. Plan. Manag. 114 (3), 276e294.

Zali R. B.; Latifi M.; Javadi A. A.; and Raziyeh Farmani R. (2024) Semisupervised Clustering Approach for Pipe Failure Prediction with Imbalanced Data Set, J. Water Resour. Plann. Managem., 150(2).

Zhang, K., Yan, H., Zeng, H., Xin, K., and Tao, T. (2019). A practical multi-objective optimization sectorization method for water distribution network. Science of The Total Environment, 656:1401–1412.

Zhang, T., Yao, H., Chu, S., Yu, T., and Shao, Y. (2021). Optimized DMA Partition to Reduce Background Leakage Rate inWater Distribution Networks. Journal of Water Resources Planning and Management, 147(10):04021071.

Zingali L. C., Monaci M., Bragalli C. (2024). Application of Primary Network analysis in real Water Distribution Systems, WDSA/CCWI 2024.